Wake analysis of Floating Wind Turbines using multifidelity AMR-Wind-OpenFAST simulations

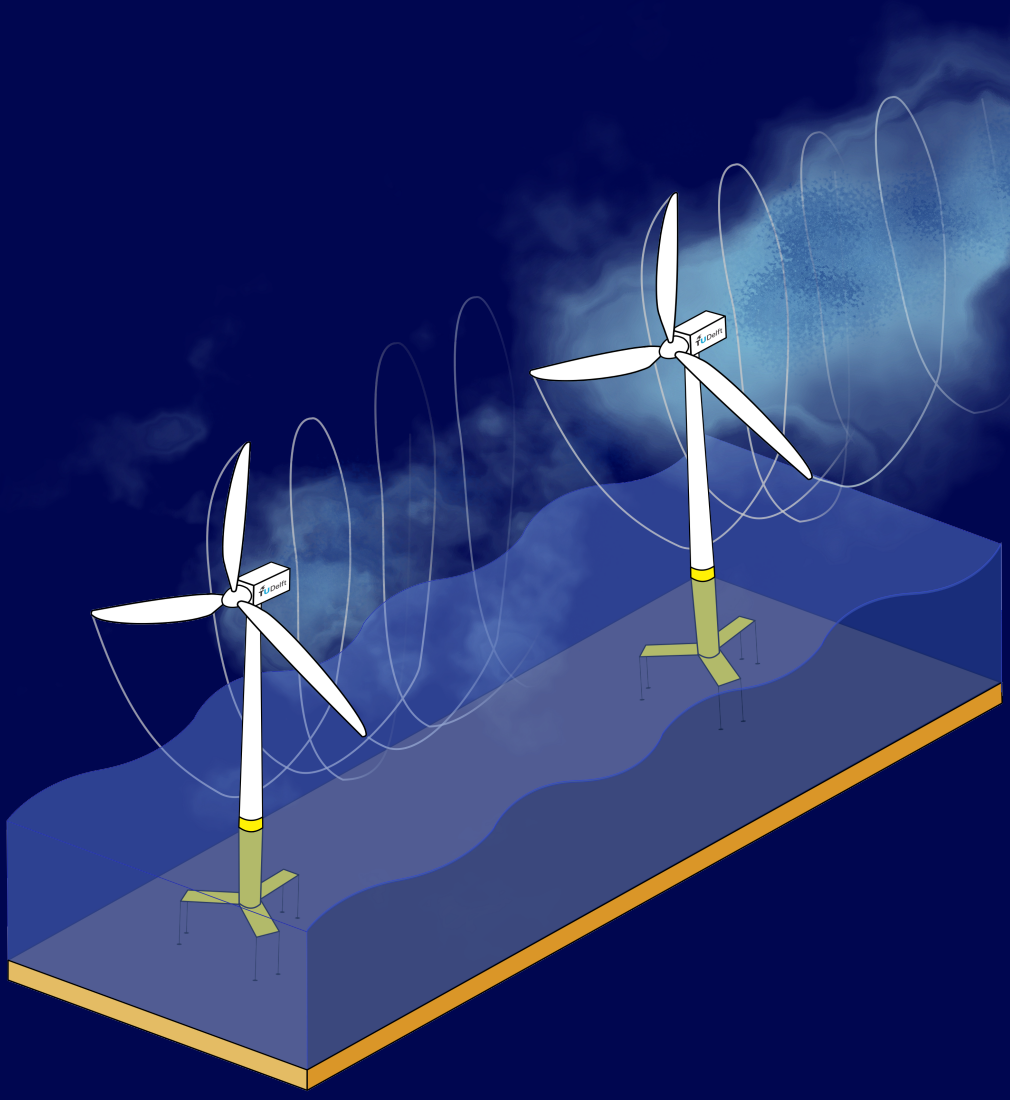

Author:
Alexandru Guntner
Rotor Design - Aerodynamics
July 2025

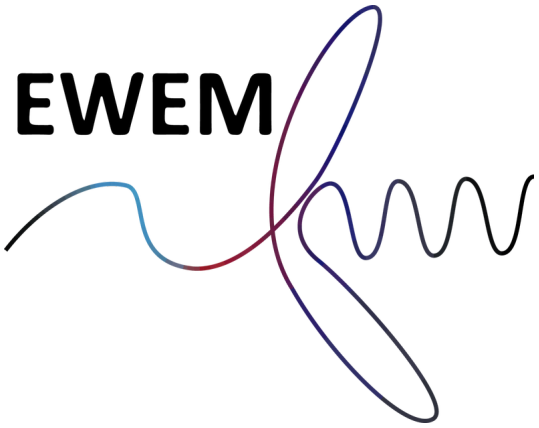

Wake analysis of Floating Wind Turbines using multifidelity AMR-Wind-OpenFAST simulations

Alexandru Guntner

to obtain the degrees of:

Master of Science
in Wind Energy
at Technical University of Denmark

Danmarks Tekniske Universitet

DTU

Master of Science
in Aerospace Engineering
at Delft University of Technology

TU Delft Delft University of Technology

Supervisors:

Hamid Sarlak	DTU
Axelle Viré	TU Delft
Delphine De Tavernier	TU Delft

An electronic version of this thesis is available at
https://repository.tudelft.nl

Preface

The past two years have flown by, yet I can still vividly remember the moment I found out I had been accepted into the European Wind Energy Master. I was filled with excitement at the prospect of beginning this new chapter of my life. What followed was a roller coaster of emotions, challenges, but also meaningful experiences that helped me grow both personally and professionally. Throughout this journey, I had the chance to delve into the technical aspects of these huge rotating machines, the *wind turbines*. At the same time, moving from my new "home" in the Netherlands to Denmark pushed me out of my comfort zone once again. It allowed me to explore a beautiful country, adapt to a different way of life, and build long-lasting friendships.

The topic of this thesis comes from my interest in floating wind turbines, which first sparked during a course on this subject taught by Axelle Viré and Delphine De Tavernier. I have always been fascinated by the colorful visualizations of moving airflow, and so I decided to explore the subject through numerical methods. The initial concepts for this work emerged through discussions with Hamid Sarlak. He put his trust in me by giving me the responsibility to contribute to the INF4INITY project, while also allowing me the freedom to pursue what I believed was the best path. I would like to thank my supervisors Axelle, Delphine and Hamid for their guidance, encouragement, and even the informal conversations we had during this time.

I am also grateful to everyone who supported me along the way, my friends and family. A special mention to my parents for always being there for me during the past five years I have lived far from home. Your love has meant everything.

Alexandru Guntner
July 2025, Copenhagen

Abstract

The growing global demand for green energy requires the development of innovative solutions. Floating offshore wind turbines (FOWTs) present significant potential by enabling the harvesting of wind in deep-sea waters. However, as this technology is still in its early stages, the impact of the added six degrees of freedom (6-DOF) motion on wake dynamics and power performance remains unclear. Understanding these effects is critical for the design of floating wind farms. In this work, large eddy simulations and an actuator line model are employed to investigate the wake behavior and power output of the IEA-15MW reference turbine mounted on several floating platform concepts. To explore wake interactions in wind farm scenarios, two tandem FOWTs are modelled. The simulations are carried out in AMR-Wind, coupled with OpenFAST for the platform and blades' motion. Initial cases are conducted with a laminar inflow to isolate fundamental wake mechanisms. Then, a neutral atmospheric boundary layer (ABL) is recreated to perform investigations with realistic offshore conditions. Platform motions are found to induce velocity fluctuations in the wake and promote vortex-pairing. High-frequency and large-amplitude motions particularly enhance wake recovery in the upstream wake, although this effect is less pronounced in the downstream wake. Among all 6-DOF, surge is identified as the main driver of wake dynamics. FOWTs generate larger turbulence levels than their fixed counterparts during laminar inflow. Notably, when the downstream turbine moves in phase with the incoming wake, the resulting interaction leads to the superimposition of the wake structures, forming large, separated low-speed regions. In contrast, under turbulent conditions, FOWTs generate lower turbulence in the near wake, but similar levels further downstream. In these cases, the differences in mean wake velocity between floating and fixed turbines decrease significantly with distance. The tandem FOWTs are found to produce less total power when operating at rated speed during neutral ABL conditions. However, the downstream FOWTs exhibit power gains of up to 20%, indicating that larger floating wind farms are likely to generate more electricity than traditional bottom-fixed offshore wind farms.

Keywords: floating offshore wind turbines, wake, large-eddy simulations, actuator line, AMR-Wind, OpenFAST

Contents

List of Figures

List of Tables

Nomenclature

Actuator Line

α	Angle of attack [deg]
ϵ	Smearing radius [m]
η_ϵ	Smearing function [-]
c	Chord [m]
f	Force [N]
f_ϵ	Smeared force [N]
F_d	Drag [N]
F_l	Lift [N]
r	Blade spanwise coordinate [-]
w	Width of blade element [m]

Large-Eddy Simulations

$\bar{s}$	Horizontally averaged velocity [m/s]
β	Thermal expansion coefficient [1/K]
Δ	Grid size [m]
δ_i	Filter width [m]
δ_{ij}	Kronecker delta [-]
ϵ_{ijk}	Levi-Civita tensor [-]
$\hat{\partial}_i$	Anisotropic derivative [-]
κ	von Karman constant [-]
μ	Kinematic viscosity [m^2/s]
ν_t	Eddy viscosity [m^2/s]
Ω	Earth's angular velocity [rad/s]
τ	Subgrid scale stress tensor [m^2/s^2]
τ_θ	Subgrid scale heat flux [Km/s]
θ	Temperature [K]
θ_0	Ambient temperature [K]
B	Bouyancy term [N]
C	Coriolis force [N]
g	Gravitational acceleration [m/s^2]
p	Pressure [Pa]
Pr	Laminar Prandlt number [-]
S_{ij}	Strain rate tensor [1/s]
u	Velocity component [m/s]
u_τ	Friction velocity [m/s]
z_0	Roughness length [m]
z_b	Distance to closer grid cell [m]

Wind Turbine

β	Wave propagation direction [deg]
Δ	Distance between wind turbines [m]
η	Wave elevation [m]
ω_n	Wave frequency [1/s]
D	Rotor diameter [m]
f_S	Surge frequency [1/s]
H_s	Significant wave height [m]
k_n	Wave number [1/m]
P_{rated}	Rated power [MW]
T_p	Peak period [s]
U	Wind velocity [m/s]
U_∞	Freestream velocity [m/s]
U_{rel}	Relative velocity [m/s]

Abbreviations

ABL	Atmospheric boundary layer
ADM	Actuator disk method
ALM	Actuator line method
AMD	Anisotropic minimum-dissipation
BEM	Blade element momentum
CFD	Computational fluid dynamics
CNBL	Conventionally neutral atmospheric boundary layer
DLC	Design load case
DOF	Degree of freedom
DNS	Direct numerical simulations
ECMWF	European Center for Medium Range Weather Forecasts
FLLC	Filtered lifting line correction
FOWT	Floating offshore wind turbine
FVW	Free vortex wake
HSB	Highj-speed bubble
IB	Immersed boundary
IDFT	Inverse discrete fourier transform
IEA	International Energy Agency
IEC	International Electrotechnical Commission
INF4INITY	INtegrated designs for Future Floating oFFshore wINd farm TechnologY
LASD	Lagrangian-averaged scale-dependent
LES	Large-eddy simulations
NREL	National Renewable Energy Laboratory
PIWS	Phase-induced wake separation

POD	Proper orthogonal decomposition
PSD	Power spectral density
RANS	Reynolds averaged Navier-Stokes
SGS	Subgrid-scale
SOWFA	Simulator for Off/Onshore Wind Farm Applications
TI	Turbulence intensity
TKE	Turbulence kinetic energy
TLP	Tension-leg platform
URANS	Unsteady Reynolds averaged Navier-Stokes
WALE	Wall-adapting local eddy-viscosity
WT	Wind turbine

1 Introduction

Floating offshore wind turbines (FOWTs) are gaining significant attention for their potential energy applications in the near future. As the race towards a carbon-neutral society continues, generating electricity from renewable sources has become more important than ever. Wind energy is one of the fastest-growing industries in the world and is leading the green transition [1]. However, the increasing spatial constraints of onshore and traditional offshore wind farms require innovative solutions to meet rising energy demands. Deep offshore presents a significantly greater energy potential compared to shallow water areas [2]. The implementation of FOWTs is necessary in regions where sea depths exceed 50-60 m, in which bottom-fixed wind turbines become no longer economically viable [3]. Far from the coast, they benefit from steadier winds, reduced noise regulations and visual impact. Furthermore, floating foundations offer environmental benefits compared to fixed-bottom designs due to the less intrusive construction techniques employed on the seabed [4].

Altough FOWTs have been a focus of research since the mid 90's, when the commercial wind industry was becoming well established [5], it was not until 2009 when the first large scale grid connected floating turbine was installed. This involved a 2.3 MW turbine deployed by Equinor in Norway [6]. In the last decade, the advancement of floating concepts has accelerated, with numerous prototypes being developed globally. A significant milestone occurred in 2017 with the commissioning of Hywind Scotland, the world's first commercial floating offshore wind farm, which features five turbines with a capacity of 6 MW [7].

Currently, the limiting factor for the adoption of FOWTs is the cost associated with floating platforms, which can be as expensive as the wind turbines [8]. According to the International Renewable Energy Agency (IRENA) [9], the projected economies of scale will make floating offshore wind competitive and commercially viable by 2035.

Because large-scale deployment has yet to occur, there is still limited understanding of the dynamics and complex wake interactions between FOWTs, particularly within wind farm configurations. This holds particularly true for the upcoming generation of wind turbines exceeding 15 MW, which are expected to lead floating projects in the future. Addressing these knowledge gaps is essential for optimizing wind farm layouts, enhancing energy production, and reducing the levelized cost of energy. One critical challenge is understanding how the additional degrees of freedom associated with FOWTs motion affect wake recovery and the dissipation of turbulent kinetic energy [10]. The flow field generated by the moving platform leads to unsteady aerodynamics and the breakdown of the momentum balance equations [11]. These phenomena lead to increased structural loads and fluctuating power output [12, 13], which are key concerns given the high operational and maintenance costs of FOWTs [14].

This research aims to investigate the wake characteristics of two FOWTs in tandem by means of multi-fidelity numerical simulations. A comprehensive comparison of different floater designs and their performance is also made. The remainder of the work is structured as follows: a review of the theory behind wind turbine wakes and the current state of research on FOWTs is presented in Section 1.1. This is followed by an outline of the objectives and research questions. Chapter 2 introduces the methodology and relevant theoretical framework. The simulation setup and its validation are described in Chapter 3. The results are then presented and discussed in Chapter 4 and Chapter 5. Lastly, the conclusions and outlook of the work are provided in Chapter 6.

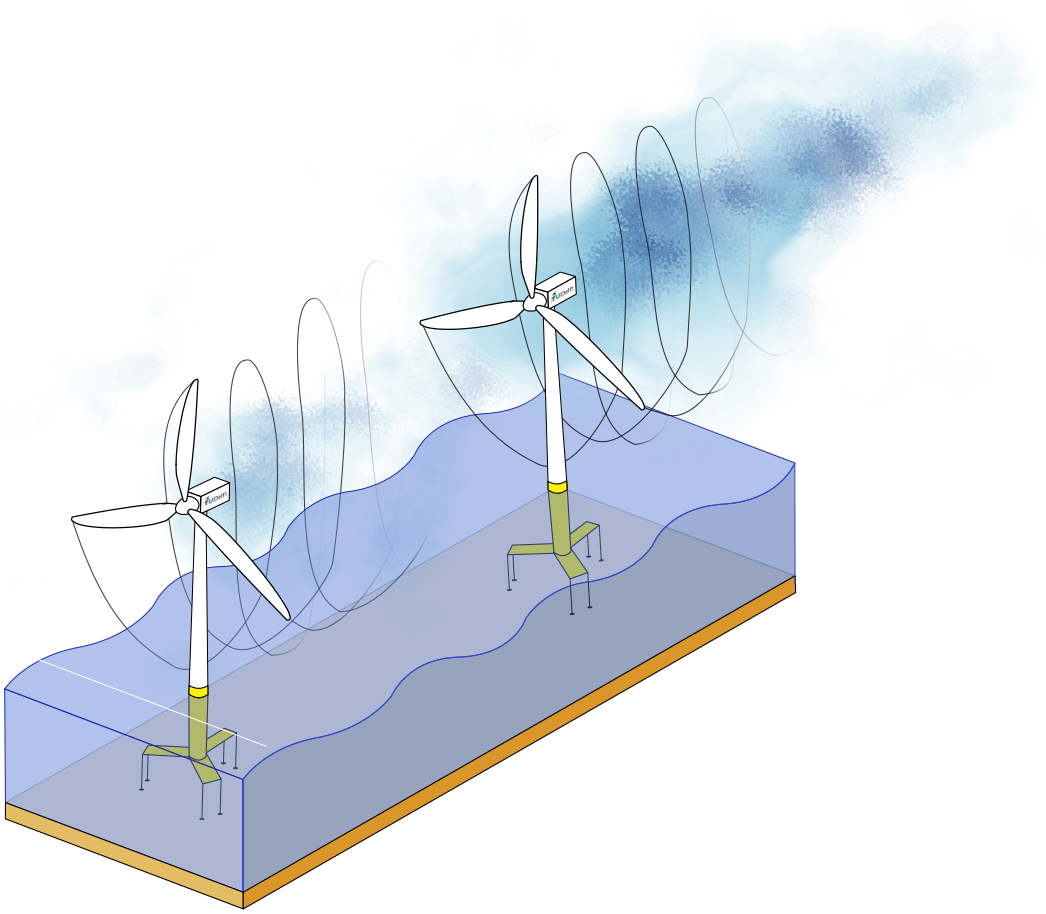

Figure 1: Illustration of the wakes of two floating wind turbines in tandem.

1.1 Literature Review

This section outlines the key characteristics of wind turbine wakes and examines the impact of floating wind turbine motion on wake evolution. Additionally, it provides a review of the numerical techniques commonly used to investigate these phenomena. Fundamental aspects of wind energy are not rigorously discussed here but can be found in the books of Hansen [15] and Burton et al. [16].

1.1.1 Wind Turbine Wakes

Wind turbines extract energy from the wind through their blades, which sweep out a rotor disk that develops a pressure difference across its surface. This leads to a loss of axial momentum in the wind and a reduction in the flow velocity behind the turbine. This downstream region is known as the *wake*. To maintain conservation of momentum, the imaginary streamtube of air passing through the turbine expands its cross-sectional area as it travels downstream. By rotating, the blades exert a torque on the incoming air, inducing a reaction that causes the wake to rotate in the opposite direction. The magnitude of this rotation reduces as the downstream distance increases. Shear layers are formed at the edge of the rotor disc and gradually merge until the central region of the wake regains properties similar to the freestream.

The region upstream of a turbine is referred to as the induction region, while the downstream wake can be further divided into the near-wake and far-wake (see Figure 2). The near-wake is directly influenced by the presence of the turbine blades and the associated aerodynamic phenomena. As a result, it is characterized by a complex vortex system and three-dimensional, unsteady and heterogeneous flow patterns [17]. In contrast, the far-wake is influenced more by global wind turbine parameters, such as thrust and power coefficients, as well as incoming flow conditions, which allow for reasonably accurate predictions of mean flow distributions in this region [18]. Generally, near-wake research focuses on turbine performance and the physical processes of power extraction, whereas far-wake studies emphasize wake interactions, turbulence models, and topographical effects, particularly in the context of wind farms [19].

Many of the theories and engineering models developed to study wind turbine wakes rely on simplifications and assumptions. This is because some fundamental aerodynamic mechanisms of wind turbines are not fully understood yet. Indeed, wind systems operate under complex conditions, including atmospheric turbulence, wind shear caused by ground effects, temporal and spatial variations in wind direction, and interactions with the wakes of nearby turbines. These factors collectively define the typical operating environment for turbine blades. Consequently, the aerodynamic forces acting on the blades fluctuate in both time and space, making a dynamic description an important aspect of aerodynamic analysis [20].

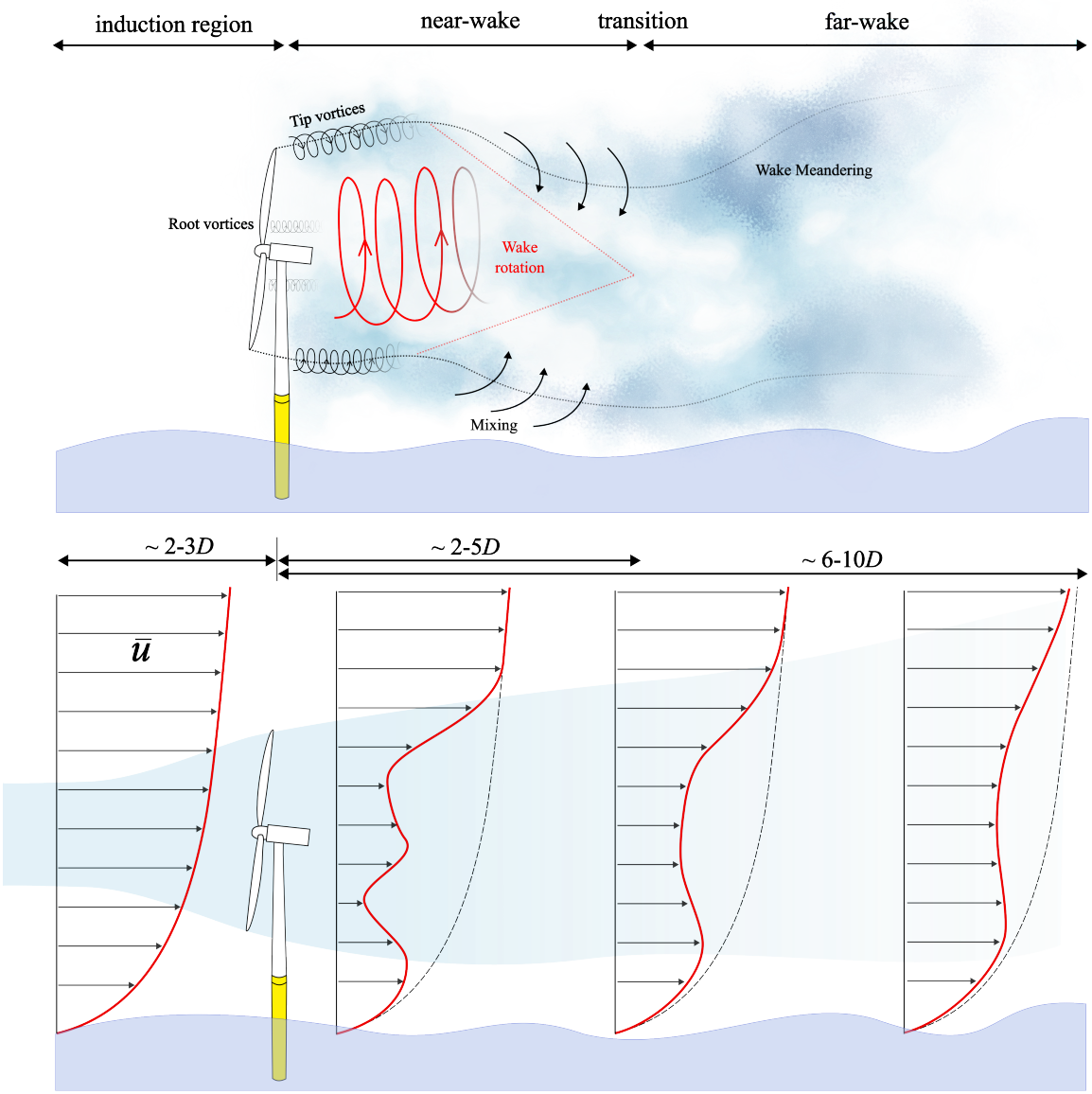

Figure 2: Flow regions and mean wind velocity profile of a floating offshore wind turbine, including interaction with the incoming boundary layer.

The length of the airflow regions presented in Figure 2, described in rotor diameters (D), is influenced by several factors. These include the number of blades and tip-speed ratio of the wind turbine [21], the boundary layer and turbulence intensity of the incoming flow [22, 23, 24], buoyancy forces due to atmospheric instability [25], and tower and nacelle effects [26]. As can be seen, the far-wake region is characterized by a self-similar Gaussian velocity-deficit distribution [27].

1.1.2 Vorticity Generation

Wind turbines shed a large amount of vorticity in the downstream flow. This is mostly visible in the near-wake, where aerodynamic forces and viscous effects act on the flow. Vorticity is defined as the curl of the velocity field and can be generated by a non-conservative force field, such that $\nabla \times f \neq 0$. In the ideal rotor disc model, assuming incompressible and inviscid flow, vorticity is concentrated near the blades' tips and roots due to the large force gradients in these regions. As the blades rotate, the tip vortices are convected downstream with the flow and form a helical path that rotates in the turbine's opposite direction of rotation [28]. In reality, however, vorticity is shed along the entire blade span due to the spanwise variation of bound circulation and the viscous effects. Despite its limitations, this model still provides valuable insight into the primary regions of vorticity concentration [29].

The evolution of the root vortex structure is less significant than the tip vortex structure, as it dissipates earlier due to interactions with the induction effects from the hub. The root vortices are also located much closer to each other, leading to a faster destruction of their spiral structures. In contrast, the tip vortices are more stable and persist for longer, determining the overall behavior of the wake [30].

The tip vortices are caused by the pressure difference between the top and lower sides of the blade tip, which drives the flow from the pressure side to the suction side of the blade. Initially, the tip vortex diameter decreases due to vortex stretching caused by wake expansion. Over time, the diameter increases as a result of viscous effects [31]. In the near wake, tip vortices can limit flow entrainment by isolating this region from the surrounding outer flow [32]. Eventually, these structures break down into smaller-scale turbulence through mutual inductance instability mechanisms, such as vortex pairing of the tip vortices. This effect is also known as "leapfrogging" and leads to the merging and destabilization of the tip vortices [32, 33, 34], as shown in Figure 3. The breakdown process is accelerated at higher tip-speed ratios [21].

1.1.3 Turbulence Generation

The downstream vicinity of the turbine is characterized by increased turbulence, a critical aspect that can lead to dangerous unsteady loads on downwind turbines and increase fatigue damage [35]. Turbulence intensity (TI) typically decays just behind the turbine nacelle but increases as the shear layers at the tip expand until they meet at the center, where TI decreases again. In standard operations, the turbulence vertical profile is asymmetric and exhibits higher intensity at the top tip. This is attributed to the significant mechanical generation of turbulence kinetic energy (TKE) in this region, associated with the strong shear and momentum flux, as observed by Wu et al. [23]. High turbulence levels in the incoming flow favour turbulent mixing and entrainment, facilitating faster wake recovery.

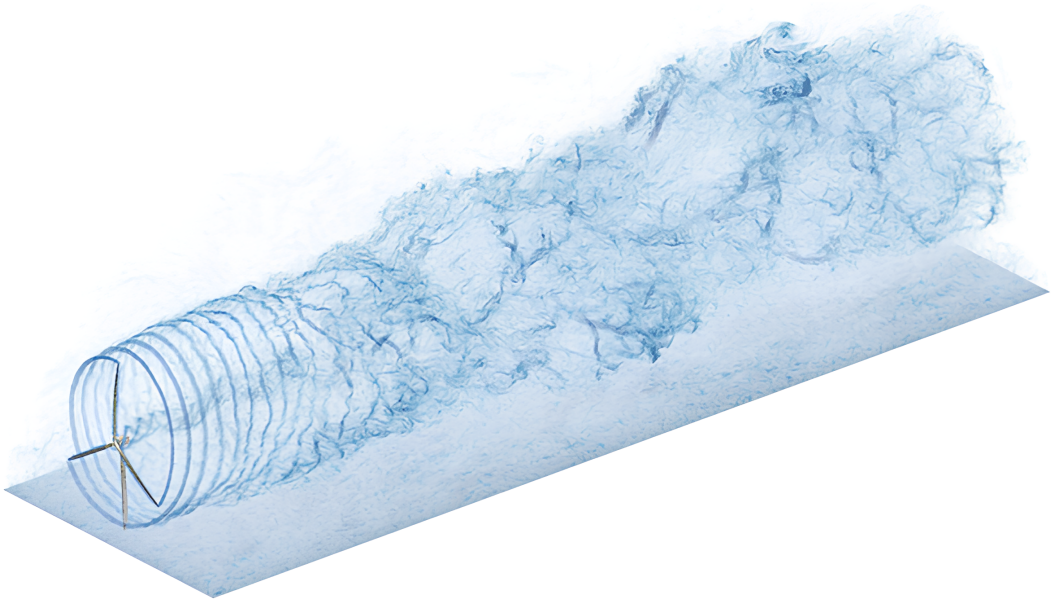

Figure 3: Wake structures of a large offshore wind turbine. Reproduced from Trigaux et al. [36].

1.1.4 Interactions with Atmospheric Boundary Layer

The atmospheric boundary layer (ABL) can be described as "the part of the troposphere that is directly influenced by the presence of the earth's surface, and responds to surface forcings with a timescale of about an hour or less", according to Stull [37]. The thickness of this layer can vary significantly, spanning from several hundred meters to a few kilometers. The ABL is characterized by complex, three-dimensional turbulent flows, driven by wind shear and surface friction, as well as variations in the terrain such as buildings and vegetation. Solar radiation also plays a significant role by creating thermal gradients that drive air motion, which can either promote or hinder vertical air movement through buoyancy effects. Additional influencing factors include large-scale pressure differences and the Coriolis effect. A typical ABL flow covers a broad spectrum of turbulent scales, extending from the integral scale down to the Kolmogorov scale. The development of the ABL generally follows a daily cycle, influenced by changes in radiative energy between day and night.

The traditional classification of atmospheric stability is based on surface thermal effects. Three distinct types of atmospheric boundary layers can then be identified: the neutral boundary layer (NBL), the stable boundary layer (SBL), and the unstable or convective boundary layer (CBL). In unstable conditions, when the ground is warmer than the air above, buoyancy promotes the formation of turbulent eddies. As these eddies expand, they generate a well-mixed layer that is typically bounded above by a temperature

inversion. In contrast, under stable conditions, such as when warm air moves over a cooler surface, buoyancy acts to suppress turbulence. In an NBL, there is no heat exchange between the surface and the atmosphere, and the potential temperature remains uniform with height. As a result, vertical air movements are neither amplified nor reduced.

Neutral boundary layers have been further distinguished between truly neutral flows, which form in neutrally stratified environments, and conventionally neutral layers (CNBL), which arise in the presence of stable stratification [38]. The latter is more commonly observed over seas, where surface heat fluxes are typically lower [39].

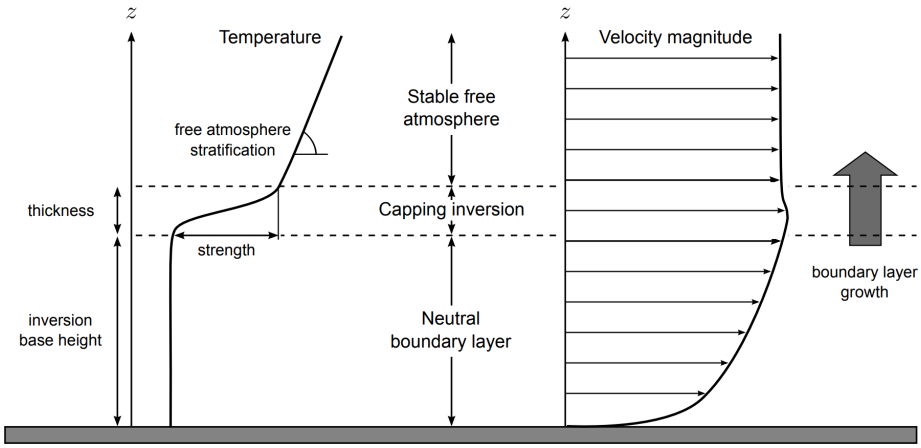

Figure 4: Schematic view of the conventionally neutral atmospheric boundary layer. Reproduced from Allaerts & Meyers [40].

Wind shear in the ABL plays an important role in defining the structure of a wake. The interaction with the turbine wind speed profile creates a highly inhomogeneous wake characterized by asymmetries, streamwise vorticity, and non-periodic behavior downstream of the turbine rotor. The blades get exposed to surface pressure variations, which, in turn, cause large fluctuations in the power output and thrust forces generated by the turbine [24]. Moreover, atmospheric stability - and the associated turbulence characteristics - can substantially impact the length of turbine wakes within wind farms. Wake recovery is most effective in unstable atmospheric conditions, whereas stable conditions lead to extended wakes characterized by significant velocity deficits [18, 41].

The influence of the size of a wind turbine rotor on the interaction with the incoming sheared inflow has received little attention. Larger rotors will experience more dynamic inflow due to the increased wind speed difference across their vertical span. Still, their elevated height reduces interaction with the steep velocity gradients near the surface, resulting in lower turbulence generation [42]. As a result, the wake is anticipated to persist longer due to lower mixing in the wake.

1.1.5 Floating Motion

Floating wind turbines are subject to translational and rotational platform motions due to wind and wave loading. The added six degrees of freedom (6-DOF), illustrated in Figure 5, can cause increased structural loads and power fluctuations compared to land-based systems [43]. Generally, platform motions are reported to increase the mean power production [12, 44].

Floaters can be categorized based on how they achieve static stability in pitch and roll. Some of the main designs are tension leg platforms (TLPs), spar buoys, semi-submersibles and barges. Stability is maintained through different mechanisms: TLPs rely on a taut mooring system combined with excess buoyancy, spar buoys utilize a deep draft with ballast, and barges achieve stability with a shallow draft and a large waterplane area. Semisubs are hybrid designs that incorporate features from all three types [45].

Each type of floating platform has its advantages, and the selection of the most suitable design depends on the analysis of geographical and environmental conditions. In general, a balance between total costs and stability of the platforms is required. While no single design has emerged as the dominant choice, the semisub platform has been the most popular and widely adopted [46].

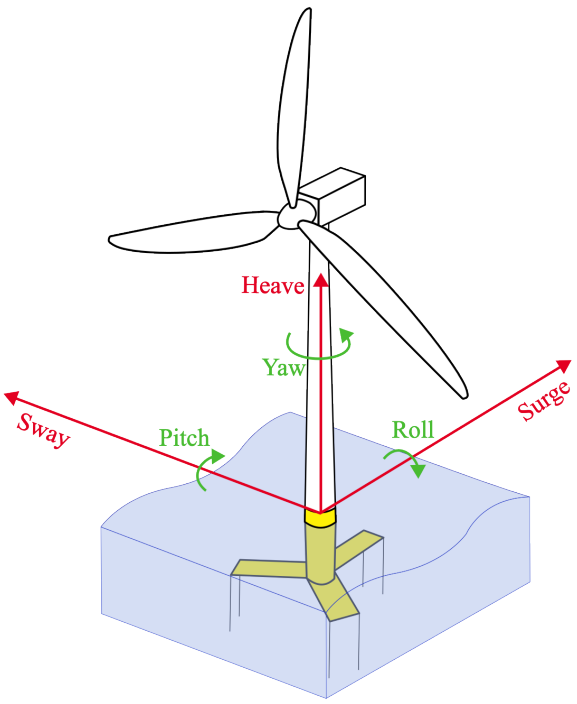

Figure 5: The six degrees of freedom of a floating wind turbine.

Platform motion significantly influences the performance of a wind turbine. Surge and pitch typically show the largest amplitudes in a FOWT and can potentially amplify or counteract each other. Figure 23 compares the average displacement of three platform concepts for different wind and wave loads reported in Table 1. The overall mean for each platform is also displayed. The data is derived from both numerical and experimental studies. Note that investigations with similar wind and wave conditions are limited. All the authors used the JONSWAP spectrum for wave generation, with H_s describing the significant wave height, $\overline{U}$ the mean wind velocity, and T_p the wave peak period.

Table 1: Methods and environmental conditions in selected floating wind studies.

Author(s)	$\boldsymbol{P_{rated}}$ [MW]	$\overline{\boldsymbol{U}}$ [m/s]	$\boldsymbol{H_s}$ [m]	$\boldsymbol{T_p}$ [s]	**Method**
Sebastian et al. [11]	5	11.4	2.54	13.35	OpenFAST
Johlas et al. [47]	5	8	8	14	SOWFA
Goupee et al. [48]	5	17	10.5	14.3	Experimental
Maktabi et al. [49]	10	11.4	4	12	SIMA

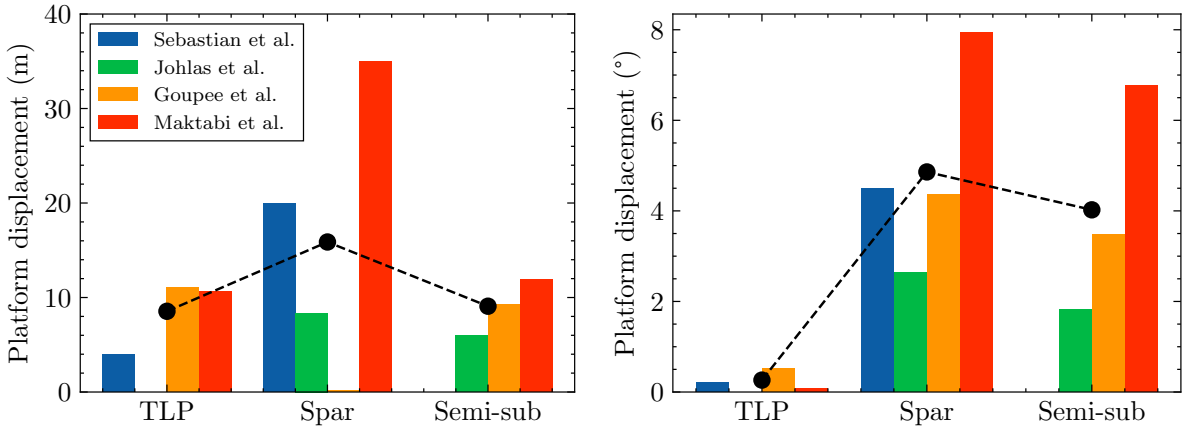

(a) Surge motion

(b) Pitch motion

Figure 6: Mean displacements of three floating concepts reported from different studies.

TLPs demonstrate the best performance in terms of stability and motion. They experience a moderate surge motion and their pitching is almost negligible. In contrast, spar buoys exhibit significant motion in both surge and pitch, whereas semisubs show moderate responses.

Notably, surge data of the spar from the study by Goupee et al. [48] indicates almost no motion, which contradicts findings from other studies. Tomasicchio et al. [50] conducted experiments using a scaled 5MW spar buoy turbine, revealing moderate surge motion,

results that were also confirmed with OpenFAST. Similarly, Huang et al. [44] employed an unsteady actuator line method (ALM) on a 5MW turbine and observed comparable surge motion. They also highlighted how aerodynamic forces from the wind turbine greatly influence the motion responses of the platform, particularly in surge, pitch, and yaw. These findings emphasize that differences in experimental setups and platform designs can significantly affect floater responses.

Overall, altough TLP-type turbines are very stable, thanks to the highly tensioned mooring system, their primary challenge remains to achieve cost-effective installations. Only a few FOWTs with this concept have been installed worldwide [46], making TLPs far less common than other designs. In contrast, spar platforms are simpler and less expensive to construct. For a more comprehensive review of floating platforms, refer to the work of Leimeister et al. [51].

1.1.6 Influence of Motion on the Wake

The additional degrees of freedom in a FOWT contribute to a more complex aerodynamic environment around the rotor. A key change is the introduction of new wind components, which lead to variations in the angle of attack (see Figure 7). FOWTs are particularly affected by both periodic and aperiodic sources of unsteadiness, and experience effects such as unsteady airfoil dynamics and dynamic inflow [52]. Time variant wind speed is likely to cause hysteris loops in the aerodynamic forces. Moreover, compared to bottom fixed turbines, FOWTs might experience pronounced skewness in the flow due to yaw and pitch motions, as well as stronger wind shear across the rotor disk [11].

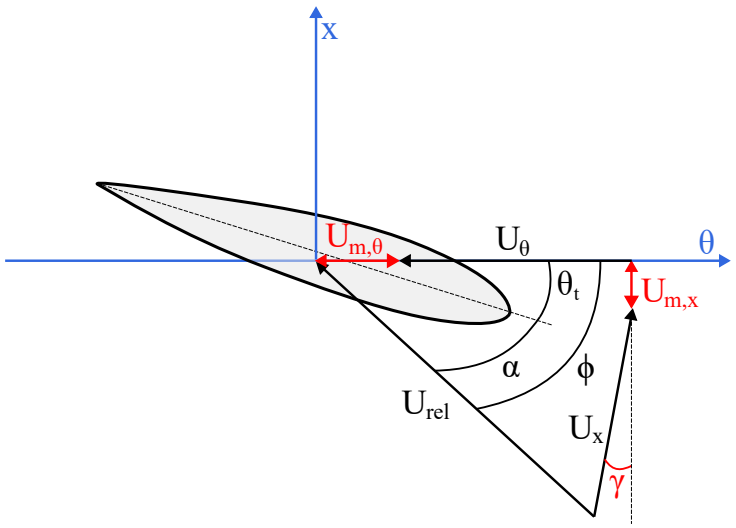

Figure 7: Velocity triangle of floating wind turbine airfoil. In red, the additional velocity components and angles change due to translational and rotational motion respectively.

As previously mentioned, pitch and surge have the greatest impact on the aerodynamic properties of the flow that can lead to highly unsteady conditions. These motions enhance the interaction between the wind turbine and its wake. Figure 8 shows a schematic of the four operating states of a FOWT [11]. During a still or forward motion, the wind turbine operates in the windmill state. However, as the turbine moves downward, it interacts with its wake, creating unsteady conditions and leading to the formation of recirculation areas. With increasing motion speed, these recirculation zones develop into a vortex ring state. When the relative speed approaches zero or becomes negative, the system transitions to the propeller state, where the turbine outputs energy to the flow field. The turbulent and vortex ring states are particularly significant due to their potential to cause structural damage.

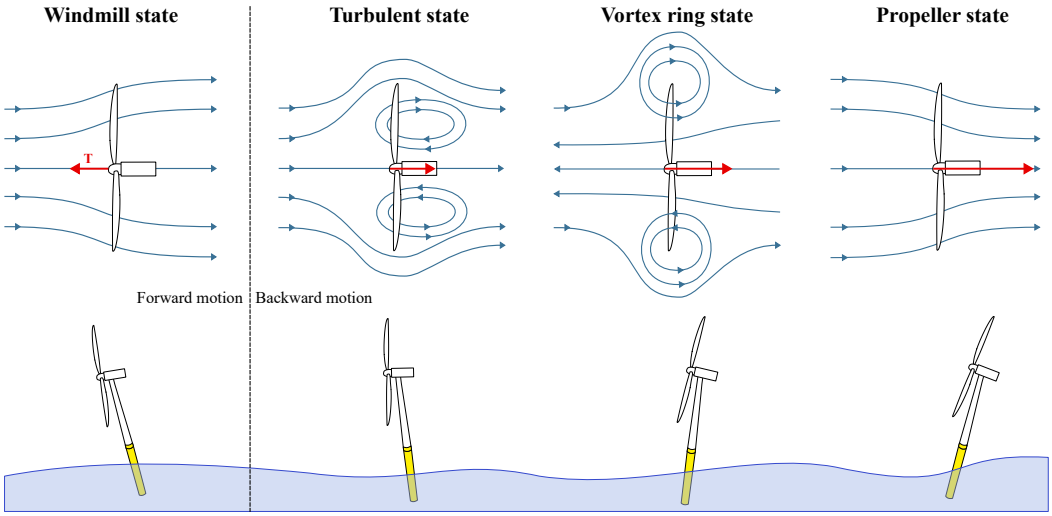

Figure 8: Operating modes of a floating wind turbine undergoing pitch and surge motions.

The rapidly changing circulation along the blade due to platform motions generates additional vortices along the trailing edge. These vortices might not only influence the blade that sheds them but also affect the subsequent blade passing through the same azimuth angle. The strength of the shed vortices is determined by the rate of change in the angle of attack, which is directly linked to the rate of change in motion velocity. Surge and pitch can cause a returning wake effect that has a significant impact on aerodynamic loads. While this phenomenon is well-studied in helicopter aerodynamics, it has received limited attention in the context of FOWTs [53].

It is widely accepted that turbine motions promote wake recovery and accelerate the dissipation of turbulent kinetic energy [10, 13]. Wake structures subjected to platform motion exhibit greater distortion, with helical structures breaking down and transitioning

to a turbulent wake earlier than those in bottom-fixed turbines [54]. Fu et al. explored the characteristics of wakes both through experimental [55] and computational studies [56], determining that indeed, wake structures mix at an earlier stage, especially under large amplitude motion. The resulting increase in turbulence leads to stronger instabilities on downstream turbines. Li [57] investigated the impact of surge amplitude and frequency and found that faster and larger oscillations improve wake recovery. His results indicated that differences from the fixed cases are also dependent on the ambient turbulence intensity.

In addition, platform movements are likely to promote the development of robust circular wake structures, with their period, intensity, and center being influenced by the motion and operational conditions of the FOWT [58]. This causes fluctuations in the aerodynamic performance of the turbine. Side-to-side motions at specific frequencies can trigger large-scale far-wake meandering, enhancing wake mixing. This, in turn, induces strong unsteady loads on downstream turbines and amplifies yaw motions in downstream FOWTs compared to upstream turbines [59].

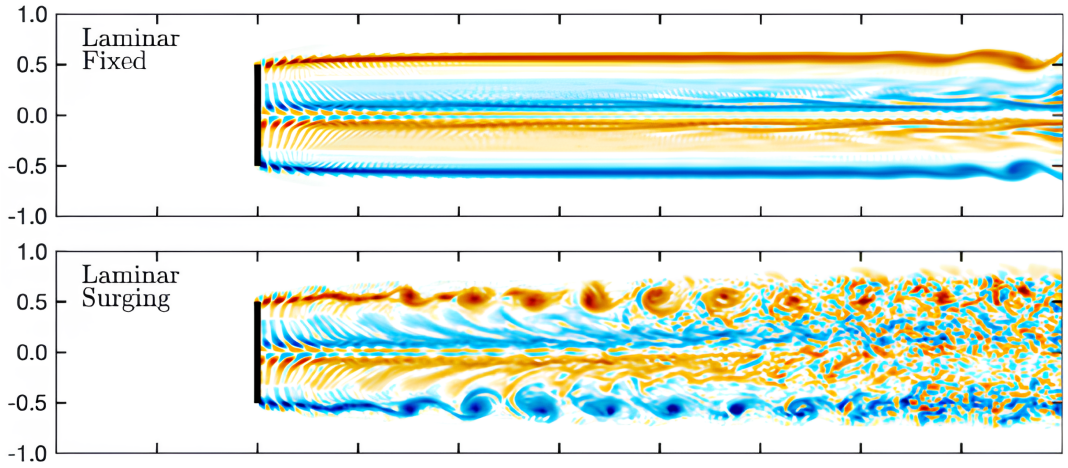

Figure 9: Influence of harmonic surge motion on the vorticity of a wind turbine wake [57].

Some experimental studies present different outcomes concerning the wake evolution of FOWTs. Rockel et al. [60, 61] found that the pitching motion of a FOWT resulted in slower wake recovery compared to bottom-fixed turbines. However, they noted that FOWTs might benefit from reduced fatigue loads due to their ability to dampen fluctuations. Fontanella et al. [62] observed that the average axial velocity and TKE in the wake were slightly lower with motion, leading to a more stable wake. Lastly, Belvasi et al. [63] found no observable effect of prescribed heave, surge, and pitch motions on far-wake recovery.

Johlas et al. [47, 64] concluded that under realistic inflow conditions, changes in wake structure between floating and fixed wind turbines are generally small. These become

more pronounced under stable ABL conditions and are primarily attributed to mean platform displacements, such as sustained positive pitch. In contrast, variations in turbulence intensity are linked to time-varying platform motions. The authors further stressed that the differences remain minimal particularly under conditions of high wind speeds and low wave heights.

1.1.7 Wake Interactions between Floating Wind Turbines

Wake interactions between wind turbines are of particular importance in the design of wind farms. Understanding this phenomenon is critical for optimizing layouts and operational strategies, reducing power deficits and mitigating fatigue loads. While the wake and blockage effects in large bottom-fixed offshore wind farms have been extensively studied (e.g. Troldborg et al. [65], Kirby et al. [66]), research on wake interactions among multiple FOWTs remains limited. Table 2 provides a summary of the available literature on wake interactions involving multiple FOWTs.

The most common numerical code for this purpose is FAST.FARM, a mid-fidelity multi-physics tool developed by NREL as an extension of OpenFAST. FAST.FARM is primarily used to predict structural loads and performance within wind farms. High-fidelity approaches are required for deeper insights. These include the actuator line (ALM) or actuator disk (ADM) methods combined with computational fluid dynamics (CFD) simulations. However, not many studies have employed the latter to investigate wake interactions within floating wind farms. Their use is limited by the substantial computational resources that are required.

Table 2: Numerical methods of selected studies focusing on multiple floating wind turbines.

Author(s)	**Year**	**Motion(s)**	**Platform(s)**	**Method**
Wang et al. [67]	2024	6-DOF	Semi	FAST.FARM
Carmo et al. [68]	2024	6-DOF	Semi	FAST.FARM
Cui et al. [69]	2024	Translational	Semi, Spar, TLP	FAST.FARM
Xue et al. [70]	2022	6-DOF	Semi	FAST.FARM
Yao et al. [71]	2023	Prescr. Surge, Heave, Pitch	-	FAST+URANS
Arabgolarcheh et al. [72]	2023	Prescr. Surge, Pitch	-	ALM+URANS
Zhang et al. [73]	2022	6-DOF	Semi	URANS
Rezaeiha et al. [74]	2021	Prescr. Surge	-	ADM+URANS
Huang et al. [75]	2018	6-DOF	Spar	UALM+URANS
Hendriks [76]	2024	Prescr. Surge, Pitch, Yaw	-	PTV
Li [57]	2023	Prescr. Surge	-	ALM+LES

Arabgolarcheh et al. [72] investigated the wake dynamics of two floating wind turbines subjected to prescribed surge and pitch motions. Their study highlighted that periodic motions increase wake complexity and found that the mean power and thrust coefficients of the downstream turbine improved by up to 5%. Rezaeiha et al. [74] reported that the downstream turbine's power coefficient increased by 1 to 4% depending on the motion amplitude. While the time-averaged velocity deficit in the wake of a surging rotor was comparable to that of a fixed rotor, the wake exhibited significantly greater unsteadiness. Huang et al. [75] further noted that platform motions increase wake vortex instability, leading to faster diffusion of the downstream rotor's tip vortices. All of these studies employed the NREL 5 MW turbine using unsteady Reynolds-Averaged Navier Stokes (URANS) simulations. However, URANS are not able to capture complex flow structures. The use of simplified boundary conditions (such as laminar, uniform inflow) is another critical limitation, as realistic turbulent inflow significantly influences wake dynamics.

To the author's knowledge, Hendriks [76] conducted the first experimental investigation of FOWTs in tandem using 3D particle tracking velocimetry. She suggested that pitch has a greater influence on the wake than surge and that low frequency movements could be seen in the loads measurements of the downstream turbine.

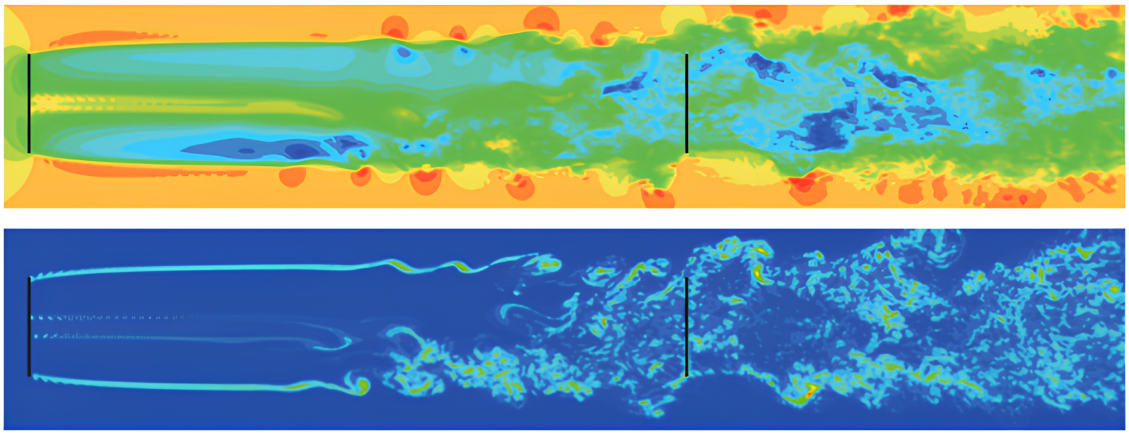

Figure 10: Instantaneous wind velocity (top) and vorticity (bottom) of bottom fixed wind turbines in tandem using actuator line technique [65].

Li [57] conducted large-eddy simulations (LES) with ALM to study two FOWTs in tandem, subjected to prescribed surge motion. His investigation showed that surge marginally enhances wake recovery in both the near and far wake under most ambient turbulence levels. He concluded that the faster wake recovery observed in surging cases is not driven by instability-induced turbulence, but rather by enhanced advection resulting from surge-induced periodic coherent structures. Finally, the system's power output increased by up to 2% at realistic turbulence intensities compared to the fixed configuration.

Based on these preliminary findings, the wake structures behind multiple floating rotors under realistic inflow conditions might not differ significantly compared to bottom-fixed rotors. While further validation is required, this implies that platform motions may have a greater impact on the wind turbine's performance than wake modifications caused by an upstream FOWT. Consequently, when modeling floating wind farm, it could be reasonable to approximate the wake of a FOWT using bottom-fixed wake models that do not account for the specific effects of an upstream floating turbine [12].

1.1.8 Numerical Framework

Floating wind turbines are being studied through on-site measurements, scaled experiments, and numerical simulations. The latter are typically validated with experimental work due to the limited amount of data available from existing sites. One of the advantages of scaled experiments is that it is possible to capture nonlinear hydro-aero interactions and allow for controlled environmental conditions. Nonetheless, they require advanced facilities capable of generating combined wind-wave conditions and suffer scaling challenges posed by Reynolds and Froude numbers. Numerical methods are cheaper and more convenient, but depending on the fidelity level, often rely on simplifications which fail to fully address coupling effects [77].

The dynamic behavior of FOWTs can be analyzed using uncoupled, partially coupled, or fully coupled approaches [78]. Uncoupled methods separate wind and wave for simplicity and independently study the hydrodynamic and aerodynamic responses. Partially coupled techniques incorporate both aerodynamic and hydrodynamic effects, but might prescribe one to focus on the other. Fully coupled methods provide the most realistic assessment by simultaneously modeling wind-wave interactions.

Simulating the aerodynamics of FOWTs with numerical techniques is challenging, particularly capturing dynamic inflow effects and wake interactions. The most widely used tools for studying horizontal-axis wind turbines are based on blade element momentum (BEM) theory and can become unreliable under large unsteady rotor motion. To address some of the limitations, empirical corrections are often added to account for non uniform, unsteady and skewed inflow conditions. Some authors have recently developed dynamic inflow models for BEM, which can adequately simulate the aerodynamics of FOWTs under most conditions (e.g. Papi et al. [79], Ferreira et al. [80]). A particular limitation of BEM, even with unsteady corrections, is its inability to account for returning wake effects, which are particularly pronounced during surge and pitch motions [53]. Free Vortex Wake (FVW) methods are able to model complex physics [81] and can be an effective compromise between computational efficiency and accuracy.

Fully coupled methods via CFD are necessary for capturing the full aero-hydrodynamic interactions of FOWTs. Wall resolved CFD simulations are very computationally expensive and are normally conducted using URANS simulation. Higher fidelity, such as

LES, is impractical for this purpose and is employed to model the wind turbine wake in single-phase simulations. Hybrid RANS-LES approaches can also be adopted, where the RANS equations model the boundary layer close to the surface, and LES is applied to the unsteady separated regions that are distant from the surface [82]. To save computational resources, one approach is to then represent the rotor through an actuator disk or actuator lines. The difference between the two in the far wake is small, making ADM a suitable trade-off for studying large wind farms. On the other hand, for near-wake studies, ADM is significantly worse than ALM as it does not generate tip and root vortices, which are essential for accurately capturing near-wake dynamics [83].

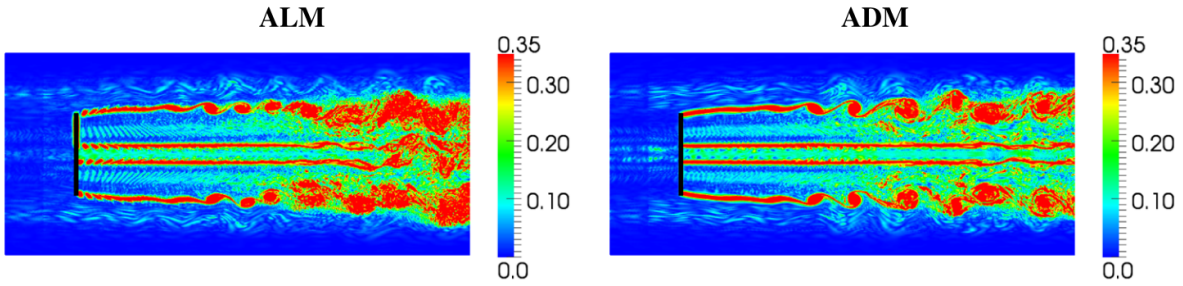

Figure 11: Vorticity around wind turbine predicted by actuator line and actuator disk large-eddy simulations [83].

Multiphase simulations require substantial computing power as they need to model the free surface between air and water. These simulations can face a phenomenon known as added mass instability, which can compromise their accuracy and cause abrupt crashes. This issue typically arises when a light, floating body interacts with a dense fluid. In scenarios where the body is rigid and the fluid is treated as incompressible, any acceleration of the body necessitates an instantaneous acceleration of the surrounding fluid. The kinematics of the problem enforce an extremely tight coupling between the two. However, any numerical delay in handling this simultaneous motion can result in the unphysical introduction of momentum into the system [84].

For a long time, most ALM implementations were developed using in-house codes, with very few commercial software options available prior to 2013 [85]. Then, the National Renewable Energy Laboratory (NREL) developed a CFD tool called the Simulator for Off/Onshore Wind Farm Applications (SOWFA) [86]. This tool integrates OpenFOAM with OpenFAST and includes both the ALM and an ABL model. SOWFA enables two-step analyses, utilizing precursor and successor simulations to replicate in silico wind turbine operations under turbulent wind conditions [87]. Johlas et al. [12, 47, 64, 88] have extensively used this tool to investigate single bottom-fixed and floating wind turbines. Body force methods that can model the turbine's tower in SOWFA have been proposed by Liu et al. [89] and Matiz-Chicacausa et al. [90]

Although some authors continue to use SOWFA, its primary limitation is its dependence on outdated versions of OpenFOAM (v6) and OpenFAST (v2.4), which lack many of the latest features and improvements. NREL has discontinued SOWFA development and is now focusing on AMR-Wind [91, 92], a new tool that integrates a CFD flow solver with OpenFAST. This integration allows wind turbines to be modeled using ADM/ALM, incorporating aero-serv-oelastic and tower effects, and floating motions in real time. A key objective of AMR-Wind is to enable efficient simulations on GPUs [91]. Two-phase flow capabilities are currently being developed with the integration of Nalu-Wind [93], which can be used to simulate wall-resolved flows.

Table 3: High fidelity CFD tools suited for floating wind turbine analysis.

Tool	**Year**	**Base software**	**Focus**
Y2-BH [94]	2023	YALES2+BHawC	Aerodynamics
AMR-Wind [92]	2020	ExaWind+OpenFAST	Aerodynamics
turbinesFoam [95]	2015	OpenFOAM	Aerodynamics
SOWFA [86]	2013	OpenFOAM+OpenFAST	Aerodynamics
naoe-FOAM-SJTU [96]	2019	OpenFOAM	Aero-Hydrodynamics
OF^2 [97]	2023	OpenFOAM+OpenFAST	Hydrodynamics
FloatingturbinesFoam [98]	2022	OpenFOAM	Hydrodynamics

Other tools include turbinesFoam, introduced by Bachant et al. [95], which employs ALM to simulate the aerodynamics of both horizontal and vertical axis wind turbines within OpenFOAM. The library's interpolation, Gaussian projection, and vector rotation functions are adapted from NREL's SOWFA. A modified version, FloatingturbinesFoam, developed by Frontera [98], extends these capabilities by handling arbitrary motions across all DOF.

Moreover, coupling between OpenFAST and OpenFOAM was developed in OF^2 [97]. This approach enables the inclusion of aero-servo-elastic couplings present in the wind turbine, alongside the hydrodynamic system resolved by CFD. It is based on the preCICE environment, which provides a massive parallel coupling library that enables standard OpenFOAM solvers to interface with external solvers without the need for code modifications [99].

Lastly, Wang et al. developed naoe-FOAM-SJTU, which includes features for fluid-structure interaction and an unsteady actuator line model [96]. Initially based on the $k-\omega$ SST turbulence model, it was recently extended to include LES [100].

1.2 Scope and Research Questions

The aerodynamic environment created in the wake of floating offshore wind turbines (FOWTs) is highly complex and currently not fully understood. Despite growing research efforts, most experimental and numerical studies focus on single rotors, given the large computational resource requirements. High-fidelity numerical investigations of multiple floating systems are limited. Critical aspects, such as the impact of turbine motion on wake evolution, wake interactions between FOWTs, and the effects on power generation, require further investigation.

This work aims to employ large eddy simulations in combination with a dynamic actuator line method to investigate wake interactions between two FOWTs in tandem. The analysis focuses on the International Energy Agency (IEA) 15MW wind turbine mounted on three floater types: semi-submersible, spar and tension leg platform. Historical wave and wind data from the European Center for Medium Range Weather Forecasts (ECMWF) dataset ERA5 are implemented. Both calm and extreme sea state conditions are reproduced. OpenFAST predicts the turbines' response to wave and wind forces, using the full-coupling integration implemented in AMR-Wind. The wake characteristics of the different FOWT configurations are examined under both laminar and realistic turbulent conditions and compared to the bottom-fixed reference case. Lastly, the power performances are analyzed.

Based on the literature findings, the following research questions are set to be answered:

1. **How does 6-DOF motion affect wake development and interactions of two tandem floating wind turbines?**
   (a) What differences can be observed between operations in calm and extreme sea state conditions?
   (b) How does wake evolution change between laminar and realistic turbulent inflow conditions?
2. **What are the key differences between TLP, Semi-Submersible, and Spar floating platforms?**
   (a) What kind of dynamic response do the platforms experience?
   (b) How does wake recovery compare to the fixed reference turbine?
3. **How does 6-DOF motion affect the power performance of two tandem floating wind turbines?**
   (a) Is the effect more pronounced on downstream or upstream floating wind turbines?

2 Methodology

2.1 Large-Eddy Simulations

To fully capture the physics of a turbulent flow across all temporal and spatial scales, CFD simulations must solve the Navier-Stokes equations directly. This is achieved through direct numerical simulations (DNS) using extremely fine computational grids, but demands significant processing power and data storage, rendering it impractical for most engineering applications. Reynolds-Averaged Navier Stokes (RANS) and its unsteady version (URANS) implement time-averaged equations and can be performed in a relatively short time, but they are not suited for highly unsteady and complex flows. Moreover, RANS tends to be overly diffusive for wind energy applications [29]. Large-eddy simulations (LES) provide a compromise between DNS and RANS by resolving the large, energy-containing eddies while modeling the smaller structures through subgrid scales (SGS) models. It was first proposed by Smagorinsky [101] and is based on the Kolmogorov's theory of self-similarity [102]. This states that the large eddies depend on the flow geometry, while smaller scales exhibit more universal behavior. LES applies a low-pass filter to decompose velocity into filtered and residual (SGS) components. Filtering can be explicit, achieved through a mathematical convolution function, or implicit, where numerical discretization provides artificial dissipation, effectively substituting SGS modeling. In practice, explicit filtering is rarely used due to the high computational costs.

The governing equations for LES for an incompressible flow can be obtained by filtering the incompressible Navier-Stokes equations:

$$\frac{\partial \bar{u}_i}{\partial x_i} = 0 \tag{1}$$

$$\frac{\partial \bar{u}_i}{\partial t} + \bar{u}_j \frac{\partial \bar{u}_i}{\partial x_j} = -\frac{1}{\rho}\frac{\partial \bar{p}}{\partial x_i} + \nu \frac{\partial}{\partial x_j}\left(\frac{\partial \bar{u}_i}{\partial x_j} + \frac{\partial \bar{u}_j}{\partial x_i}\right) - \frac{\partial \tau_{ij}}{\partial x_j} + \bar{f}_i \tag{2}$$

where $\bar{u}_i$ and $\bar{p}$ represent the filtered velocity and pressure, ρ the fluid density, ν is the kinematic viscosity and f_i the external forces, such as the ones introduced via the actuator method. Note that $\tau_{ij} = \overline{u_i u_j} - \bar{u}_i \bar{u}_j$ is the SGS stress tensor, which is analogous to the Reynolds-stress tensor.

In order to model a typical atmospheric boundary layer flow, additional source terms need to be introduced, as follows:

$$\bar{f}_i = C_i + B_i \tag{3}$$

$$C_i = -2\epsilon_{ijk}\Omega_j u_k \tag{4}$$

$$B_i = -g_i \beta \left(\theta - \theta_0\right) \tag{5}$$

where C_i is the contribution of the Coriolis forces due to Earth's rotation and B_i is the buoyancy term. Ω_j is the Earth's angular velocity, θ_0 is the reference ambient temperature, β is the thermal expansion coefficient, approximated as $\beta \approx 1/\theta_0$ and g_i is the gravity vector. Here the geostrophic forcing is also included, which drives the flow to a desired horizontal mean velocity. The potential temperature is then described by:

$$\frac{\partial \bar{\theta}}{\partial t} + \frac{\partial \bar{u_j} \bar{\theta}}{\partial x_j} = -\frac{\partial \tau_{\theta j}}{\partial x_j} + \frac{\nu}{\mathrm{Pr}} \frac{\partial^2 \bar{\theta}}{\partial x_j \partial x_j} \tag{6}$$

where $\tau_{\theta j} = \overline{\theta u_j} - \bar{\theta}\bar{u_j}$ is the heat flux term and $\mathrm{Pr} = 0.7$ is the laminar Prandtl number.

In ABL simulations, the Monin-Obukhov similarity theory is used for wall boundary conditions. The subgrid-scale stresses (τ_{i3}) and heat flux ($\tau_{\theta 3}$) need to be specified at the terrain boundary, with the friction velocity calculated as:

$$u_\tau = \frac{\kappa \overline{s}}{\ln\left(\frac{z_b}{z_0}\right) - \psi_m} \tag{7}$$

where κ is the von Karman constant, $\overline{s}$ is the horizontally averaged wind speed, z_0 is the roughness length and z_b is the the grid cell closest to the boundary. The profile near the wall is then determined by applying the logarithmic law of the wall:

$$u = u_\tau \left(\frac{1}{\kappa} \log\left(\frac{u_\tau z}{\nu}\right) + C\right) \tag{8}$$

where C is a constant. Equations 2 and 6 are unclosed and require a closure model to express the residual-stress tensor using information from the resolved scales. A common approach is to use the Boussinesq eddy viscosity assumption, which relates SGS shear stress to the strain rate tensor of the resolved scales:

$$\tau_{ij} - \frac{1}{3}\delta_{ij}\tau_{kk} = -2\nu_t \overline{S}_{ij} \quad \text{with} \quad \overline{S}_{ij} = \frac{1}{2}\left(\frac{\partial \bar{u}_i}{\partial x_j} + \frac{\partial \bar{u}_j}{\partial x_i}\right) \tag{9}$$

where ν_t is the eddy viscosity and $\overline{S}_{ij}$ is strain rate tensor. The subgrid-tensor is split into its deviatoric and isotropic parts - the latter can be neglected for incompressible flows [103]. The Smagorinsky SGS model [101] was the first to employ this concept and is still widely used. In this model, the eddy viscosity is written as:

$$\nu_t = (C_s\Delta)^2\sqrt{2\overline{S}_{ij}\overline{S}_{ij}} = (C_s\bar{\Delta})^2|\bar{S}| \tag{10}$$

where Δ is the grid size and C_s is the Smagorinsky constant.

Over the past decades, various alternative models have been developed. For example, the approach proposed by Germano et al. [104] in which the model constants dynamically and locally adjust, the wall-adapting local eddy-viscosity (WALE) model [105], which improves near-wall turbulence predictions or the Lagrangian-averaged scale-dependent (LASD) model [106]. However, studies have shown that the type of SGS model has only a limited impact in wind energy applications, with the characteristics of the inflow turbulence playing a more significant role [107, 108].

Recently, the anisotropic minimum-dissipation (AMD) model has been proposed by Rozema et al. [109], with an extension to thermally stratified flows by Abkar et al. [110]. The eddy viscosity in a field without temperature field is calculated using an anisotropic derivative with a different filter width in each direction:

$$\nu_t = \frac{-(\hat{\partial}_k\bar{u}_i)(\hat{\partial}_k\bar{u}_j)\bar{S}_{ij}}{(\partial_l\bar{u}_m)\,(\partial_l\bar{u}_m)} \tag{11}$$

where $\hat{\partial}_i = \sqrt{C}\delta_i\partial_i$ is the anisotropic derivative operator, $C = 1/3$ is the Poincare coefficient for a second-order accurate scheme and δ_i is the filter width along dimension i for anisotropic grids. In practical implementations of the AMD model, the filter width is typically chosen to match the grid size, i.e. $\delta_i = \Delta_i$. For the derivation in a thermally stratified flow refer to [110].

To assess whether an LES simulation is well-resolved, Pope [111] suggested that the ratio of resolved turbulent kinetic energy to total kinetic energy (including modelled contributions) should exceed 80%. However, other researchers, such as Davidson [112], have questioned the reliability of this criterion as a definitive measure of LES quality.

2.2 Actuator Line Method

The Actuator Line Model (ALM) was first introduced by Sørensen & Shen [113] to simulate wind turbine wakes. Instead of explicitly resolving the boundary layer around turbine blades, ALM represents their effects by projecting body forces directly onto the computational domain (see Figure 12). ALM significantly reduces computational costs compared to fully resolved simulations by eliminating the need for high-resolution mesh refinement around the blades. For this reason, it has been widely employed to study flow fields in wind farms, and interactions between wind turbines and the atmospheric boundary layer.

This approach employs BEM theory, where aerodynamic forces at discrete blade positions are computed using airfoil data retrieved from lookup tables:

$$\boldsymbol{f}_i = F_l \boldsymbol{e}_l + F_d \boldsymbol{e}_d \tag{12}$$

$$F_l = \frac{1}{2}\rho c w C_l(\alpha) U_{rel}^2 \qquad F_d = \frac{1}{2}\rho c w C_d(\alpha) U_{rel}^2 \tag{13}$$

where $\boldsymbol{f}_i$ is the aerodynamic force vector of each actuator point, F_l and F_d the lift and drag force respectively, α is the angle of attack, c is the local chord, w is the width of the blade element and U_{rel} is the relative velocity. The latter is calculated as the difference between the sampled fluid velocity at the specific actuator point $\boldsymbol{u}(\boldsymbol{x_i})$ and the velocity $\dot{\boldsymbol{x}}$ of the i_{th} actuator point. The position of the points is updated at every time step based on the rotational speed of the wind turbines, the blade deflections and the platform movements when adopting a FOWT.

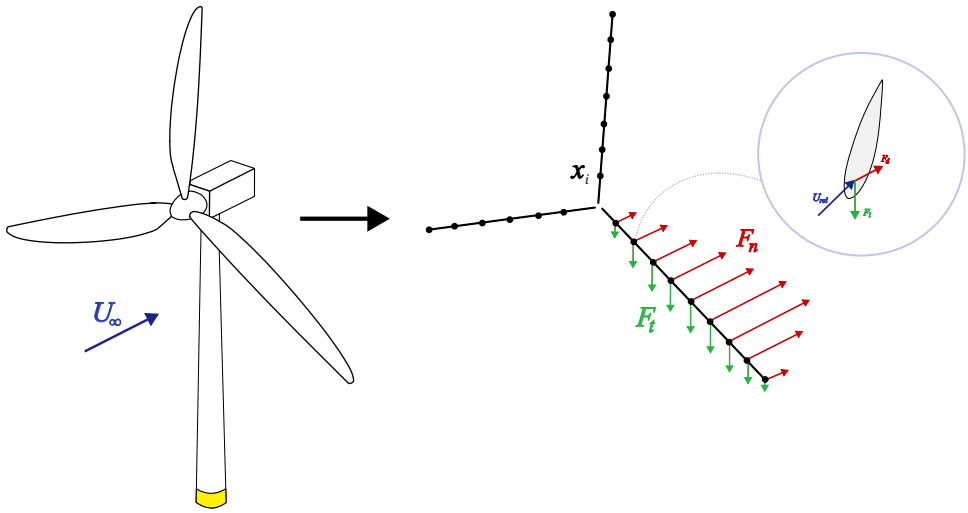

Figure 12: Schematic of the actuator line technique.

To maintain numerical stability and avoid unphysical discontinuities, a Gaussian isotropic smearing function was originally employed to distribute these forces over a small region around each actuator point, as described by:

$$\boldsymbol{f}_\epsilon = \boldsymbol{f}_i \otimes \eta_\epsilon \tag{14}$$

$$\eta_\epsilon(x, y, z) = \frac{1}{\epsilon^3 \pi^{3/2}} \exp\left(\frac{(x - x_0)^2 + (y - y_0)^2 + (z - z_0)^2}{\epsilon^2}\right) \tag{15}$$

where ϵ is the thickness of the regularization function, x, y and z are the three coordinate directions; and x_0, y_0, and z_0 are the location about which the Gaussian is being applied.

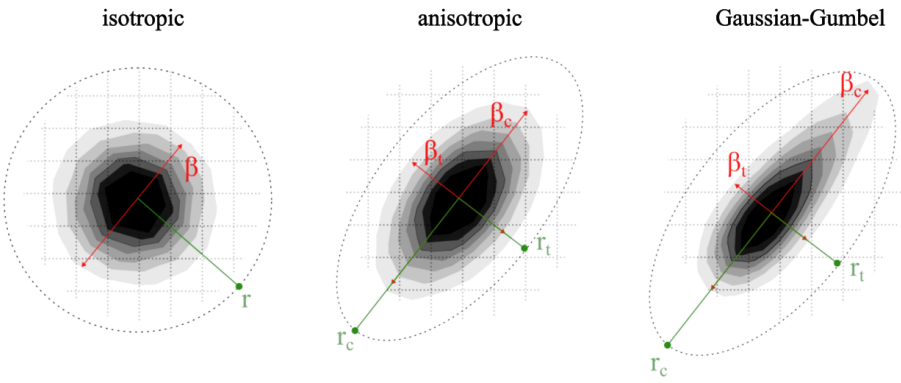

Figure 13: Representation of three different kernel functions. Adapted from Melani et al. [114]

Figure 13 shows a comparison of different kernel functions that have been introduced over the years to improve the representation of the wind turbine blades. In particular, the anisotropic function by Churchfield et al. [115] and the Gaussian-Gumbel function by Schollenberger et al. [116]. AMR-Wind features the anisotropic Gaussian body force representation, described as follows:

$$\eta_\epsilon(x_c, x_t, x_r) = \frac{1}{\epsilon_c \epsilon_t \epsilon_r \pi^{3/2}} \exp\left[-\left(\frac{x_c - x_{c,0}}{\epsilon_c}\right)^2 - \left(\frac{x_t - x_{t,0}}{\epsilon_t}\right)^2 - \left(\frac{x_r - x_{r,0}}{\epsilon_r}\right)^2 \right] \quad (16)$$

where x_c, x_t and x_r are the coordinates in the chord-wise, thickness-wise and radical directions.

The most accurate predictions of the velocity field on a wind turbine blade can be achieved using a smoothing width between 14%-25% of the chord length of the blade, i.e. $\epsilon_{opt} = 0.14c - 0.25c$, independently of the angle of attack [117]. However, this is a much finer value that can be resolved in a practical LES. In order to correct for this discrepancy caused by larger a mesh size, Martínez-Tossas et al. [118, 119, 120] introduced an analytical function called the Filtered Lifting Line Correction (FLLC). This expresses the induced velocity along the wind turbine's blade as the solution to the following:

$$u'_x(r) = -\int_0^R \frac{dF'_l(r')}{dr'} \frac{\left(1 - e^{-(r-r')^2/\epsilon(r')^2}\right)}{U_\infty(r')\, 4\pi\, (r - r')} dr' \quad (17)$$

where F'_l is the lift force per unit span and r the blade spanwise coordinate. This feature has been implemented and validated in AMR-Wind.

To account for the presence of the wind turbine tower, a fixed actuator line can be used by superimposing body forces to the upcoming flow. The nacelle can be modeled as a bluff body using the immersed boundary (IB) method.

2.3 OpenFAST

OpenFAST [121] is a multi-physics, multi-fidelity tool for simulating the coupled dynamic response of wind turbines. It integrates various modules, including aerodynamics, hydrodynamics for offshore structures, control system dynamics, and structural dynamics, enabling comprehensive nonlinear aero-hydro-servo-elastic simulations in the time domain. Wind turbines can be modeled as onshore or offshore, with the possibility to include floating substructures. The framework is modular and one can choose which module to activate in the main (*.fst*) file. For the current work, OpenFAST v4.0.4 is used, which present significant improvement over the previous versions and better integration with AMR-Wind.

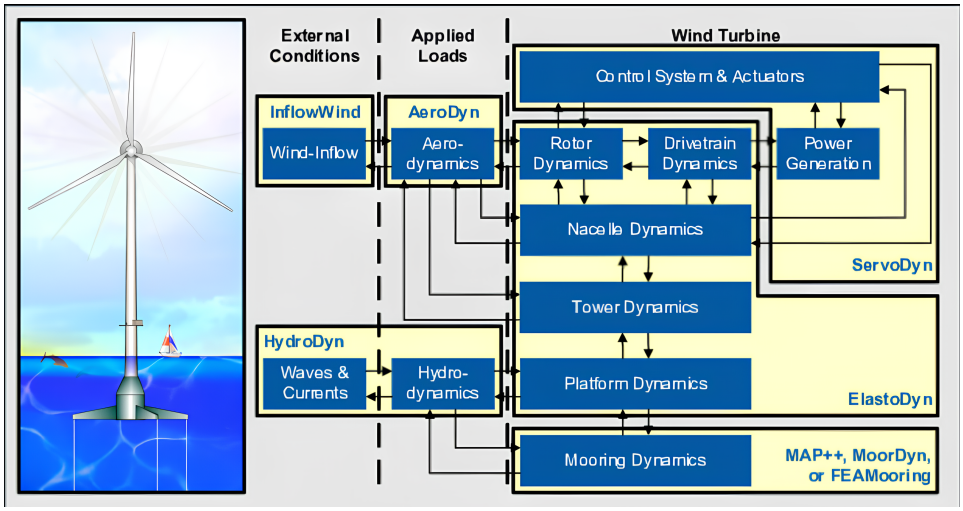

Figure 14: OpenFAST schematic [121].

The full list of inputs for some of the modules can be found in the Appendix-D. Below is a brief summary highlighting the key features implemented from each module.

- Aerodyn: Prandtl tip and hub loss corrections are applied. Tower aerodynamics are disabled for the corresponding simulations. The dynamic blade element momentum (DBEM) theory is activated, using Oye's discrete-time model with varying τ. Unsteady airfoil aerodynamics is modeled using an extension of the Beddoes-Leishman model by Minnema/Pierce. Skew correction is applied using the Glauert/Pitt/Peters model.
- Elastodyn: blade and tower structural dynamics are deactivated. The `GenDOF` is set to `True`. The blade pre-cone and shaft tilt are both set to zero. The blades are modeled with 300 blade nodes, following the recommendations described in the FLLC method. The BeamDyn module is included for the monopile configuration.

- SeaState: the JONSWAP spectrum is used to generate wave data. Second-order waves are included, while current modelling is disabled (see Section 2.3.1)
- Hydrodyn: platform modelling combines potential flow theory (based on WAMIT outputs) with strip theory. Second-order forces are not included.
- Moordyn: the length of mooring lines matches the values from the original design of the platforms (see Section 3.2).
- Servodyn: the ROSCO monopile controller is used for the bottom-fixed wind turbine simulations, while the controller of the U-Maine semisub is employed for the floating simulations.

Prescribed harmonic motion is implemented in OpenFAST using the method described by Amaral et al. [122]. This consists of applying force time histories through the ExtPtfm module to obtain the desired motion, by modelling the foundation as a super-element characterised by mass m_{ij}, damping c_{ij}, and stiffness k_{ij} tensors.

OpenFAST files of the IEA-15MW monopile [123] and U-Maine semi-submersible configurations [124] are retrieved from the main IEA Wind Systems git repository. The WindCrete spar [125] is accessed through its official website. The turbine's and platforms' specifications for these models are publicly available and are not documented here for conciseness. Files for the GICON's TLP are provided by the INF4INITY project partners.

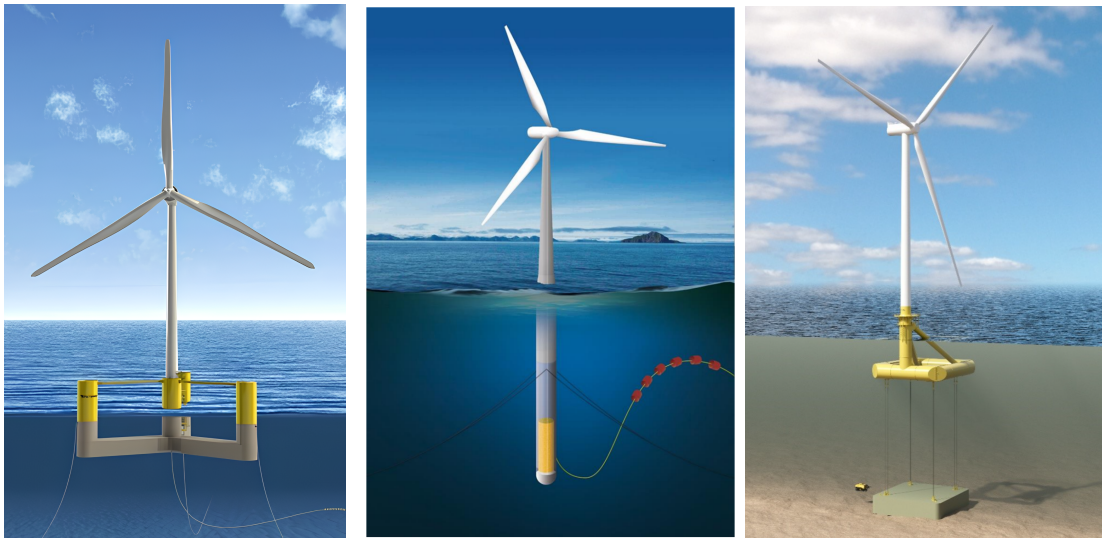

Figure 15: From left to right: the IEA-15MW wind turbine mounted on the U-Maine semisub [126], the WindCrete spar [127] and GICON's tension-leg platform [128].

2.3.1 Sea State Generation

The wave field is generated within the SeaState module, employing both linear Airy theory and second-order wave theory in combination with the JONSWAP spectrum to simulate irregular waves. Current effects are not included in the model. The waves are aligned with the direction of the incoming wind. Figure 16 shows the wave elevation time series for a calm sea at the locations of the two simulated wind turbines: the first at the "Origin", and the second located either 3D or 5D downstream. A similar plot for a rough sea state can be found in the Appendix-A. To compute the wave conditions at the latter positions, a spatial propagation of the wave field is performed using wave theory. For linear waves in finite water depth, the dispersion relationship relates the wave number k_n to the wave frequency ω_n as follows:

$$k_n \tanh(k_n h) = \frac{\omega_n^2}{g} \tag{18}$$

where h the water depth and g the gravitational acceleration.

Once the wave numbers are determined, the wave elevation $\eta(t, X, Y)$ at a spatial point (X, Y) and time t can be obtained via an Inverse Discrete Fourier Transform (IDFT). This is based on the complex wave amplitude spectrum H_n, defined at the origin $(0, 0)$:

$$\eta(t, X, Y) = \text{IDFT}\left(H_n \cdot e^{-ik_n(X\cos\beta + Y\sin\beta)} \cdot e^{i\omega_n t}\right) \tag{19}$$

where β denotes the wave propagation direction relative to the X-axis.

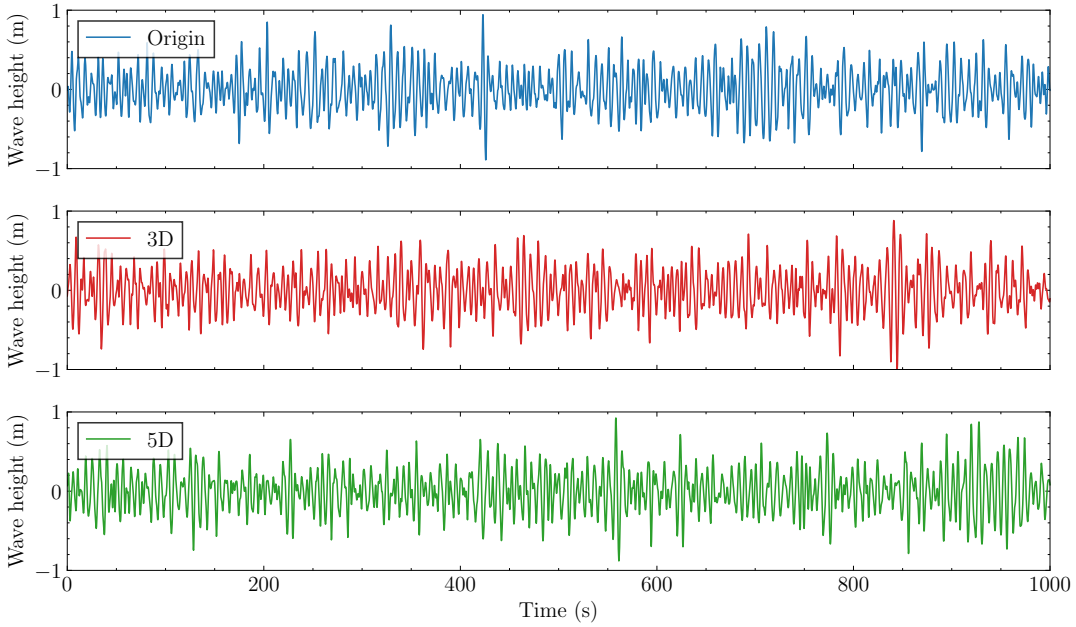

Figure 16: Wave height evolution of the calm sea case at different spatial locations.

In all simulations, WaveMod is set to 5, enabling the use of externally generated wave-elevation time series. According to the OpenFAST documentation, the input wave-elevation time series is assumed to be first-order, while second-order components are internally computed based on this input. The wave signal is therefore provided to OpenFAST without including second-order terms directly.

2.4 GICON's 5th Generation Platform

The INF4INITY project (INtegrated designs for Future Floating oFFshore wINd farm TechnologY) [129] focuses on the development of a tension-leg platform that integrates nature-inclusive features for subsea components, enabling co-use with marine aquaculture. The design incorporates an innovative gravity anchor and features self-stabilization during transport and installation, facilitating easier and more efficient deployment. The project targets parameters that support the economic viability of floating substructures based on the TLP concept. Its goal is to create a universal structural platform adaptable to various deployment sites through scalable and modular components.

The project is led by GICON, which is developing the concept using its existing GICON-SOF technology, suitable for water depths ranging from 45 to 350 meters. For the current work, design iteration 2 is used, intended for a water depth of 122 m. Further design modifications are expected as development progresses.

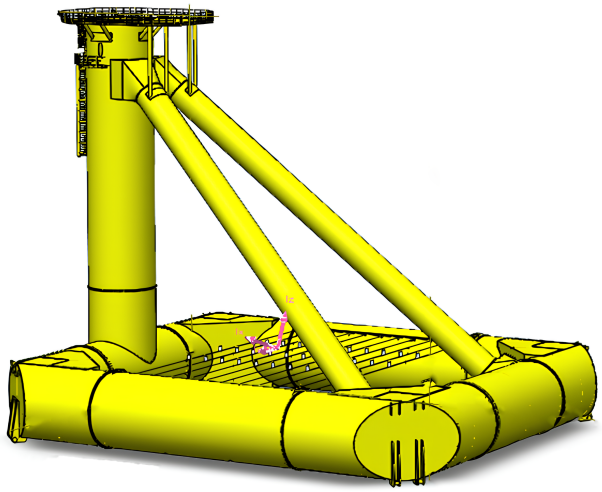

Figure 17: 3D rendering of the GICON's floater [128].

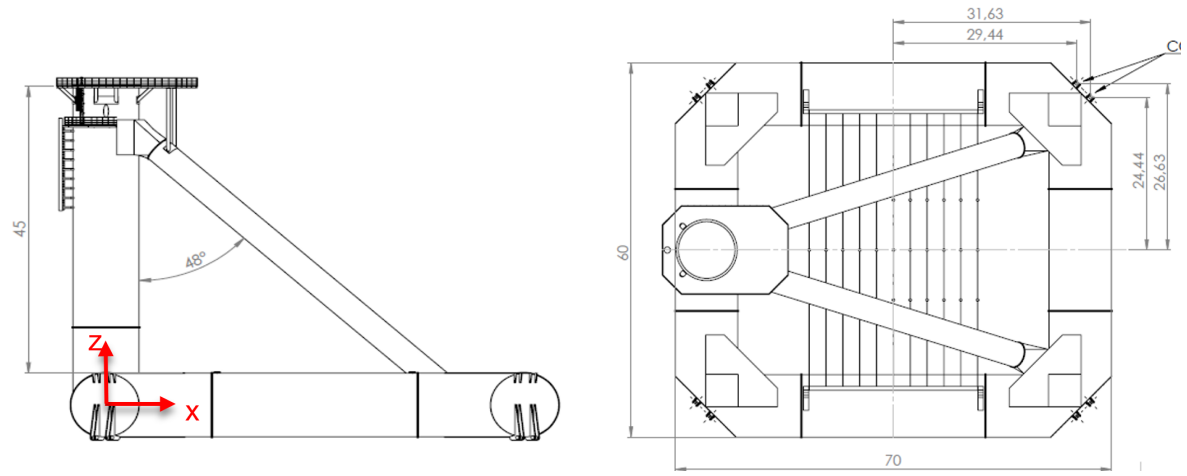

(a) Side view. (b) Top view.

Figure 18: Technical drawings of the GICON's floater [128].

The design strategy revolves around a symmetrical, modular, four-sided layout to gain manufacturing and assembly advantages over the smaller existing GICON-TLP. The buoyancy bodies are configured as cylindrical monopile structures. This configuration is chosen due to its suitability for buoyancy generation, supported by established and partially automated manufacturing techniques. Other benefits include an efficient hydrodynamic pressure distribution in submerged environments with thinner outer shells and fewer stiffeners. These structural elements have a diameter of 10m, resulting in high production capabilities globally. Horizontal alignment maximizes buoyancy volume with the same footprint (as opposed to vertical alignment) and offers a shallower draught. Additionally, these large structural elements are deliverable for assembly without needing lifting, eliminating the requirement for a suitable crane.

The mooring lines consist of FibreMax aramid cables, manufactured using Twaron, a high-performance aramid fiber developed by Teijin Aramid. They have been selected for their exceptional mechanical strength and long-term durability. These characteristics make them particularly well-suited for demanding applications such as deepwater mooring, offshore wind platforms, bridge stays, marine lifting, and aerospace systems. To model the mooring lines in OpenFAST, Moordyn is employed.

Free decay tests are conducted to determine the natural periods of the platform and are summarized in Table 6. The results are compared with those of the U-Maine semisub and the WindCrete spar. Initial displacements for all platforms are adopted from the Semisub report [126]. It is important to note that the WindCrete spar results are based on the optimized MoorDyn configuration (second design iteration), which differs from the 2021 report where this optimization had not yet been implemented.

Table 4: GICON's tension-leg platform structural and hydrodynamic properties.

Paramater	**Value**
Mass (primary steel)	6029 ton
Mass (primary steel + surcharge + ballast)	8063 ton
Center of gravity (x, y, z)	(25.97, 0.0, 5.45) m
Overall length	70 m
Overall width	60 m
Overall height	55 m
Bouyancy volume	20100 m^3
Platform draft	38 m
Platform inertia for roll tilt rotation	3.329×10^9 kgm^2
Platform inertia for pitch tilt	5.034×10^9 kgm^2
Platform inertia for yaw rotation	7.032×10^9 kgm^2

Table 5: GICON's tension-leg platform mooring lines properties.

Paramater	**Value**
Overall length	78 m
Overall number	8
Diameter	276.95 mm
E-Modulus	69 GPA
Minimum breaking load	7000 ton
Pretension (per cable)	12.95 MN

Table 6: Floaters' natural frequencies in Hertz.

	Surge	**Sway**	**Heave**	**Pitch**	**Roll**	**Yaw**
GICON's TLP	0.038	0.032	0.348	0.343	0.294	0.066
U-Maine Semi-sub	0.007	0.007	0.049	0.036	0.036	0.011
Windcrete Spar	0.022	0.022	0.030	0.024	0.024	0.059

2.5 AMR-Wind

AMR-Wind [91, 92] is a massively parallel, block-structured adaptive-mesh solver designed for incompressible flow simulations of wind turbines and wind farms. It is built on top of the AMReX library, which provides essential functionalities, including mesh data structures, adaptive meshing, and linear solvers for solving the governing equations. It uses a second-order finite method and second-order temporal integration to solve the discretized Navier-Stokes equations. The main applications of AMR-Wind include: conducting large-eddy simulations of ABL flows and modeling wind farm turbine-wake interactions using actuator disk or actuator line methods. Additionally, it can be coupled with Nalu-Wind, a near-body flow solver, to perform blade-resolved simulations of multiple wind turbines within a wind farm. The software fully leverages GPU acceleration and is compatible with a wide range of hardware. As of today, the code has been successfully used to simulate a wind farm of over 500 turbines in a 100 km x 100 km domain [130].

In the current work, AMR-Wind is compiled using Spack through the Exawind-Manager on the dedicated DTU high-performance computing (HPC) cluster [131], with GCC v12.4.0. Simulations are executed in parallel using MPI on Lenovo ThinkSystem SD530 and with NVIDIA A100 and V100 GPUs. The setup and post-processing of the simulations can be performed via the AMR-Wind frontend tool, which is a program based on Python developed by Lawrence Cheung. Additional key features are implemented in this tool to enable the generation of the figures in this report.

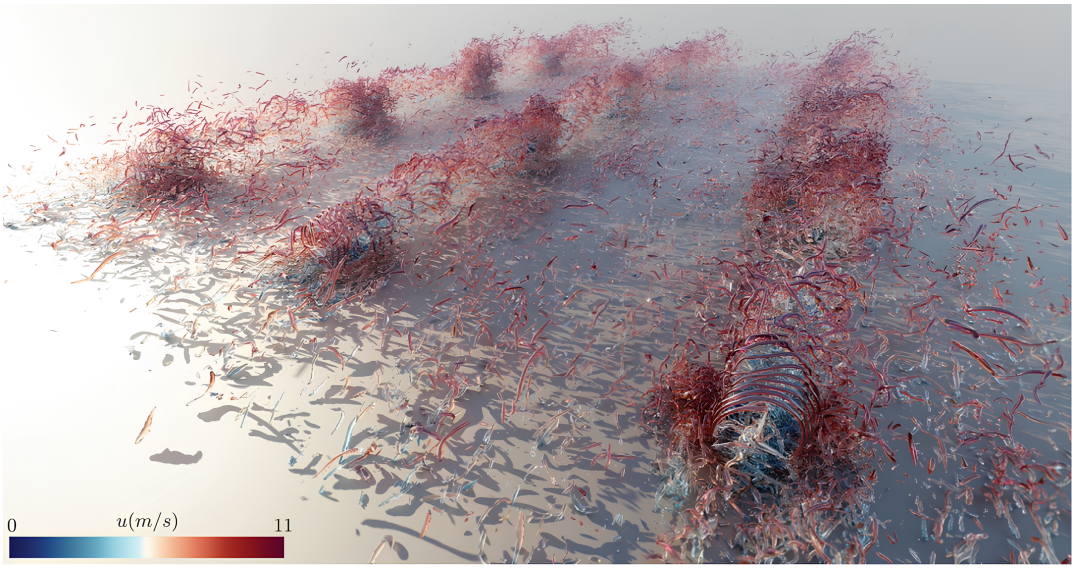

Figure 19: Isosurface of Q-criterion of a small wind farm simulation using AMR-Wind. Reproduced from Kuhn et al. [92]

3 Simulation Setups

3.1 Site Selection

The selection of the wind turbines' site is based on the data analysis on the Scottish Sea performed by Penalba et al. [132], as part of the INF4INITY project deliverables. This study includes metocean data, statistical analysis and site-specific design load cases (DLCs) across different offshore areas. The sources of the data include ERA5 - the fifth generation ECMWF reanalysis for global climate, along with the Copernicus Marine Service and the European Marine Observation and Data Network. Key parameters such as main wind, waves and mean-sea level characteristics are retrieved from ERA5. The dataset spans over 20 years, with a temporal resolution of 1 hour. For the current work, the period 2000-2020 is chosen.

The Scottish east coast of the North Sea has received the most attention for the development of floating wind farms. From the available dataset, the location with the greatest water depth is selected to better align with the design specifications of the existing floating platform models, which are intended for depths around 200 m. This site is located at 60.0°N, 0°W and has a water depth of 146 m. Although it differs from the optimal sites identified through the multicriteria ranking in Task 5.2 of the INF4INITY project, its wind and wave conditions are expected to be comparable to those at one of the selected sites - Location B (59.0°N, –2.0°W).

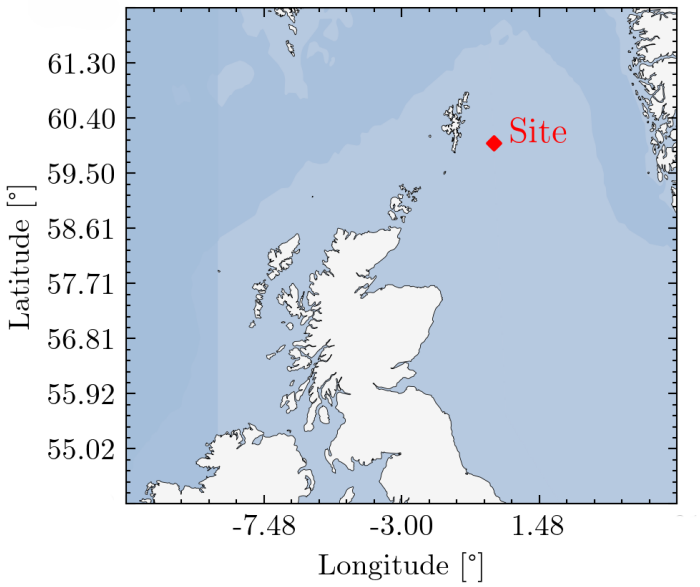

Figure 20: Geographical map of the Scottish Sea. In red, the selected wind site location.

Figure 21 illustrates the distributions of wind speed and significant wave height at the site, while Figure 22 shows the joint probability distribution of significant wave height and wave peak period for $U_{hub} = 10$ m/s. These figures highlight the most frequently occurring sea states, which serve as the basis for selecting the design load cases used for the simulations explained in Section 3.2.

Due to the low temporal resolution of the available data, it is not possible to reliably estimate the reference turbulence intensity (TI) directly from the wind speed signal. Instead, it is determined from existing offshore measurements in the North Sea. Notably, Marek et al. [133] report TI values of 5–6% around the British Isles, and similar levels are observed at the FINO1 met mast [134]. As indicated by these studies, relying solely on the International Electrotechnical Commission (IEC) standard guidelines to determine the TI would significantly overestimate its magnitude around this region.

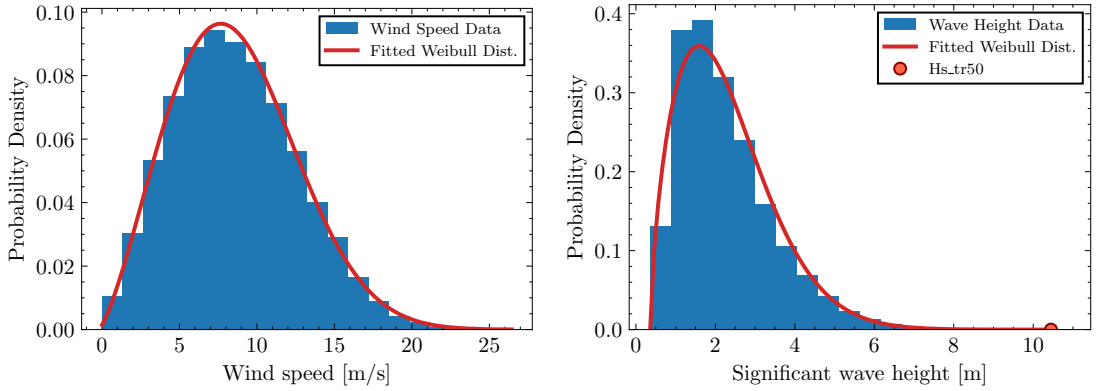

Figure 21: Probability density function of wind speed and significant wave height at site.

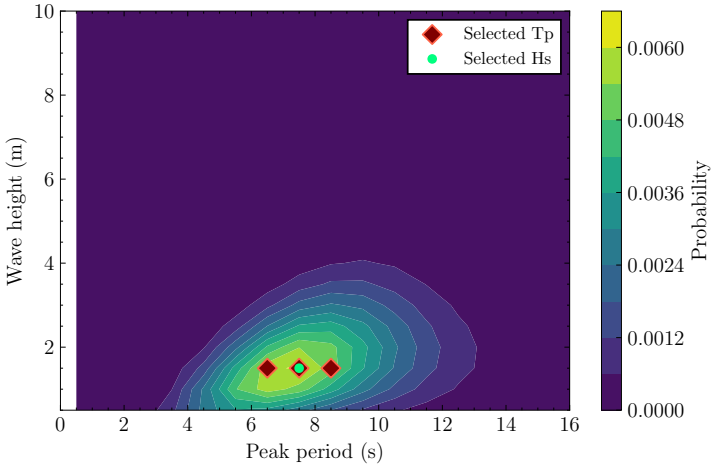

Figure 22: Joint probability between significant wave height and peak period for $U_{hub} = 10$ m/s.

3.2 Design Load Cases

The Design Load Cases (DLCs) are grouped into laminar inflow cases (Table 7) and turbulent sheared inflow cases (Table 8). For the latter, a conventionally neutral boundary layer is imposed. The selection of sea state conditions is based on the data analysis described in the previous section. A key focus is to investigate the interactions between closely spaced FOWTs, as this has implications for potentially more compact wind farm layouts. In all scenarios, wind and wave directions are set to be aligned.

Table 7: Wind turbines layout and environmental conditions for laminar cases.

Case	$\boldsymbol{\Delta/D}$	**Platform**	**Sea state**	$\overline{\boldsymbol{U}}_{\boldsymbol{hub}}$ [m/s]	$\boldsymbol{H_s}$ [m]	$\boldsymbol{T_p}$ [s]
1	3	Fixed	Calm	10.59	1	7.5
2	3	TLP	Calm	10.59	1	7.5
3	3	Spar	Calm	10.59	1	7.5
4	3	Semi-sub	Calm	10.59	1	7.5
5	5	Fixed	Calm	10.59	1	7.5
6	5	TLP	Calm	10.59	1	7.5
7	5	Spar	Calm	10.59	1	7.5
8	5	Semi-sub	Calm	10.59	1	7.5
9	5	TLP	Extreme	10.59	10	12
10	5	Spar	Extreme	10.59	10	12

Table 8: Wind turbines layout and environmental conditions for neutral ABL cases.

Case	$\boldsymbol{\Delta/D}$	**Platform**	**Sea state**	$\overline{\boldsymbol{U}}_{\boldsymbol{hub}}$ [m/s]	**TI** [%]	$\boldsymbol{H_s}$ [m]	$\boldsymbol{T_p}$ [s]
11	3	Fixed	Calm	10.59	5	1	7.5
12	3	TLP	Calm	10.59	5	1	7.5
13	3	Spar	Calm	10.59	5	1	7.5
14	3	Semi-sub	Calm	10.59	5	1	7.5
15	5	Fixed	Calm	10.59	5	1	7.5
16	5	TLP	Calm	10.59	5	1	7.5
17	5	Spar	Calm	10.59	5	1	7.5
18	5	Semi-sub	Calm	10.59	5	1	7.5
19	5	TLP	Extreme	10.59	5	10	12
20	5	Spar	Extreme	10.59	5	10	12

To model the floating systems under investigation, a hybrid approach combining potential-flow theory and strip theory (Morison formulation) is implemented in the HydroDyn module. Second-order hydrodynamic forces are not considered in this analysis. Additionally, the original mooring line designs for each floater are preserved, meaning the systems are simulated as if operating at their original design water depths—200 meters for the semisubmersible and spar, and 124 meters for the TLP. This choice is based on several considerations. First, when generating wave time series, the wave characteristics remain essentially unchanged for a small variation in water depth (e.g., from 200 m to 146 m, as in the selected site). Because the depth difference is minor, it is reasonable to assume that the floater's hydrodynamic response would remain mostly unaffected. Second, changing the water depth would necessitate modifications to the mooring system design, such as shortening the cables. The goal would then be to ensure that the floater's dynamic response remains comparable across different depths. Finally, even if mooring adjustments were made, updated hydrostatic matrices would be required from a frequency-domain wave-body interaction solver at the new depth, something which is outside the scope of the current work.

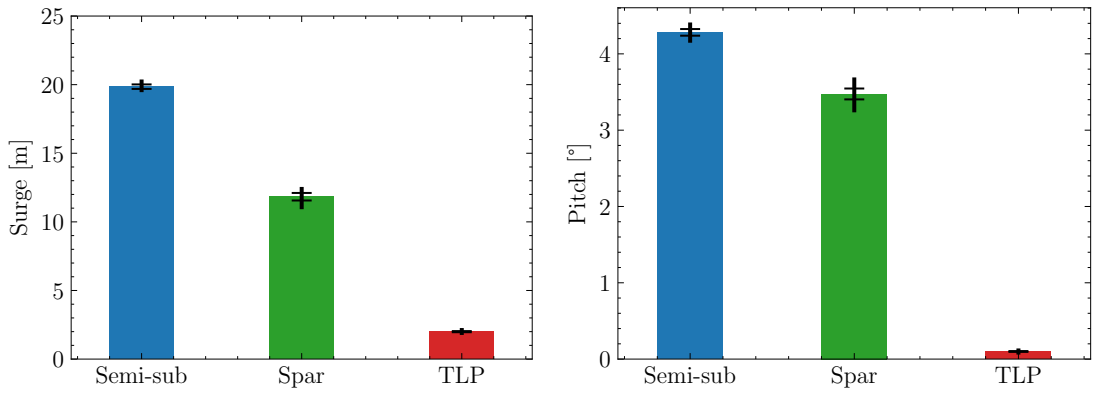

Figure 23: Comparison of the floaters' mean motion dynamics under calm waters.

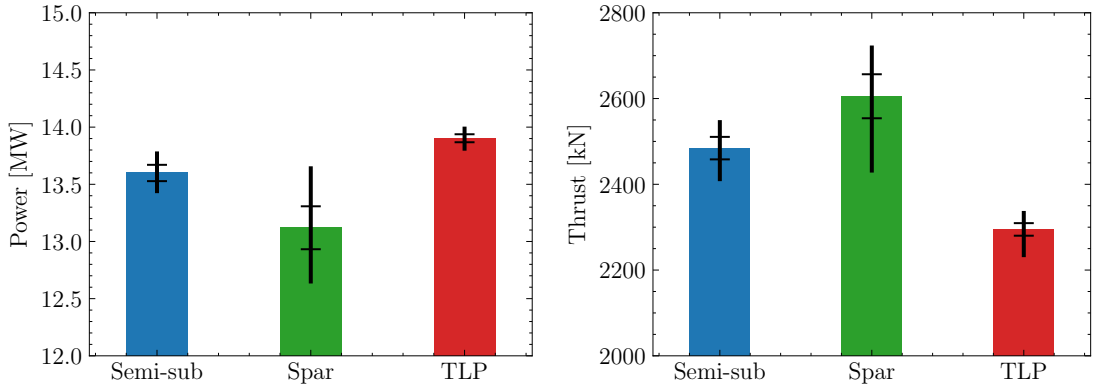

Figure 24: Comparison of the floaters' mean power and thrust under calm waters.

To eliminate start-up transient effects, the initial part of each simulation is discarded. Figure 23 and 24 show the dynamics and performance of the single floaters during the calm sea state. As can be seen, the semisub exhibits the largest mean motions, while the Spar has the largest fluctuations over time. The TLP is the stiffest of the platforms.

3.3 Flow Solver

LES are performed by solving the incompressible Navier–Stokes equations, supplemented with a SGS model, using the massively parallel AMR-Wind solver. Second-order spatial and temporal discretization schemes are employed. The former integrates both the finite-volume and finite-element methods. Advection is treated explicitly using a Godunov-type upwind scheme, namely the Weighted Essentially Non-Oscillatory (WENO-Z) algorithm [135]. Temporal integration is carried out using the Crank Nicolson scheme. Several SGS models are evaluated, but ultimately, the AMD model is used.

The CNBL is generated by simulating a flow with no temperature stratification within the surface layer. The wind speed is forced at the desired mean velocity at the hub height of 150 m by enabling the ABLForcing source term in AMR-Wind, which applies a uniform vector term to the entire domain to mimic the atmospheric pressure gradient. The desired turbulence intensity ($\approx 5\%$) is achieved by varying the surface roughness and is obtained at $z_0 = 0.012$. The flow is initialized with a surface temperature of 290° K and the surface heat flux set to zero. In all simulations, the Boussinesq buoyancy model is included to capture any temperature changes effects. The Coriolis forcing is ultimately discarded due to inconsistencies in the imposed flow direction when transitioning into the refined mesh regions. The CNBL simulations are carried out in two stages. First, a precursor simulation with periodic boundary conditions is run to develop a turbulent atmospheric flow. Once a statistically steady state is reached— identified by the convergence of energy content and horizontally averaged vertical profiles— data from the boundary cross-sectional plane is extracted and stored for use as initial conditions in the main simulation.

The IEA-15MW wind turbine is represented as body forces in the momentum equations using actuator line models. At the start of each time step, AMR-Wind provides sampled velocities at actuator points to OpenFAST, which then advances the turbine dynamics and returns updated actuator point forces and positions to AMR-Wind.

3.4 Computational Domain and Boundary Conditions

The numerical setup differs between the laminar inflow and the CNBL cases. For the former, the preliminary single-turbine simulations use a domain size of $10D \times 5D \times 5D$, which is extended to $13D$ and $15D$ in the streamwise direction for the tandem configu-

rations. The blockage ratio is approximately 3%, which provides sufficient accuracy at a reasonable computational cost. A steady, uniform inflow wind speed of $U = 10.59$ m/s is applied at the inlet boundary, while a pressure outlet boundary condition is imposed at the outflow. The other planes are set as periodic. The computational mesh consists of an isotropic base grid with a resolution of 20 m, with three levels of refinement being applied in a cylindrical shape, resulting in a minimum grid spacing of $\Delta x = 2.5$ m (or $D/96$). For the $5D$-spaced wind turbines cases, the total cells reaches 36 million.

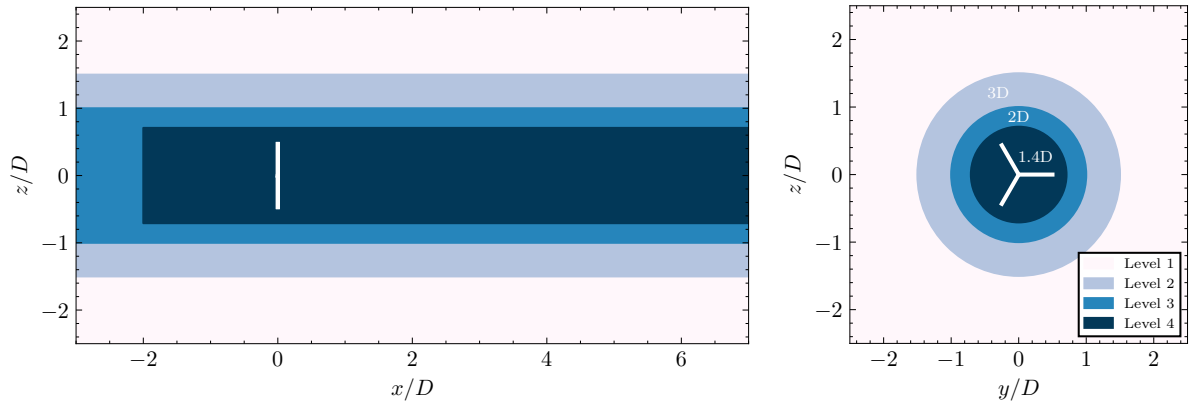

Figure 25: Mesh refinement in the single turbine domain for the laminar case.

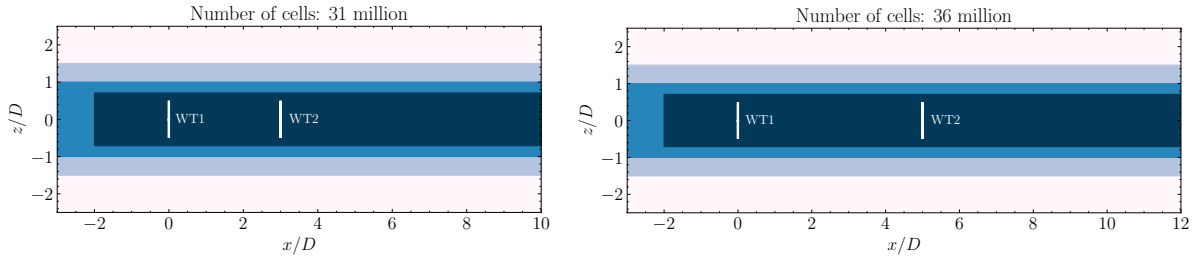

Figure 26: Mesh refinement in the two turbines domain for the laminar case.

The first wind turbine is placed $3D$ downstream from the inflow boundary, with the hub height aligned at the mid-plane along the vertical (z) direction. The rotor blades are discretized using 300 points, and a Gaussian width in all directions of $\epsilon/\Delta x = 1.0$ is used. The FLLC is implemented using the recommended settings to ensure results remain within 1% of the converged solution, specifically $\epsilon/c = 0.25$ and $\epsilon/\Delta z = 6.25$ (see Table 1 in [120]).

The time step for all scenarios is fixed at 0.02 s to ensure that the blade tip does not traverse more than one grid cell per time step. At the imposed rated inflow speed, the tip velocity reaches 90 m/s, but including pitch and surge effects, it increases up to 100 m/s. This results in a tip displacement of approximately $0.8\Delta x$ per time step. The Courant

number is below the critical value of 1. The total simulation time is determined by the need to achieve a converged flow field and eliminate transient startup effects in the wind turbine motions introduced by OpenFAST. The simulations for the single turbine, $3D$ spacing, and $5D$ spacing configurations are then run for total durations of 600 s, 800 s, and 1000 s, respectively. A brief study to verify statistical convergence is reported in Appendix-B. The averaged flow quantities are calculated using the last 200 s of each simulation. The simulations require approximately 48 to 60 hours to complete and are run either using one NVIDIA Tesla A100 (80GB) or two Tesla V100 (32GB) GPUs. For the latter, a single checkpoint restart is required due to the strict 24-hour usage limit.

In the CNBL cases, the precursor and successor domains extend for $17D \times 10.6D \times 4D$, based on the recommendations by Brasseur and Wei [136]. On the lower surface, the log-law wall model is applied, while the top boundary is set to slip-wall. The base grid is isotropic, with a uniform resolution of 20 m. The precursor simulation includes one level of grid refinement (up to $\Delta x = 10$m), which is the minimum resolution required to achieve accurate ABL statistics according to Wurps et al. [137]. This domain accounts for approximately 4.6 million.

To allow the turbulence to sufficiently develop, the precursor is run with periodic boundary conditions for a total of 5 hours, using a time step of 0.25 s. After this spin-up period, the simulation proceeds for an additional 1000 seconds, during which data is recorded using a time step of 0.04 s. Following a similar approach by Navarro et al. [138], the successor simulation employs two additional levels of grid refinement, to achieve a finer resolution near the turbines of $\Delta x = 2.5\,\text{m}$. Once the flow enters the refined region, it travels 720 m (or $3D$) before reaching the first wind turbine, which is deemed long enough to develop the eddy structures in the new finer mesh. The largest ABL domain contains 42 million cells. An input file for both the laminar inflow and ABL cases can be found in the Appendix-E.

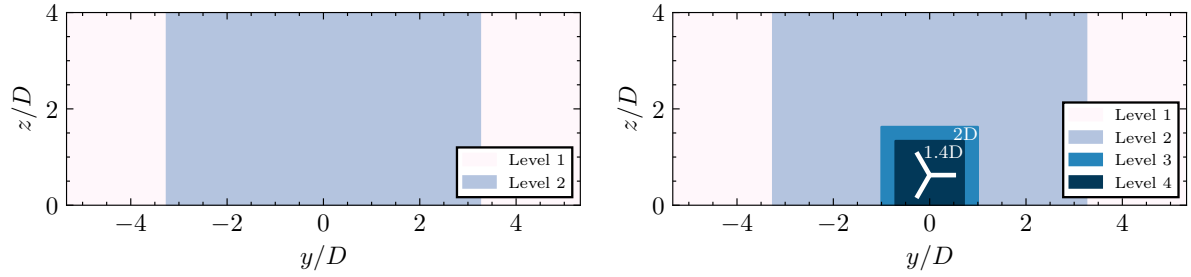

(a) Spin-up and Precursor

(b) Successor

Figure 27: Mesh refinement for the neutral ABL cases.

Mean profiles of flow quantities for the CNBL simulations are shown in Figure 27 and 28. The results show good agreement with the typical values for similar atmospheric conditions.

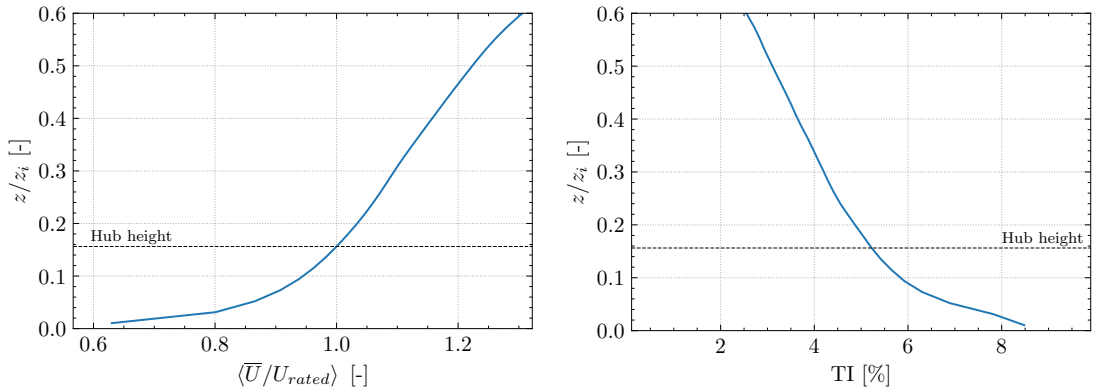

Figure 28: Averaged velocity and turbulence intensity in the neutral ABL cases.

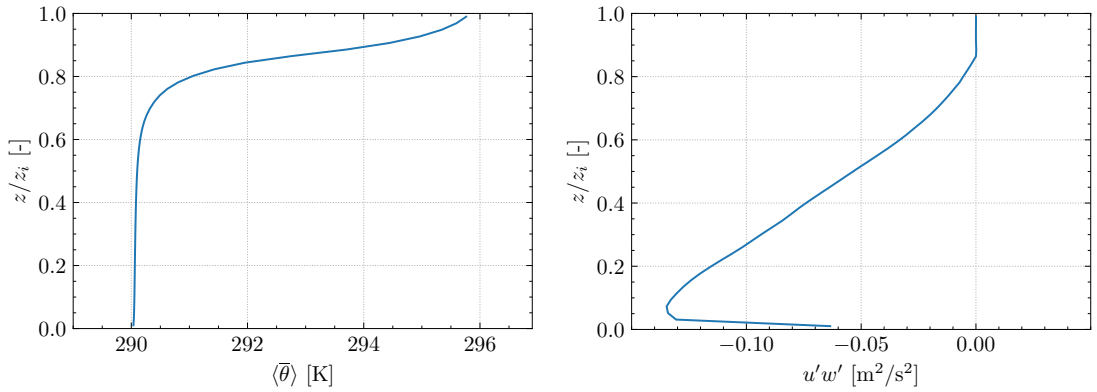

Figure 29: Averaged temperature and Reynolds stress in the neutral ABL cases.

3.5 Sampling

Data is collected throughout the entire simulation at a frequency of $f = 0.5\,\text{Hz}$. The figures are generated from planar slices taken from the xy- and xz-planes located at the center of the domain, extending from $-2D$ to $11D$ downstream and aligned with the hub height. A total of 29 vertical probes are placed at intervals of $1D$, beginning at the first turbine and spanning vertically from $-1D$ to $1D$. For the ABL simulations, horizontal probes are also employed using a similar pattern.

The mean flow quantities in the wake are computed by first time-averaging the recorded values at each probe location. These local time-averaged values are then spatially averaged across all cross-sectional planes. A similar procedure is used to compute the mean turbulence intensity within the wake region. To determine the vertical and horizontal wake centers, a method similar to that described by Howland et al. [139] is employed. Here, the wake center is defined as the weighted average of the velocity deficit along the spanwise coordinate:

$$z_c(x) = \frac{\sum z_i \cdot (U_\infty - U_i)}{\sum (U_\infty - U_i)} \quad \text{and} \quad y_c(x) = \frac{\sum y_i \cdot (U_\infty - U_i)}{\sum (U_\infty - U_i)} \tag{20}$$

3.6 Mesh Comparison

A mesh sensitivity analysis is conducted by simulating a single bottom-fixed wind turbine under laminar inflow conditions. Coarse ($\Delta x = D/60$), medium ($\Delta x = D/80$) and fine ($\Delta x = D/96$) near turbine grid resolutions are investigated. Note that the mesh is isotropic in all directions. The choice is based on common settings found in the literature [21, 140, 141]. Finer resolutions are not considered due to time constraints.

Table 9: Mesh resolution of the cases investigated in the sensitivity analysis.

Grid resolution	Level 1	Level 2	Level 3	Level 4	Total n° of grid cells
Fine	20 m	10 m	5 m	2.5 m	24.0 million
Medium	24 m	12 m	6 m	3 m	13.6 million
Coarse	32 m	16 m	8 m	4 m	6.0 million

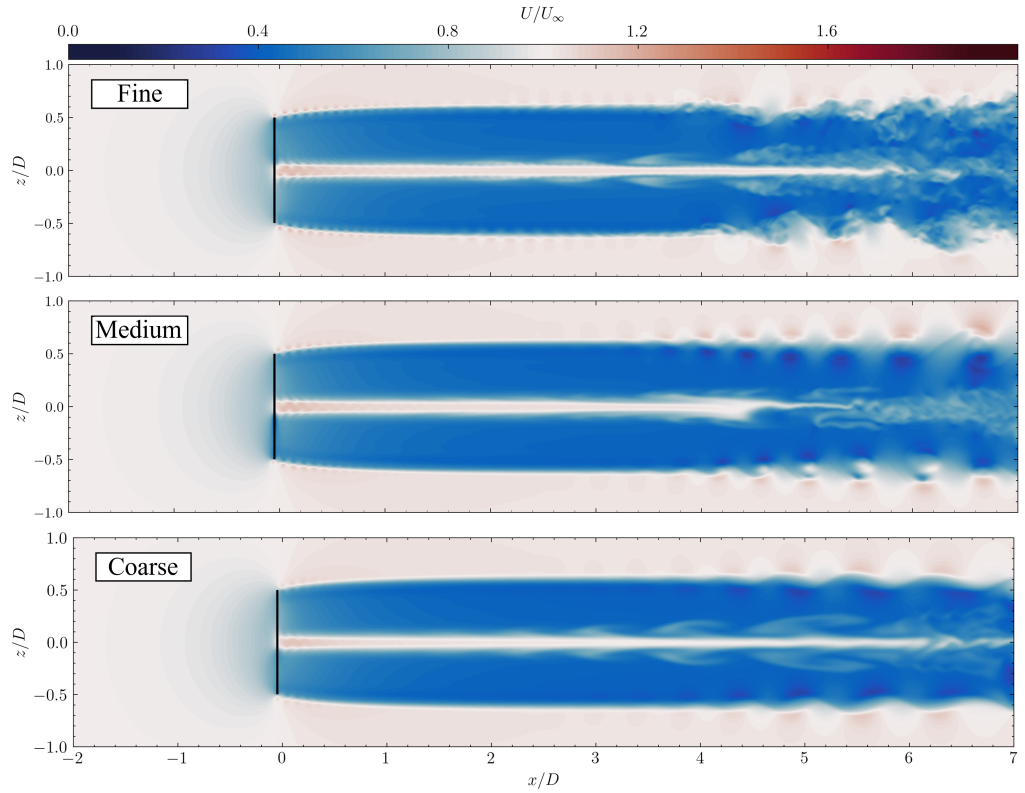

Figure 30: Instantaneous streamwise velocity for different grid sizes.

For all cases, the inflow velocity is set to $U_\infty = 8$ m/s, while the smearing function is kept fixed as a function of the grid, i.e. $\epsilon = 0.8\Delta x$, as suggested by the AMR-Wind documentation. The FLLC is also employed. Note that these settings are used for the remaining comparisons and are not reported again.

As can be seen in Figure 30, the wake at the largest resolution presents substantial discrepancies. In particular, the tip vortices appear significantly smeared out and there is little small-scale turbulence visible. Even the medium mesh refinement does not capture the wake dynamics with sufficient accuracy. Plane averaged velocities support these findings, with the finer mesh resulting in a quicker wake recovery due to the earlier breakdown of the near turbine vortices. These resolution-dependent differences are also present in the predicted power output, where the coarser meshes lead to overpredictions of approximately 3% and 5% compared to the finest mesh. Although full grid independence is not achieved, the finest mesh is consistent with those employed in recent studies [36, 64, 142, 130] and is used for the rest of the simulations.

3.7 Subgrid-scale Model Comparison

Two SGS models are compared to assess their influence on wake predictions. This choice is particularly critical for laminar inflow conditions, where differences between SGS models have been documented [83, 108]. The Smagorinsky model - with two tested constants, $C_s = 0.08$ and $C_s = 0.16$ - and the AMD model are evaluated. The results shown in Figure 31 and 32 confirm the existence of discrepancies. As expected, the transition to a turbulent wake state is sensitive to the choice of Smagorinsky constant, with higher values of C_s delaying the transition to turbulence. The lower C_s value yields closer results to the AMD model, which is in line with the findings by Martinez-Tossaz et al. [108]. The AMD model is also known to be in good agreement with the more complex LASD [143].

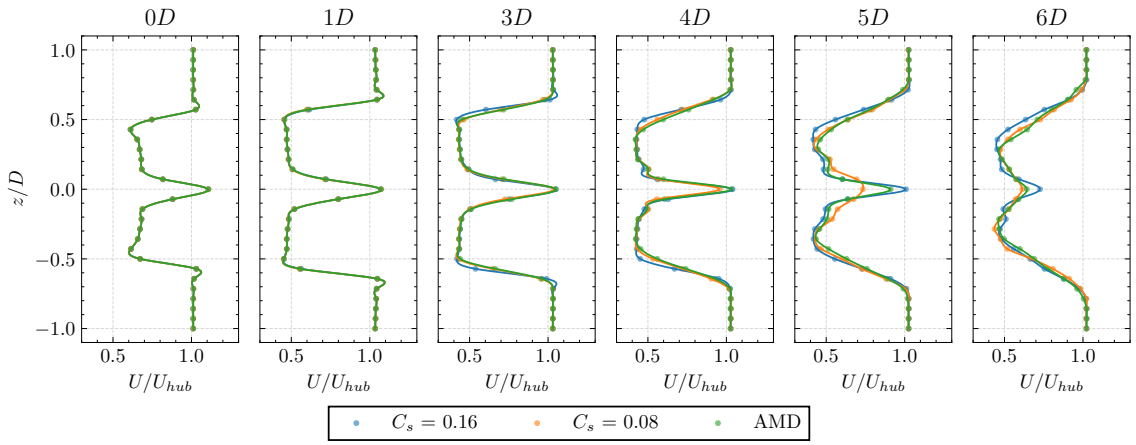

Figure 31: Streamwise averaged velocity along the wake for different SGS models.

For the CNBL cases, prior studies [144, 145] report that the LASD and AMD models can better capture the logarithmic velocity profile and turbulence energy spectra compared to the Smagorinsky model. Again, the AMD model can provide dissipation characteristics comparable to the LASD model. For these reasons, it is decided to adopt the AMD model for both laminar inflow and CNBL cases under investigation.

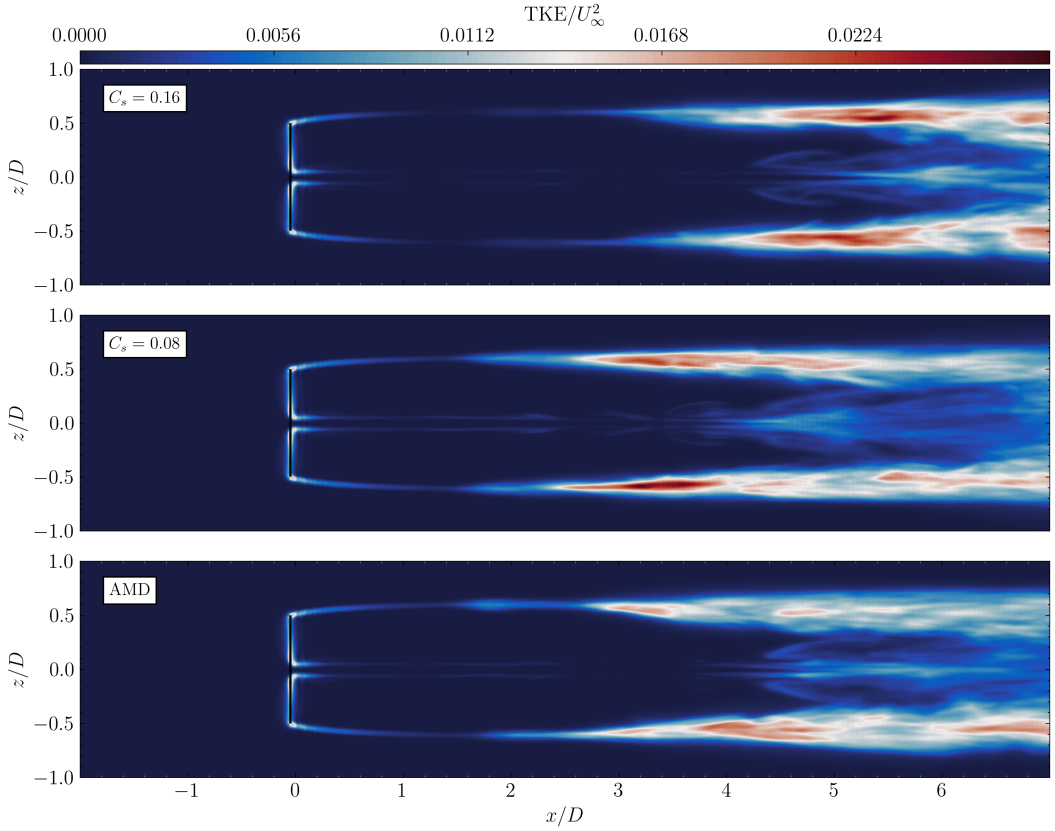

Figure 32: Turbulent kinetic energy field for different SGS models.

3.8 Smearing Radius Calibration

Choosing the right smearing radius (ϵ) for the Gaussian projection function at each actuator location is essential for accurately representing blade loads. Its value affects how relative velocity is sampled, which influences the angle of attack and, consequently, the aerodynamic loads calculated via the lookup tables. In addition, it must be sufficiently large to suppress any numerical instabilities. A wider radius produces thicker, weaker tip vortices that decrease local velocities, especially near the blade tip where chord length varies significantly. This causes overpredictions in torque and power [146]. Therefore, the value of the smearing radius has an impact on wake dynamics, as it affects how long the tip and root vortices remain coherent, with larger values that lead to more diffused vortex

structures [83]. Note that in the current analysis, preliminary tests under uniform inflow conditions show that blade loads are insensitive to subgrid-scale models or numerical settings, consistent with previous findings.

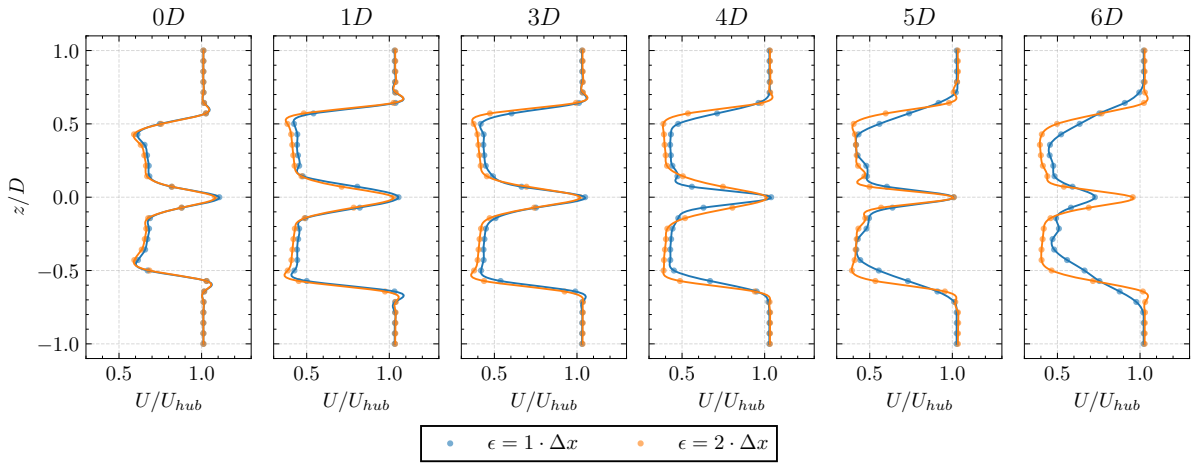

Figure 33: Streamwise averaged velocity along the wake for different smearing radii.

The effects of varying ϵ have been well studied, particularly by Martinez-Tossaz et al. [117], who suggest that its optimal value should be related to the local chord length to ensure accurate results. The literature generally supports using $\epsilon = 2\Delta x$ for stable blade loading, although this recommendation is primarily based on studies involving the NREL 5 MW wind turbine. According to preliminary tests referenced in the AMR-Wind documentation, the optimal value for the IEA 15 MW wind turbine is $\epsilon = 0.8\Delta x$. Recently, Liu et al. [147] conducted a thorough analysis of factors influencing the results of ALM versus BEM. They found that the precision of ALM is primarily influenced by grid spacing, provided that ϵ is optimal, while parameters like the number of actuator points have minimal effect.

Figure 34 illustrates a comparison of various smearing radii within the suggested range from previous studies. It is evident that the ALM gives an overestimation of the axial and tangential loads proportional to the smearing radius. When the smearing radius equals twice the grid size, there is a 10% discrepancy compared to the BEM solution. Below a threshold of $\epsilon = 1\Delta x$, the tangential load shows unrealistic oscillations. The use of FLLC (indicated as ALM-F) corrects the pronounced overshoot observed near the blade tips. This is common in ALM near the blade tips due to "mollification"—the smoothing of shed vortices [148]—as also reported by Trigaux et al. [36]. The discontinuities in blade forces, which are particularly noticeable near the root, are a result of the interpolation process used in the AeroDyn module to generate an arbitrary number of blade points. The lift and drag coefficient tables within AeroDyn are not smooth, leading to abrupt transitions between airfoil sections from one point to the next. This is a known issue within OpenFAST.

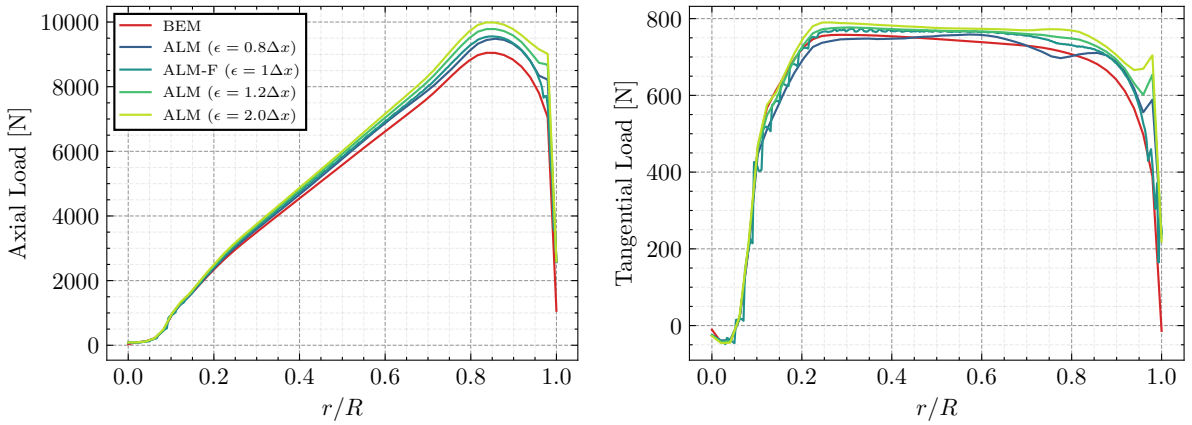

Figure 34: Blade loading for different smearing radius values.

Figure 35 compares the selected smearing radius with results from BEM and the FVW approach implemented in the OLAF module. For this method, the recommendations from the OpenFAST documentation are implemented. The simulation is run for 300 seconds to ensure convergence, with a time step of 0.153 s. Each blade is discretized with 50 nodes. The near-wake is modelled with 1083 panels, including 270 free near-wake panels, while no far-wake panels are used. Vortex core regularization is performed using the Vatistas model.

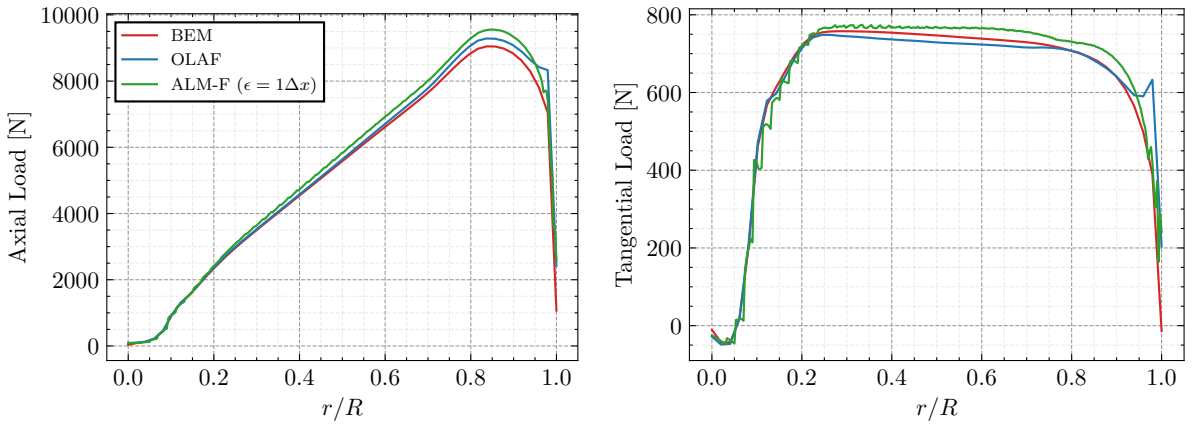

Figure 35: Blade loading for different computational methods.

There is no exact agreement between the different methods, as each relies on its own set of assumptions and limitations. The discrepancies between OLAF and BEM, for instance, come from the regularization of trailing vortex filaments in OLAF, which reduces the induced velocity near the blade tip [36]. BEM assumes each annular ring operates independently and does not account for wake expansion. These simplifications are not present in LES, where such effects are inherently captured. However, ALM applies the

force projection method that is not used in the other cases. In summary, using the current setup, ALM shows approximately a 3% deviation from OLAF and a 5% deviation from BEM in terms of overall thrust and power output. These differences are considered to be within acceptable limits and are consistent with previous studies.

3.9 Validation with Numerical Study

To validate the current simulation framework, a comparison with similar studies is necessary. Unfortunately, ALM-LES investigations of the IEA 15 MW wind turbine are still scarce, making it difficult to establish exhaustive references. In this section, results are compared with those obtained by Parinam et al. [142]. In their study, they employ the YALES2 CFD solver, with a fourth-order spatial and temporal discretization schemes, using an unstructured grid with a near-turbine resolution of $\Delta x = 1.96\,\mathrm{m}$. The inflow is laminar with a freestream velocity of $U_\infty = 9\,\mathrm{m/s}$. The Smagorinsky SGS model is applied with a constant $C_s = 0.16$. The actuator line is discretized using 64 points along each blade, with a smearing radius of $\epsilon = 2\Delta x$. To ensure comparable results, the same SGS model and smearing width are employed. It is worth noting that the velocity profiles in the present simulation are interpolated using the `CubicSpline` function from the Scipy library.

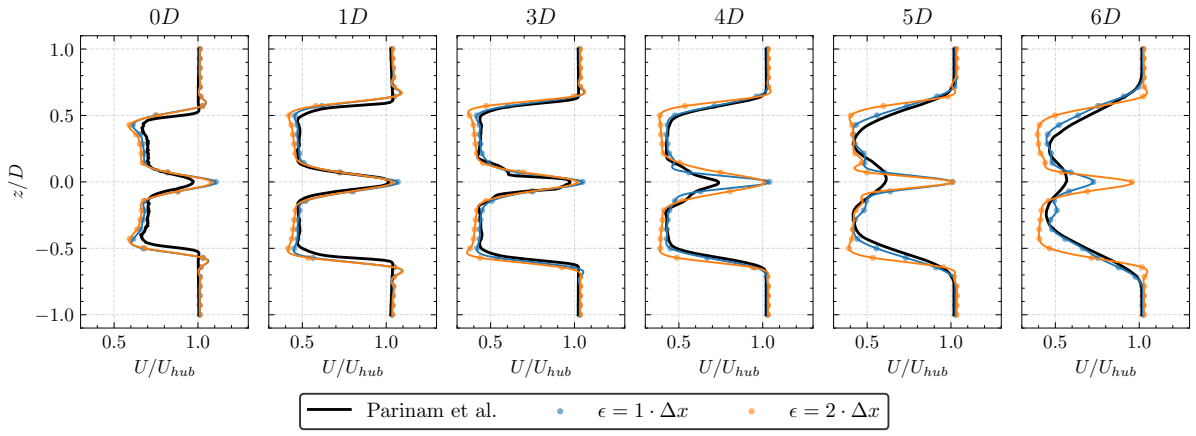

Figure 36: Streamwise averaged velocity along the wake with the results from the reference CFD study.

As shown in Figure 36, some discrepancies can be observed between the time-averaged velocity profiles. In particular, the profile at $0D$ indicates that the blade loading does not fully align with the results from Parinam et al., likely due to the overshoot discussed previously. It is important to note that the $0D$ plane in the present setup is not exactly aligned with the one of the rotor, as there is some overhang (11 m) in the original OpenFAST wind turbine configuration. This offset might explain the higher velocity observed at the center of the wake, where a speed-up occurs. In the results of Parinam et al. the

transition to turbulence also occurs earlier (around $4D$ downstream), due to differences in mesh resolution and hence the smearing radius, both of which significantly influence the underlying physics. The results obtained using the adopted smearing radius of $\epsilon = 1\Delta x$ show better agreement with their wake velocity profiles. Overall, although some variations exist, the current simulation settings are deemed acceptable and consistent with recommended practices for ALM-LES simulations.

3.10 Validation with Experimental Study

Further validation is performed by comparing the wake results with the experimental investigation of Fontanella et al. [62]. This study examined both fixed and moving configurations of a 1:100 scale model of the IEA 15 MW wind turbine, at the wind tunnel of Politecnico di Milano. The experimental conditions are closely reproduced in AMR-Wind, using the finest mesh resolution discussed previously. The CFD setup consists of a similar wind tunnel section, which results in an anisotropic blockage ratio close to the original (see Appendix-C for more details). The Smagorinsky SGS model with coefficient $C_s = 0.16$ is used.

The turbine' blades and tower are represented using actuator points, while the nacelle is modeled as a sphere via an immersed boundary (IB) method. The simulations reproduce "Wind Condition 1", corresponding to a full-scale laminar freestream velocity of $U_\infty = 8.85$ m/s. Ultimately, given the small differences in the results between the fixed and moving cases, only the fixed rotor is simulated. Figure 37 below shows a comparison of the streamwise averaged velocity at $x = 2.3D$.

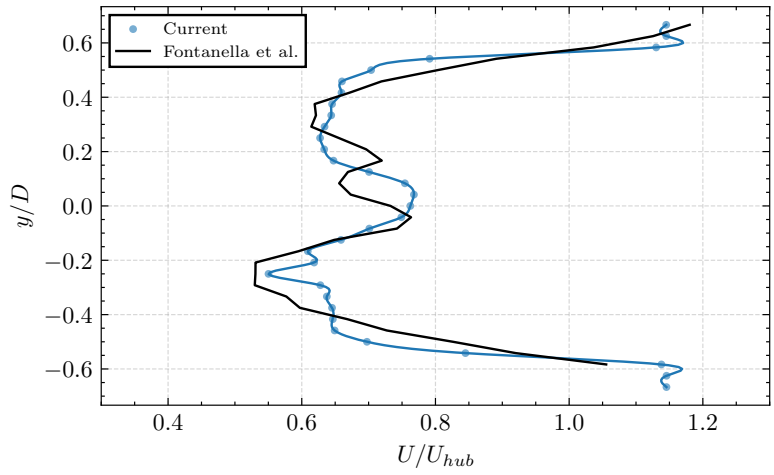

Figure 37: Streamwise averaged velocity at $2.3D$ in the wake with the results from the experimental study.

As can be seen in the results, the velocity profiles match to a good extent. At the extremities, the flow accelerates by about 15% relative to the free-stream velocity, which is in line with the experimental data. The CFD results show less wake contraction, which may be due to the implementation of wall models and to the slightly larger cross-sectional domain. The velocity at center of the wake resembles that of the experimental data. However, the unusual shape is not captured in the CFD simulations, partially due to the limitation in geometry and position of the IB nacelle model.

The observed asymmetry in their data, which resembles a double-Gaussian profile, is suggested by the authors to be due to interaction with the tower. The current simulations do not show this behavior to the same extent, although a larger velocity deficit can be seen in the same region. In addition, a small peak at $y/D = -0.25$ is present, suggesting some probable interaction with the nacelle or tower. Note that the tower support structure cannot be reproduced in the CFD model and might have some impact on the results. The authors also reported potential sources of errors from slight mismatches in the hot-wire probe positions.

Overall, the velocity profiles are comparable, and considering the setup limitations and potential sources of error, the current mesh resolution produces satisfactory results.

3.11 Comparison of Computational Performance

AMR-Wind offers capabilities for conducting simulations on multiple GPUs. This significantly boosts computational performance due to GPUs' superior floating point capability and larger memory bandwidth compared to traditional CPUs [149]. To highlight these differences, simulations are performed on a benchmark single wind turbine case with approximately 24 million cells. Wall clock times are analyzed for CPUs with 32 & 64 cores versus two GPU models, the NVIDIA Tesla A100 and V100. Although performance may differ across systems, this can serve as a useful reference for future simulations.

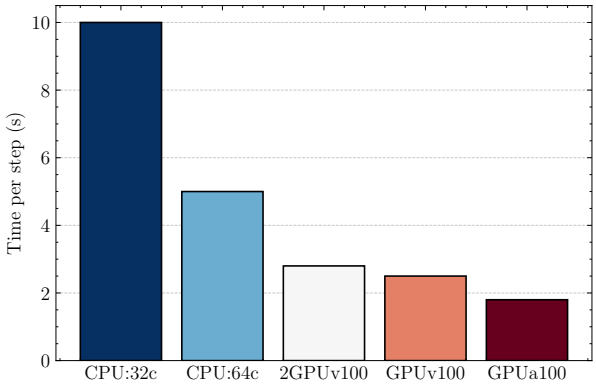

Figure 38: Average wall clock time for different computational setups.

As shown in Figure 38, the CPU performance scales nearly linearly with cores count, i.e. using 64 cores is twice as fast as using 32 cores. In contrast, the Tesla V100 exhibits poor scaling: using two GPUs for this test does not yield any improvement over a single GPU. The A100 outperforms all other setups, achieving a timestep that is a fifth of the 32-core CPU run.

Sharma et al. [91] recommend patch sizes of 16–32 cells per dimension on CPUs and 64–128 cells per dimension on GPUs to maximize computational efficiency. When using multiple GPUs, each GPU should be assigned to a dedicated MPI rank for best performance. A key limitation when using GPUs for large-scale simulations is memory capacity, which can cause job failures. While it would be ideal to leverage multiple GPUs in parallel, practical limitations arise. At the time of this study, only 6 A100 and 12 V100 GPUs are available at the DTU HPC cluster. Additionally, queuing times for multiple GPUs are significantly longer than for a single GPU.

4 Results of Laminar Inflow Cases

This section presents and discusses the results from cases 1–10. The primary focus is on wake interactions and time-averaged statistics, but a power performance analysis for the $5D$ cases is also included. To assess how wake development differs for the FOWTs, the results are consistently compared against those of the reference bottom-fixed case. Both instantaneous and time-averaged velocity fields, as well as turbulent kinetic energy distributions, are examined. Vertical xz-planes are shown to illustrate the wake deflection induced by pitch.

4.1 Floaters Dynamics

To comprehend the differences between platforms and how each FOWT's wake evolves, it is essential to first examine their motion. Figure 39 shows the dynamics of the floaters under calm sea state, focusing on surge and pitch, which are the largest motions and have the greatest impact on wake dynamics. Note that all 6-DOF are active during the simulations, nonetheless.

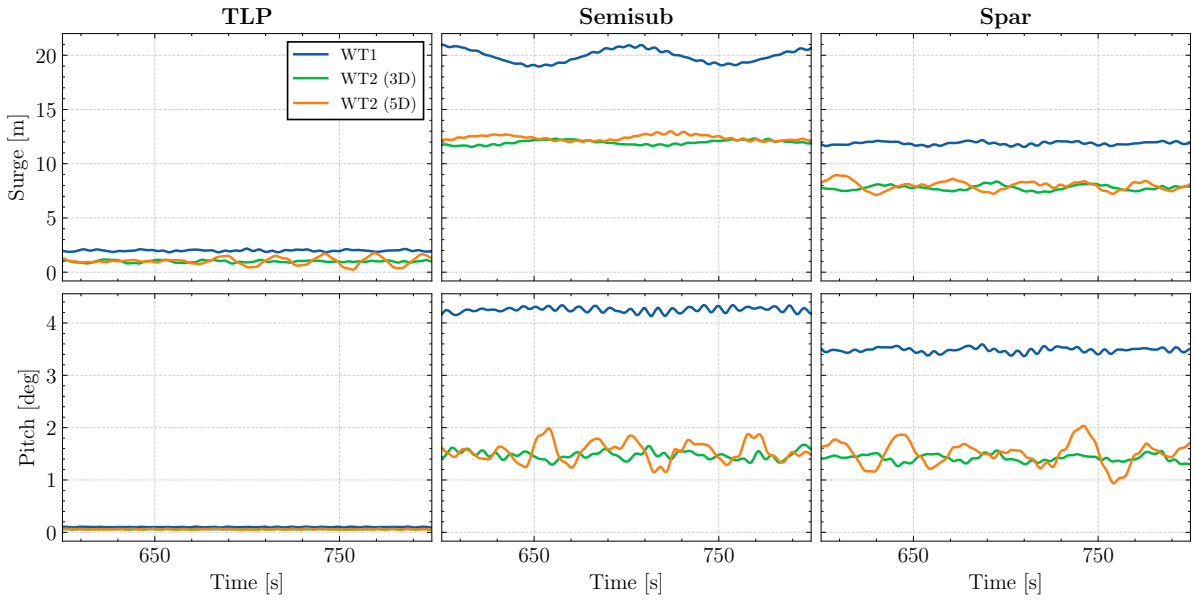

Figure 39: Dynamic response of the floating wind turbines under laminar inflow and calm waters ($\overline{U}_{hub} = 10.59$ m/s, $H_s = 1.0$ m, $T_p = 7.5$ s).

In the current results, the semisub exhibits the largest mean motions in both average surge and pitch. For the first wind turbine, the semisub undergoes a slow but large oscillatory surge ($f_S \approx 0.01$). The spar experiences higher-frequency ($f_S \approx 0.04$) and

low amplitude motion, similar to that of the TLP. The second-row turbines display smaller mean motions, as they exert reduced thrust.

The $3D$ and $5D$-spaced cases show comparable average motions; however, the $5D$ cases presents significantly greater unsteadiness across all platforms. This is particularly evident in the pitch motion of the semisub and spar, as well as in the surge motion of the TLP. The increased displacement may be attributed to the higher turbulence intensity that the far rotors perceive. This is absent in the more closely spaced $3D$ turbine configuration, as the wake does not have enough space to transition to turbulent state before reaching the second wind turbine.

Figure 40 illustrates the floaters' motion under extreme sea state conditions. In this scenario, the second-row turbines exhibit similar dynamics to those upstream, as they generate closer average thrust levels. Both platforms face high-frequency oscillations in surge and pitch, as the large waves dominate the floaters dynamics responses. The surge standard deviation remain comparable between TLP and spar, while pitch is significantly larger for the spar, both in terms of average displacement and amplitude. A notable difference from calm sea conditions is that surge and pitch motions appear strongly correlated. It is also worth noting that heave motion becomes moderate for the spar in such sea conditions.

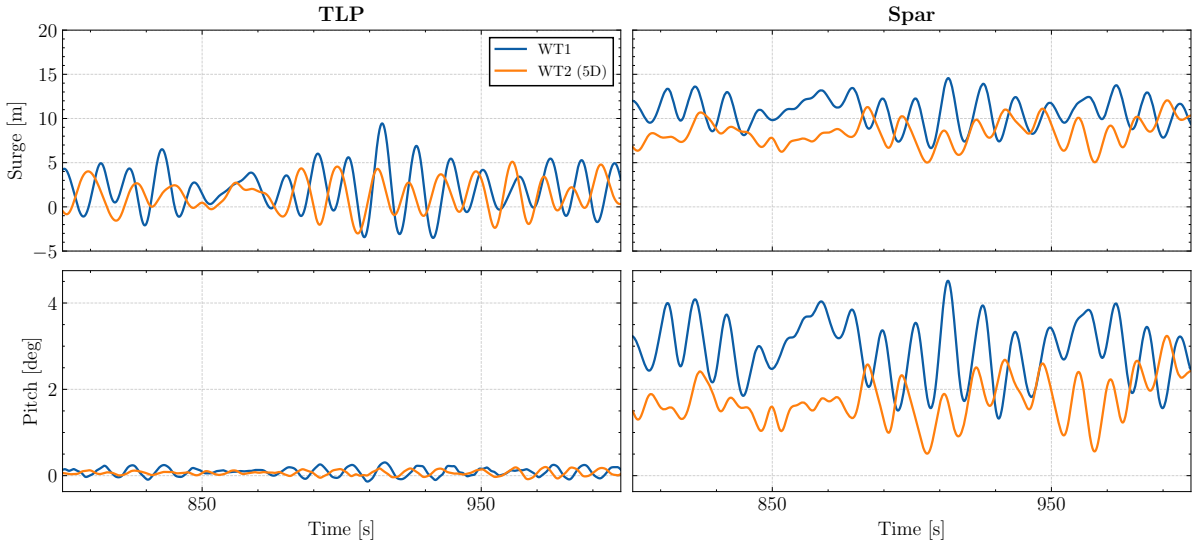

Figure 40: Dynamic response of the floating wind turbines under laminar inflow and rough waters ($\overline{U}_{hub} = 10.59$ m/s, $H_s = 10$ m, $T_p = 12$ s).

4.2 3D Spacing

4.2.1 Flow Field Analysis

A comparison between the instantaneous velocity fields for the different floaters is illustrated in Figure 41. All the floating platforms influence the wake evolution of the freestream wind turbine, although the changes are minimal given the small amplitude of motion. The oscillatory movement of the platforms triggers the formation of vortex instabilities, which are particularly visible at the tip of the blades. Moreover, it affects the distance between individual tip vortices, increasing their interaction. The starting location and width of the velocity fluctuations appears to be dependent on the amplitude of motions, with the TLP starting at around $1.5D$ in the wake, while the semisub and spar close to $1D$ downstream.

The root spiral structures remain mostly unaffected for the TLP, but start breaking down earlier for the other platforms. In particular, the initial mixing process occurs before reaching the downstream wind turbine, while for the fixed case, the free flow travels up to $1D$ beyond the second wind turbine. A major contribution to the increased mixing at the center is the mean pitch induced by the platform's motion, which causes vertical deflection of the wake for both semisub and spar platforms.

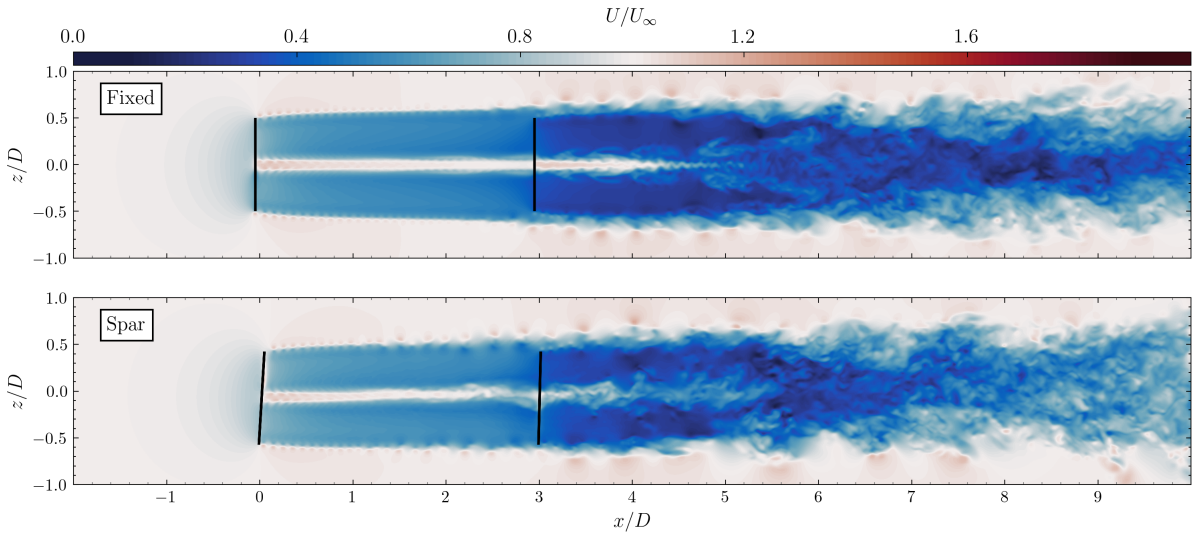

Figure 41: Instantaneous streamwise velocity for the $3D$ laminar inflow configurations under calm sea state (Cases 1 and 3).

The averaged streamwise velocities at key locations along the wake are shown in Figure 42. The change in thrust between the wind turbines is evident at $1D$, where it influences the velocity deficit behind the turbine. All three floating platforms exhibit similar velocity profiles, with slightly higher mean velocities compared to the bottom-fixed case.

The previously mentioned wake veering can be observed both near the first turbine and in the far wake. At $9D$, all FOWTs display significantly greater wake recovery than the bottom-fixed case, with the spar showing up to twice the velocity at the rotor center.

The velocity distribution approaches a Gaussian profile for all configurations at around $6D$. At this position in the wake, no significant differences in the mean velocity between platforms can be observed, although the spar and semisub are subject to higher levels of flow entrainment. The difference in the motion frequency, particularly for surge, appears to have a significant effect on flow mixing. Higher-frequency surge, such as in the TLP and spar, promotes the breakdown of vortex structures, as also reported by Li et al. [150]. In contrast, the semisub's large but slower displacements do not contribute to the same extent.

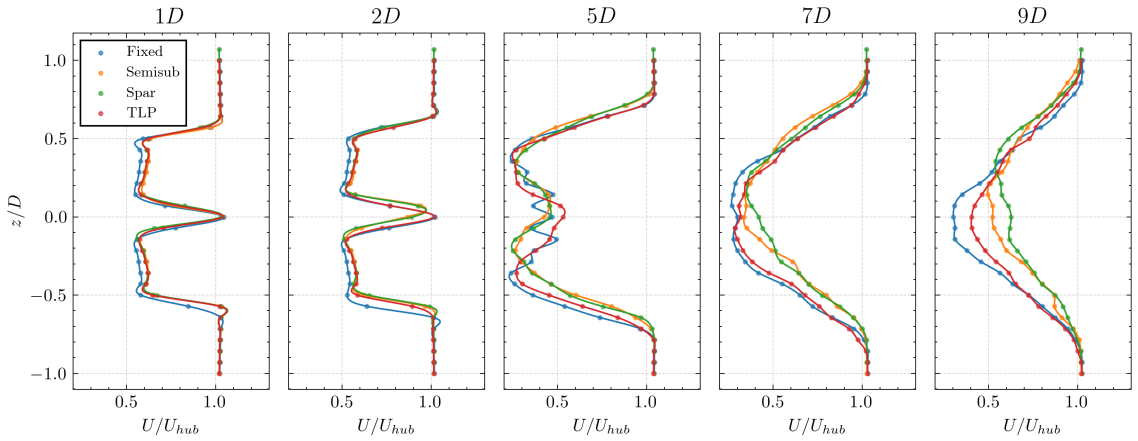

Figure 42: Streamwise averaged velocity along the wake for the $3D$ laminar inflow configurations under calm sea state (Cases 1-4).

Figure 43 presents the distribution of TKE in the wake region. All FOWTs show an increased TKE production compared to the fixed structure. This can be associated with the expansion of the turbulent shear layers caused by the rotor's motion, which enhances energy entrainment. Among the platforms, the spar exhibits the highest TKE levels, particularly near the lower part of the rotor. The semisub also shows elevated TKE in that region, though to a lesser extent. In both cases, the increase can be attributed to the vertical wake deflection. The TLP demonstrates a more balanced TKE distribution, consistent with its relatively symmetric motion profile.

The results suggest that high-frequency surge leads to larger TKE production. This is because smaller and faster motions tend to produce more chaotic and unpredictable flow structures, as also observed by Li [57]. The semisub's lower-frequency surge contributes to a more stable and coherent flow field. In fact, the TKE peaks of the semisub are similar to those of the fixed platform, with the primary distinctions arising from the wake deflection due to pitching.

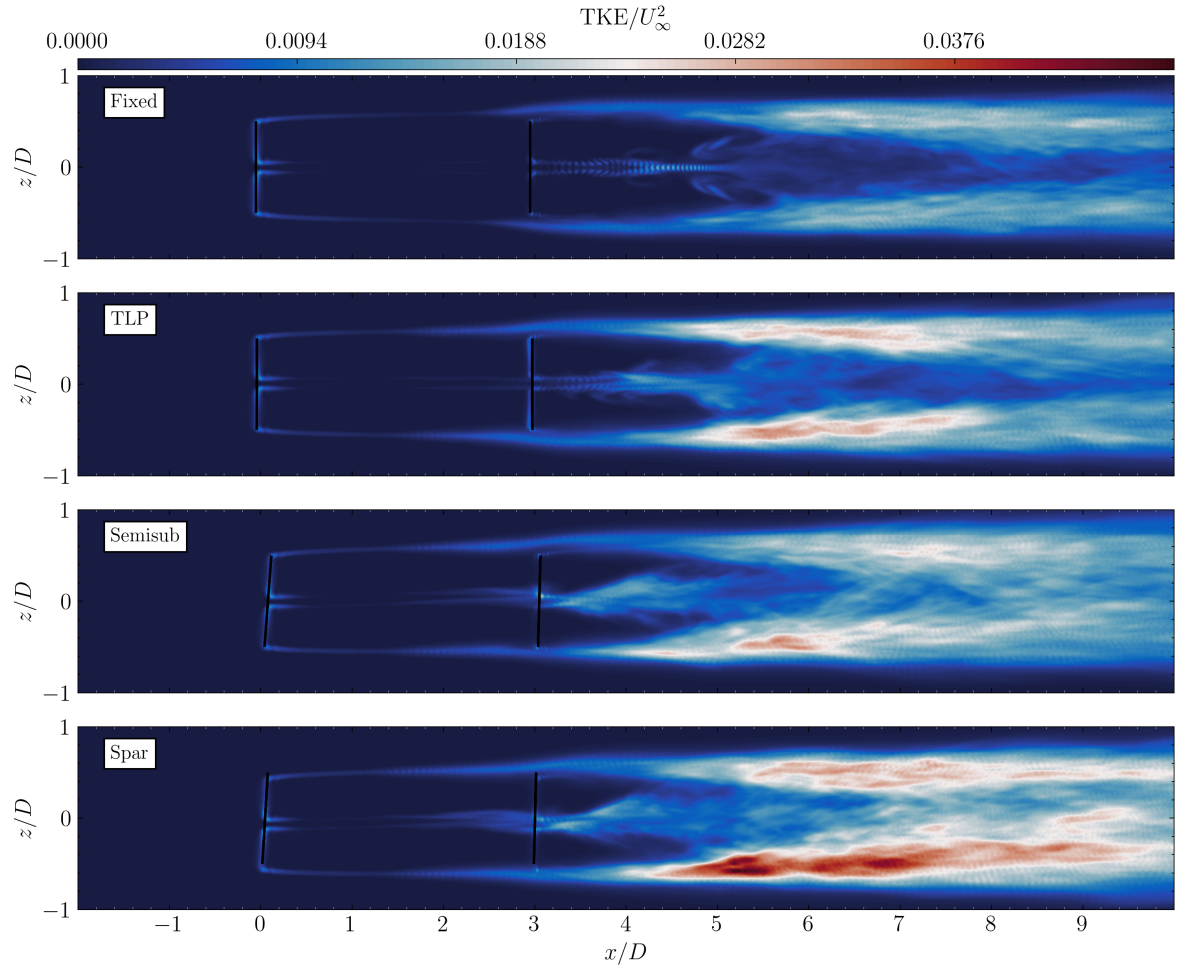

Figure 43: Turbulent kinetic energy for the $3D$ laminar inflow configurations under calm sea state (Cases 1-4).

4.3 5D Spacing

4.3.1 Flow Field Analysis

This section presents the wake analysis for the $5D$-spaced configurations. The evolution of the upstream wind turbine flow structures remains nearly identical to the results discussed previously, but now, the wake has more room to develop before reaching the second turbine. One notable consequence is the full breaking down of root vortices for the semisub and spar platforms, with the velocity profiles adopting a Gaussian-like shape just before entering the second turbine. All the floaters generate increased unsteadiness and a pronounced asymmetry in the far wake region. In particular, the lower half of the far wake shows significantly higher average velocities compared to the fixed case.

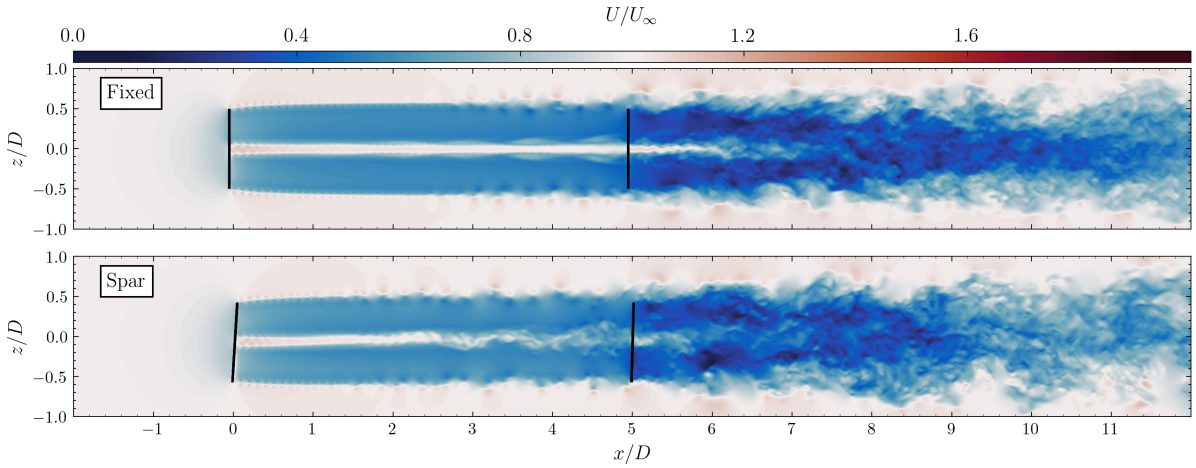

Figure 44: Instantaneous streamwise velocity for the $5D$ laminar inflow configurations under calm sea state (Cases 5 and 7).

Figure 45 shows that the semisub produces the most pronounced vertical shift in the wake, with its velocity profile resembling a Gumbel-like shape. Interestingly, the semisub's largest velocity deficits beyond $10D$ align closely with the bottom-fixed case. This further reinforces the hypothesis that slower oscillations do not substantially enhance wake recovery. Overall, the differences between floaters in the far wake have largely decreased compared to the $3D$-spacing configurations.

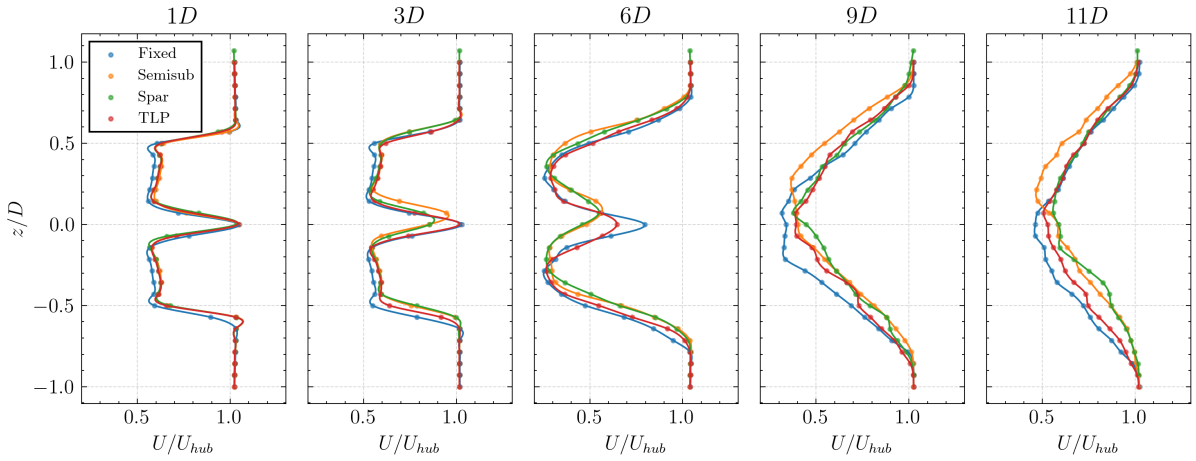

Figure 45: Streamwise averaged velocity along the wake for the $5D$ laminar inflow configurations under calm sea state (Cases 5-8).

The TKE profiles of the $5D$-spaced FOWTs resemble those of the closer configurations. The areas of high production remain unchanged, with the primary difference being a generally lower TKE budget around the same regions due to the increased distance between turbines.

Figure 46 illustrates the wake dynamics under extreme sea state conditions for the spar platform. Significant velocity fluctuations are visible behind the freestream rotor, which grow further beyond the second wind turbine. Similar findings are observed for the TLP, altough these effects are less pronounced. This suggests that the oscillations are mainly driven by surge, but pitch and heave motions have the potential to amplify them, especially in extreme sea states.

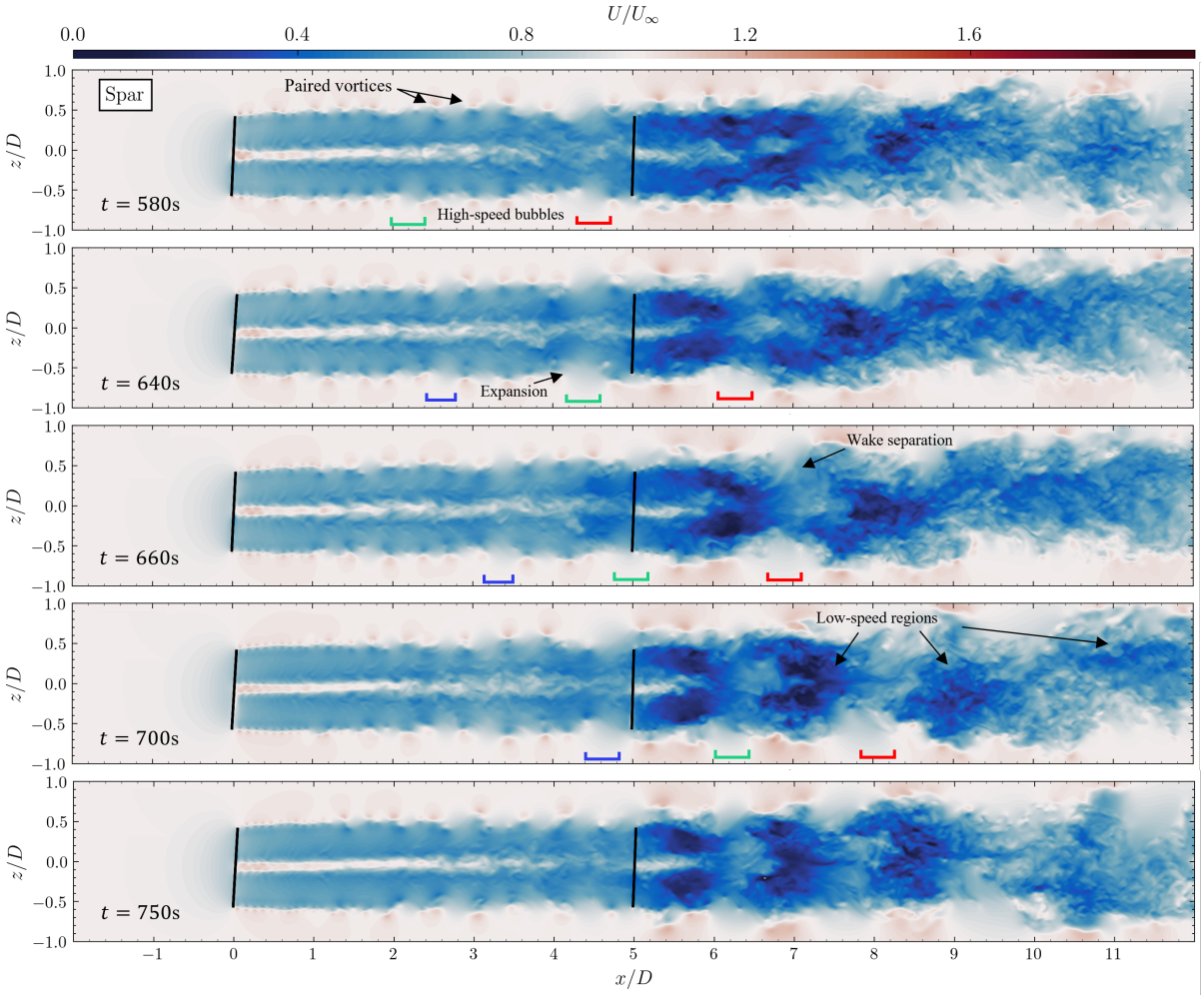

Figure 46: Time evolution of the streamwise velocity for the $5D$ laminar inflow configurations under extreme sea state (Case 10).

In order to interpret these findings, it is useful to recall the operational stages of a dynamic rotor. During the downward motion of a FOWT, the system enters a vortex-ring state, where the distance between tip vortices contracts and leads to their pairing quicker than for a steady rotor. This causes the formation of coherent, three-dimensional vortical structures with accelerated flow near the tips and smaller flow velocity inboard. As the FOWT reverses and moves upward, it transitions into a propeller state, accelerating the inflow and generating high-speed bubbles (HSBs), shown with brackets in Figure 46. The formation of these structures is directly linked to the FOWT's motion and its variation in thrust. Several authors [57, 151, 152] have shown that the evolution of the HSBs is strongly dependent on both the frequency and amplitude of rotor displacements. The current results confirm that these phenomena can occur under realistic, 6-DOF complex motions.

As the vortex rings travel downstream, they interact with the second wind turbine. Depending on the surging and pitching phase of the latter, the incoming vortices can merge, forming regions of significantly reduced velocity. These are especially pronounced when the second FOWT moves in phase with the motion-induced wake signature of the upstream turbine, resulting in a superposition of wake structures. By the time the HSBs reach the downstream rotor, they have expanded in size due to the rise in pressure in front of the FOWT and to obey the conservation of mass. If the HSBs are sufficiently large, they can induce separation in the wake of the second turbine, producing pulses of low-speed flow. This, in turn, generates alternating pressure regions within the second turbine's wake that persist for distances of at least up to $11D$ (see Figure 47).

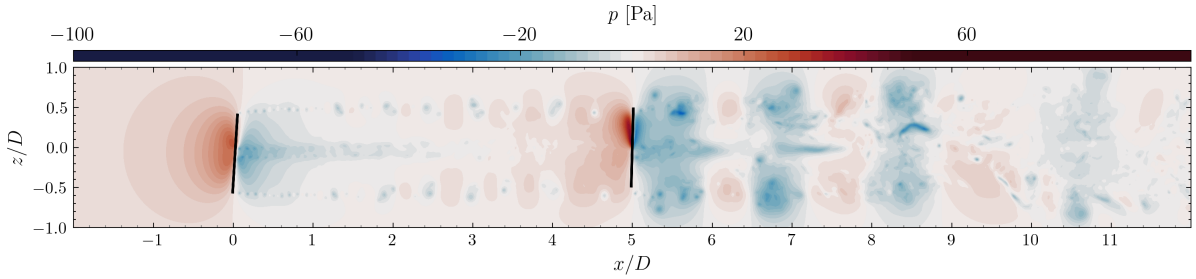

Figure 47: Instantaneous gauge pressure for the $5D$ laminar inflow configurations under extreme sea state (Case 10).

The author identifies this phenomenon as *Phase-Induced Wake Separation* (PIWS). This can have important implications for floating wind farm design and operation. Specifically, the PIWS would likely results in large loads and stress on downstream FOWTs during rough sea states. In addition, the velocity fluctuations in the wake appear to amplify the motion of the second-row FOWTs. This is supported by the comparison of the turbines' coefficient of variation for surge and pitch, which shows a larger magnitude for the downstream FOWT. To mitigate these effects, strategies such as wake steering, adaptive control of rotor speed, or other control mechanisms may be required.

Overall, the current observations are consistent with the findings by Kleine et al. [151]. In this study, the authors concluded that the number of interacting vortices is related to the non-dimensional parameter ω^*, defined as the ratio between the motion frequency and the rotational frequency of the turbine. In particular, they observed that lower values of ω^* lead to larger flow structures inside the wake, due to an increased number of vortex interactions. In the current analysis of the extreme sea conditions, these values varies between $\omega^* = 0.53 - 0.73$, resembling the results that they obtained under prescribed surge motions at $\omega^* = 0.5$ (see Figure 9e in their report). Similar evidence can also be found in the work by Lee et al. [54], where a combination of harmonic motions with similar values of ω^* was prescribed.

The signature of the floating motion is visible in the spectral content of the streamwise velocity in the wake, as shown in Figure 48. To enhance the distinction, the average across all vertical probes is used. A distinct peak appears around $f = 0.018$ (marked with a dashed line), which also occurs in the surge motion signal of both wind turbines (see Appendix-A). At a downstream distance of $4D$, the same frequency component and its harmonics are present, but with lower energy content. Further downstream, at $11D$, the peak is still distinguishable, although the frequency has slightly shifted due to the increase in flow velocity.

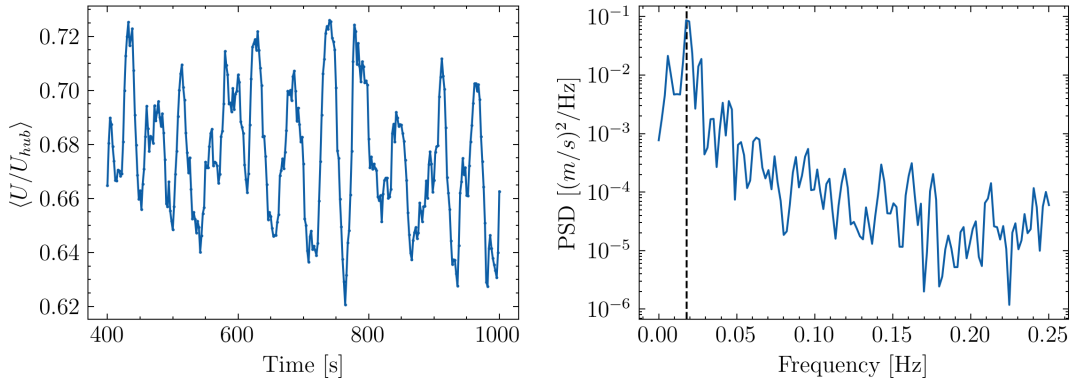

Figure 48: Characterization of the averaged velocity at $x/D = 6$ along the wake for the $5D$ laminar inflow configuration under extreme sea state (Case 10).

In rough sea conditions, the large amplitude and high frequency motions of the freestream FOWTs result in increased flow entertainment behind the first rotor when compared to calm waters. As the flow moves beyond the second turbine, the velocity profile realigns with those observed under calm sea state. This suggests that wake recovery does not improve beyond the second turbines row, likely due to the presence of large separated flow regions described earlier, which may inhibit the recovery process.

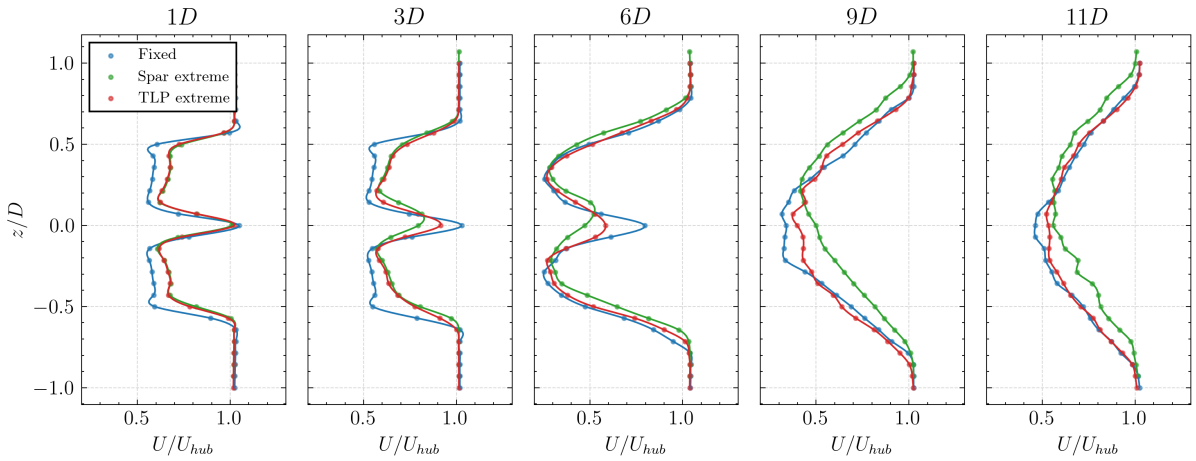

Figure 49: Streamwise averaged velocity along the wake for the $5D$ laminar inflow configurations under extreme sea state (Cases 1, 9, 10).

4.3.2 Turbines Performance

The power performance of the wind turbines under laminar inflow is presented in Figure 50. The first row of FOWTs shows reduced power generation, with the spar performing the worst. Among the second row, the semisub generates more electricity. Overall, the total power output from FOWTs during calm waters remains nearly identical to the bottom-fixed case, with differences within 1%. Under extreme sea conditions, instead, the TLP and spar show a 2.7% and 2.0% increase respectively relative to the fixed case.

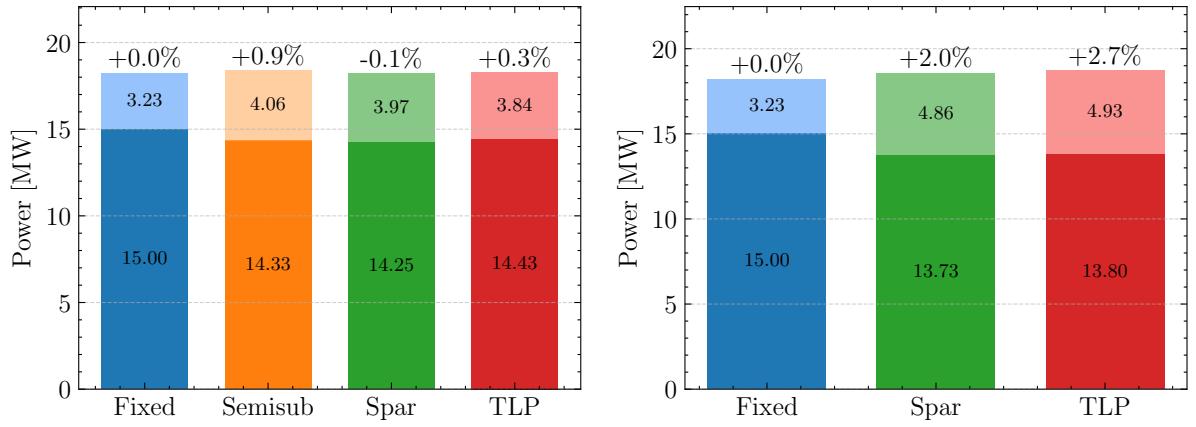

(a) Calm sea state.

(b) Extreme sea state.

Figure 50: Power performance of the wind turbines for the $5D$ laminar inflow configurations. Dark colors represent first row, while light colors represent second row.

The decrease in power in the upstream FOWTs is primarily due to the average positive rotor pitch, while dynamic rotor motions should generally improve power generation [12]. Since the wind turbines in the current scenarios operate at rated wind speed, they do not benefit from the higher relative velocities induced by platform motions, as the power is capped at the rated level. For the same reason, the actual losses due to the positive pitching might be small. However, as the turbines transition between regions 2 and 3, power gains or losses above rated depend significantly on the pitch controller's behavior. The fact that the U-Maine semisub controller is used for all FOWTs is likely to cause worse performance on the spar and TLP.

The downstream turbines, on the other hand, operate at lower wind speeds and can benefit from dynamic rotor motion effects. They also face higher inflow velocity compared to bottom-fixed due to improved wake recovery upstream.

4.4 Summary

In this section, wake interactions between different FOWTs were examined under laminar inflow conditions. During calm sea state simulations, the FOWTs experienced minimal motion, mainly characterized by slow surge and steady pitch movements. Among the platforms, the semisub and spar showed the most noticeable influence on the wake compared to the bottom-fixed configuration, resulting in a significant vertical shift in the near wake. The spar and TLP generated larger TKE levels, driven by their higher-frequency motions. Turbulence intensity was consistently higher in the near wake of the FOWTs but gradually decreased, becoming comparable to the fixed case at approximately $6D$ behind the second rotor.

Wake recovery was generally improved by the rotor motions, both in the near and far wake, supporting previous literature findings [10]. This was strongly influenced by turbines spacing. For the $3D$ cases, a clear improvement in far-wake velocity profiles was observed, whereas this benefit became less pronounced for the $5D$ cases. Across both configurations, the spar produced the highest far-wake wind speeds. The results highlighted that slower platform motions, as experienced by the semisub, do not yield as much improvement in wake recovery as the other floaters.

During extreme sea state simulations, both the TLP and spar exhibited large surge motions, although the TLP remained very stiff in the pitch degree of freedom. The reduction in thrust due to motion led to a notable increase in flow velocity in the near wake for both floaters. However, this did not result in higher recovery in the far wake beyond the second turbine, where the velocity levels remained below those observed under calm sea conditions (see Figure 51). Turbulence intensity increased significantly along the wake of both wind turbines, before reaching similar levels to the other cases by $11D$ downstream.

Distinct changes in the flow structures were observed in rough sea conditions. The dynamics of the FOWTs led to faster vortex pairing and substantial thrust fluctuations, contributing to a highly unsteady wake behind the first turbine. This unsteadiness manifested as big, periodic HSBs forming downstream. As these bubbles passed through the second turbine, their interaction with the turbine's own vortices generated low-speed regions. Large alternating regions of pressure differences were produced by both the spar and TLP, though less pronounced for the latter. This phenomenon was closely linked to the phase alignment between the motion of the downstream FOWT and the incoming wake. The results suggested that this phenomenon is mostly surge-driven, but that pitch and heave motions can accentuate it. Lastly, the trace left on the wake by the upstream FOWT seemed to promote the downstream FOWT motion.

The power performance of the FOWTs during calm waters remained within 1% of that of the fixed case. For the extreme sea state, the floaters showed an increase of up to 2.7% in electricity production.

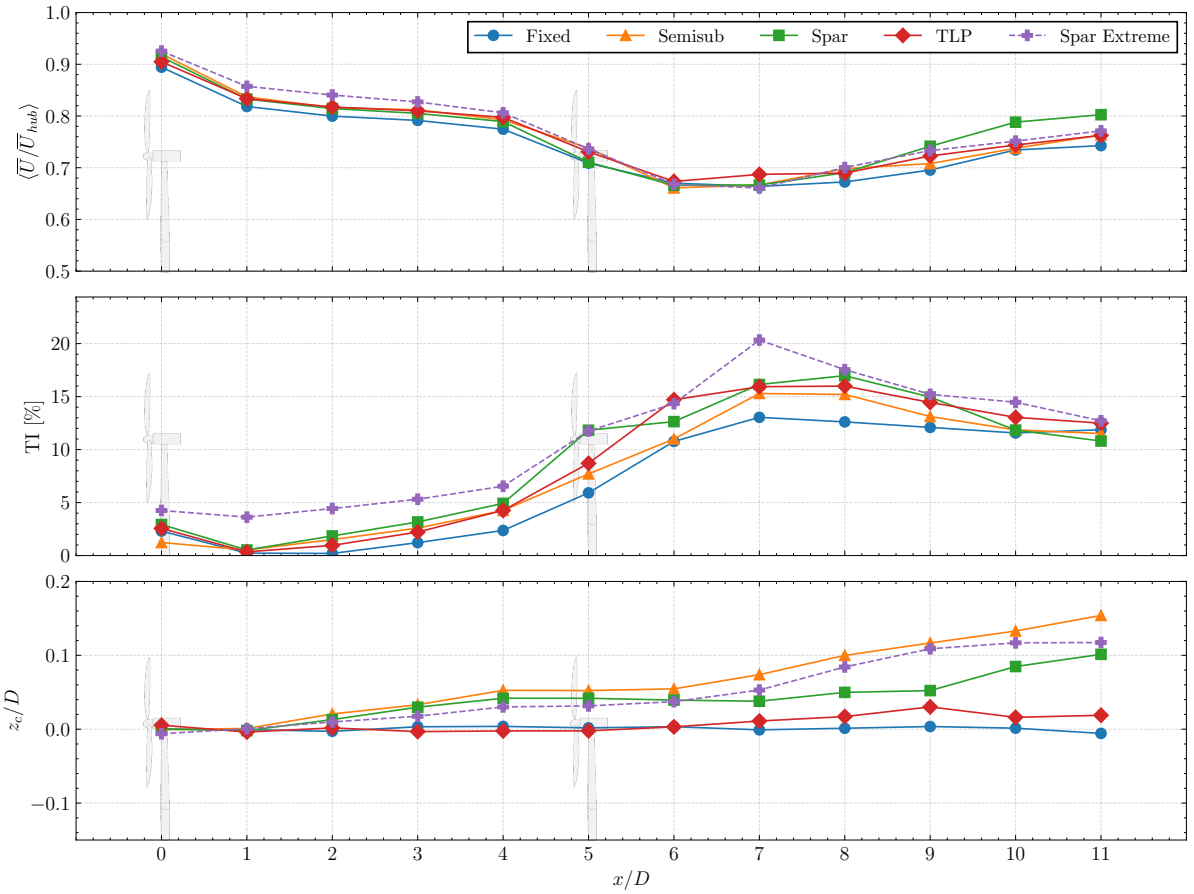

Figure 51: Comparison of the averaged streamwise velocity (top), turbulence intensity (middle) and vertical wake center (bottom) for different wind turbine configurations under laminar inflow conditions ($\overline{U}_{hub} = 10.59$ m/s).

5 Results of Neutral ABL Cases

This section presents and discusses the results from Cases 11–20. The instantaneous and time-averaged velocity fields, together with the turbulent kinetic energy distributions, are examined. An analysis of the power performance is conducted for both $3D$ and $5D$ configurations. The xz-planes and xy-planes are illustrated to understand the wake evolution of the wind turbines.

5.1 Floaters Dynamics

The dynamics of the FOWTs under neutral ABL conditions are shown in Figure 52. Both TLPs undergo displacements close to those observed under laminar inflow. The upstream semisub shows a similar response, while the downstream one experiences significantly larger surge and pitch amplitudes. The spar platforms also face more pronounced surge and pitch motions than during laminar inflow. This suggests that the motion of FOWTs gets amplified when encountering larger turbulence levels, such as those in the wake of upstream wind turbines. This observation aligns with findings by Jacobsen et al. [153] based on full-scale measurements from the Hywind Scotland wind farm.

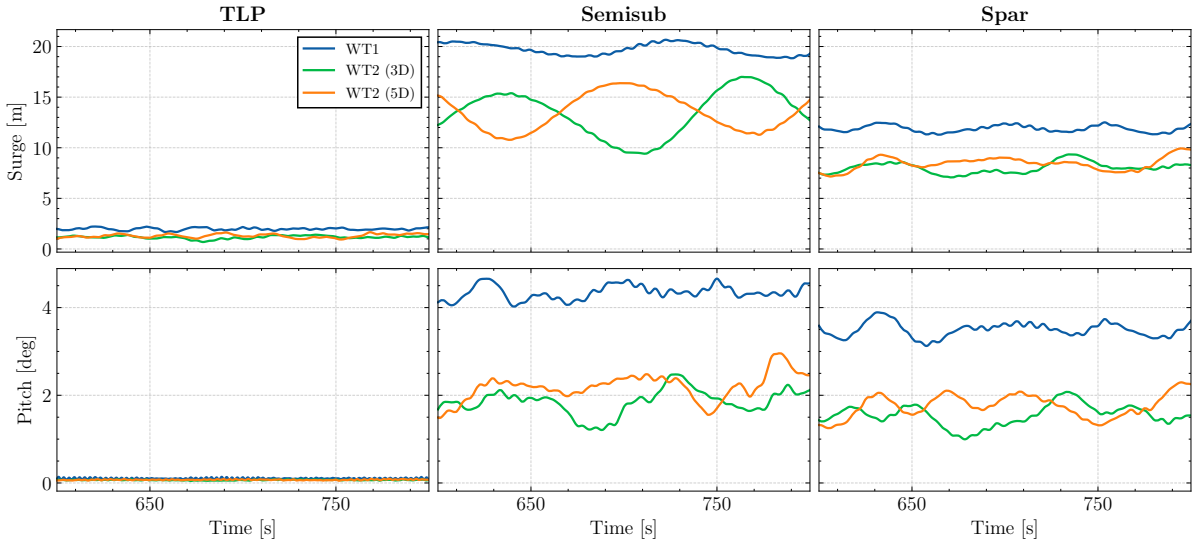

Figure 52: Dynamic response of the floating wind turbines under neutral ABL and calm waters ($\overline{U}_{hub} = 10.59$ m/s, TI $= 5\%$, $H_s = 1.0$ m, $T_p = 7.5$ s).

Figure 53 illustrates the motion of the floaters under extreme sea state conditions. Surge and pitch for the TLP behave almost identically to the laminar cases, with small additional unsteadiness over time. The freestream spar shows similar surge motion, but generally higher averaged pitch. The second-row spar experiences an increase in both

degrees of freedom, up to 3 meters in surge and 1 degree in pitch. This is expected, as the shear inflow generates a non-uniform thrust distribution on the rotor, with larger amplitudes in the upper half of the turbine.

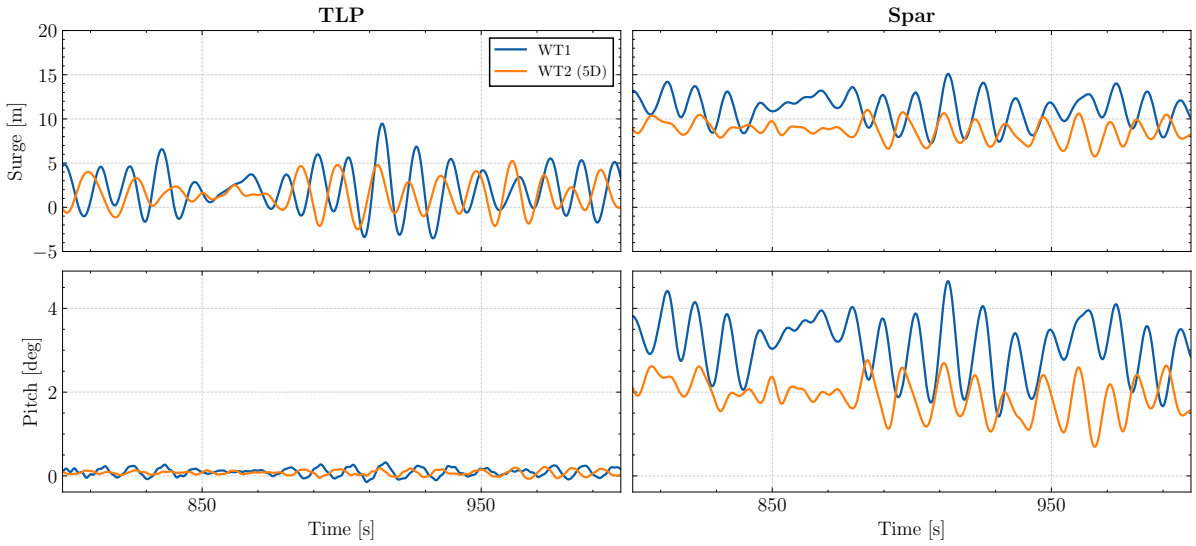

Figure 53: Dynamic response of the floating wind turbines under neutral ABL and rough waters ($\overline{U}_{hub} = 10.59$ m/s, TI= 5%, $H_s = 10$ m, $T_p = 12$ s).

5.2 Precursor

The ABL simulations load stored data from a precursor step, which ensures that the incoming flow remains identical across all cases under investigation. This dataset consisted of 1000s of saved flow information. For completeness, a snapshot of the velocity fields from the precursor simulation without wind turbines is shown in Figure 54.

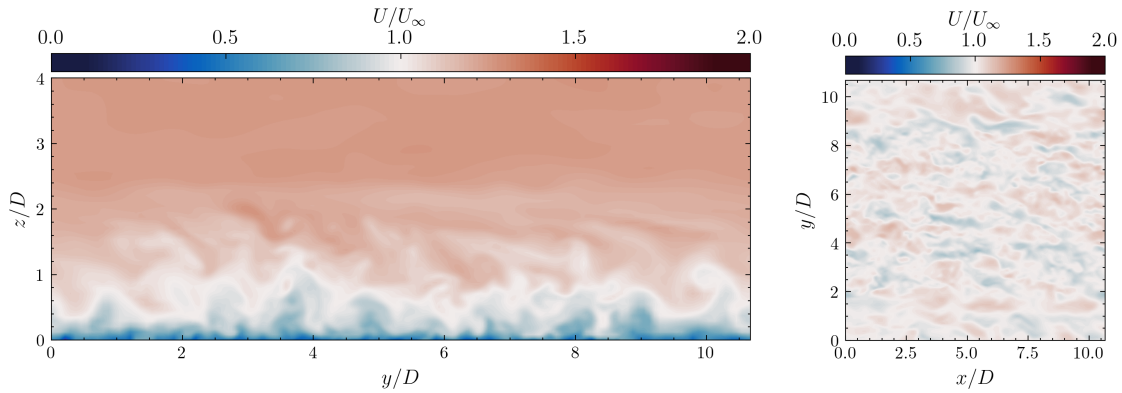

Figure 54: Streamwise velocity from the precursor simulation along the frontal plane (left) and at hub height, $z_{\text{hub}} = 150$ m (right).

5.3 3D Spacing

5.3.1 Flow Field Analysis

Figure 55 shows the instantaneous field velocity of the fixed and semisub configurations. As can be observed, the flow is highly complex and heterogeneous, resulting in small differences between cases. The velocity field within a neutral ABL is distinguished by turbulence structures that can reach sizes comparable to the turbine diameter. For this reason, the wake development is affected, if not dominated, by these mechanically generated eddies.

For the upstream wind turbine, tip vortices persist for longer than the bottom vortices, which break down more rapidly. This phenomenon is well known and has been subject to extensive investigations (see for example [142, 151, 154]). In the FOWT configurations, top-tip vortices extend up to 1.5 rotor diameters, whereas in the bottom-fixed case, they dissipate by approximately $1D$. Additionally, the freestream flow at the rotor center spans for a longer distance for the moving rotors. The vertical wake shift due to pitch is minimal and barely visible.

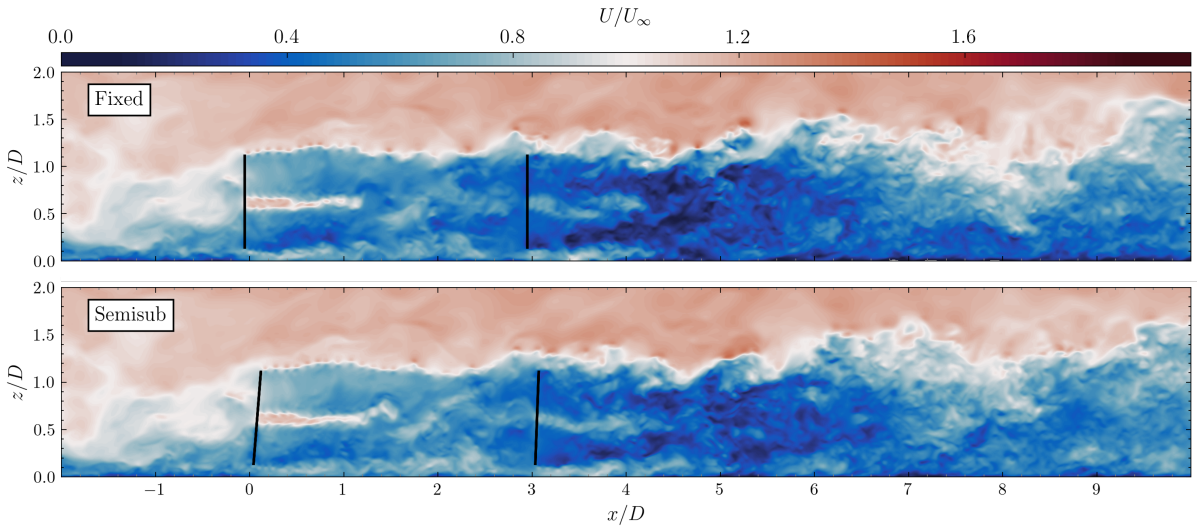

Figure 55: Instantaneous streamwise velocity for the $5D$ neutral ABL configurations under calm sea state (Cases 11 and 14).

In the near wake, the turbine's motion facilitates the breakdown of existing eddies in the flow. This, along with the lower FOWT's thrust and increased fluctuations, leads to improved wake recovery behind the freestream rotor. This is supported by showing the difference in averaged velocity between floating and fixed configurations (Figure 56). Here, the momentum deficit is notably lower behind the first FOWT, confirming the general literature findings [10]. However, as the flow progresses beyond the second

FOWT, it is gradually replenished from the upper-tip region. At approximately $6D$ downstream, the average rotor velocity for the fixed case becomes marginally higher, indicating increased flow entrainment with growing distance. Li [57] performed ALM-LES simulations of two surging wind turbines and also observed that under similar turbulence levels (5%), fixed turbines achieve equal or greater wake recovery beyond $3D$ downstream of the second turbine.

The fact that this trend is also seen in the TLP suggests that pitching is not fully responsible for the differences in the flow per se, but may still play a contributing role in combination with platform dynamics. The vertical displacement induced by a constant pitch appears to redistribute the flow momentum by stretching the positive-negative ΔU pattern diagonally. This effect is particularly visible in the semi-sub, as it experiences larger pitch amplitudes. Further investigations are required to conclude whether a tilted rotor has a net positive influence on wake recovery, particularly when coupled with platform motions. Some experimental studies [60, 155] report that upward rotor tilt tends to slow down recovery, due to a shift in turbulent kinetic flux. In contrast, Su et al. [156] argue that tilting the rotor promotes faster breakdown by increasing interaction with the surrounding flow.

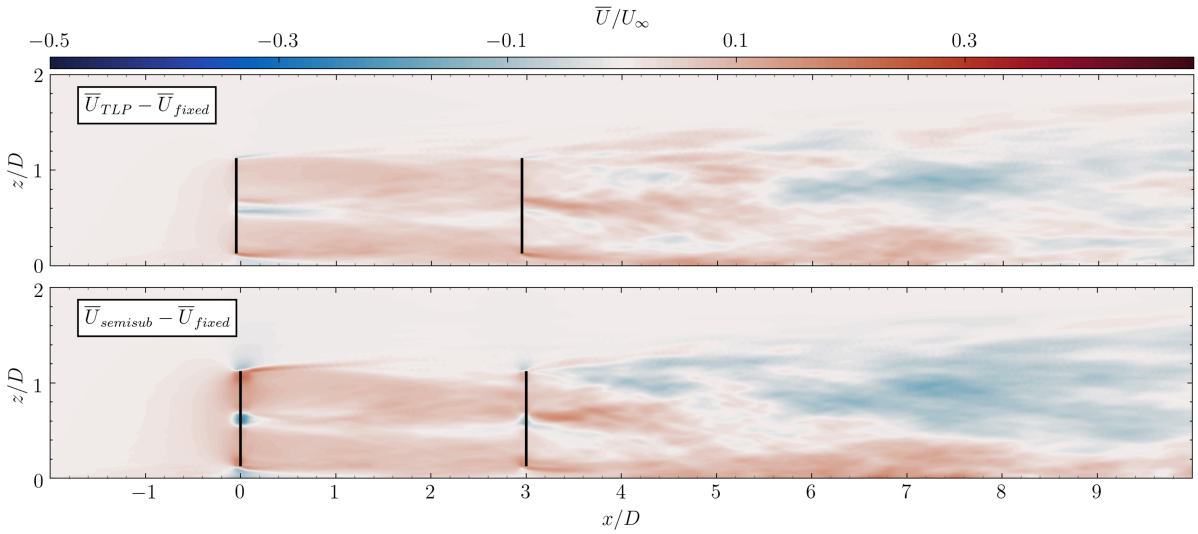

Figure 56: Averaged streamwise velocity difference between floating and fixed configurations for the $3D$ neutral ABL configurations under calm sea state (Cases 12 and 14).

The results presented are strongly related to the production of TKE near the upper wake shear layer of the wind turbines. High TKE can be observed behind both wind turbines, although it is much greater behind the second rotor. These levels persist up to 2 to 3 diameters downwind, consistent with the observations by [17, 27]. The semisub exhibits the lowest TKE in the upper rotor tip, as illustrated in Figure 57. This region corresponds spatially to the area where lower velocities can also be observed. The TLP

produces comparable levels to the fixed case, while the spar shows higher TKE in this region, with improved wake recovery in the far wake. Note that the TKE production behind the wind turbines is approximately twice as high as in the laminar inflow cases.

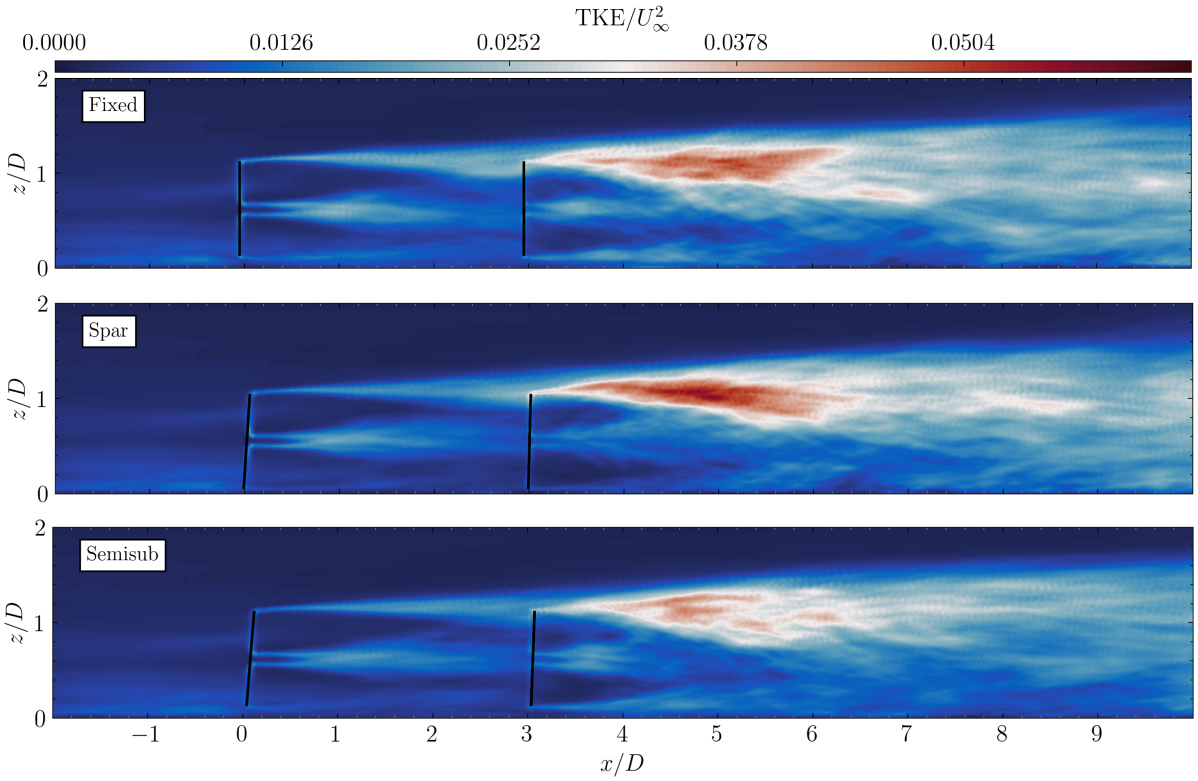

Figure 57: Turbulent kinetic energy for the $3D$ neutral ABL configurations under calm sea state (Cases 11, 13, 14).

Turbulence is consistently lower beneath the rotor level compared to the top-tip region. Xie et al. [27] attributed the lower levels to the combined effect of the turbine-induced reduced wind shear and the background wind shear. In the current results, this difference gets further accentuated behind the downstream wind turbines. Interestingly, the fixed wind turbine produces higher TI behind the first rotor ($\approx 3\%$) compared to FOWTs, which is in contrast to what was observed under laminar inflow conditions (see Figure 58). This supports the hypothesis that FOWTs promote the dissipation of large-scale turbulent structures.

Figure 59 displays the plane averaged velocities along the wake. Compared to their respective laminar inflow case, all scenarios display improved wake recovery, although the differences between FOWTs are significantly reduced. This is because, while shear tends to reduce vertical mixing [142], the ambient turbulence improves momentum exchange [141], particularly in the near wake.

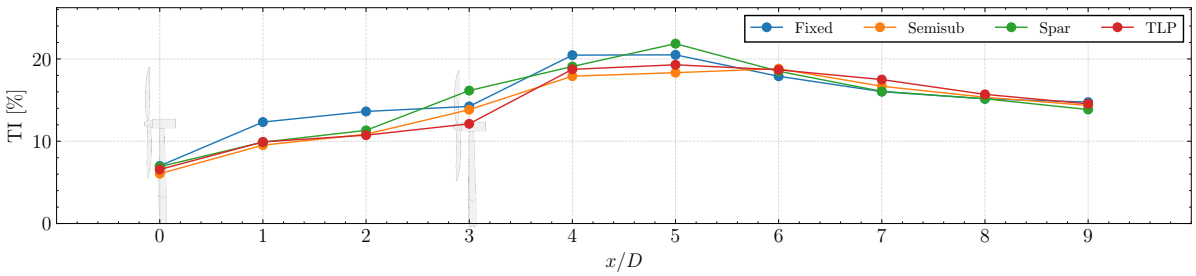

Figure 58: Streamwise averaged velocity along the wake for the $3D$ neutral ABL configurations under calm sea state (Cases 11-14).

Up to approximately $5D$ downstream, the shape of the mean velocity profiles remains relatively similar across the wind turbines. However, by $7D$, the vertical shift in the wake becomes evident. As previously discussed, both the semisub and TLP configurations show higher velocities near the lower rotor region, but reduced kinetic energy in the upper region. At $9D$, the bottom-fixed turbine produces significantly higher velocities than the semisub, while the TLP remains comparable. Notably, the spar shows the best performance overall. This suggests two possibilities: either the spar's higher motion frequency enhances wake recovery, or the closer position of the spar rotor to the ground might play a role.

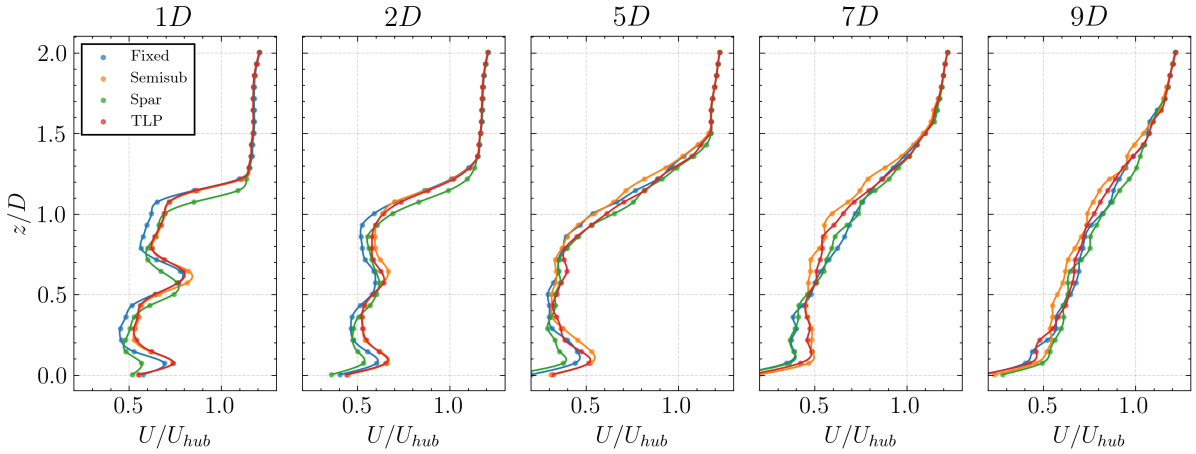

Figure 59: Streamwise averaged velocity along the wake for the $3D$ neutral ABL configurations under calm sea state (Cases 11-14).

Johlas et al. [64] performed LES-ALM simulations using SOWFA and observed similar velocity profiles during neutral ABL conditions. In their study, FOWTs exhibited better near-wake recovery. However, the far-wake velocities were weaker at the upper shear layer. The authors attributed the differences between configurations solely to the sustained rotor pitch of the FOWTs.

5.4 5D Spacing

5.4.1 Flow Field Analysis

This section presents the results obtained for the $5D$-spaced configurations. The evolution of the wake remains similar to that of the closer tandem turbines. In order to highlight any changes in the flow, the averaged velocity differences between fixed and floating wind turbines are presented in Figure 60 below.

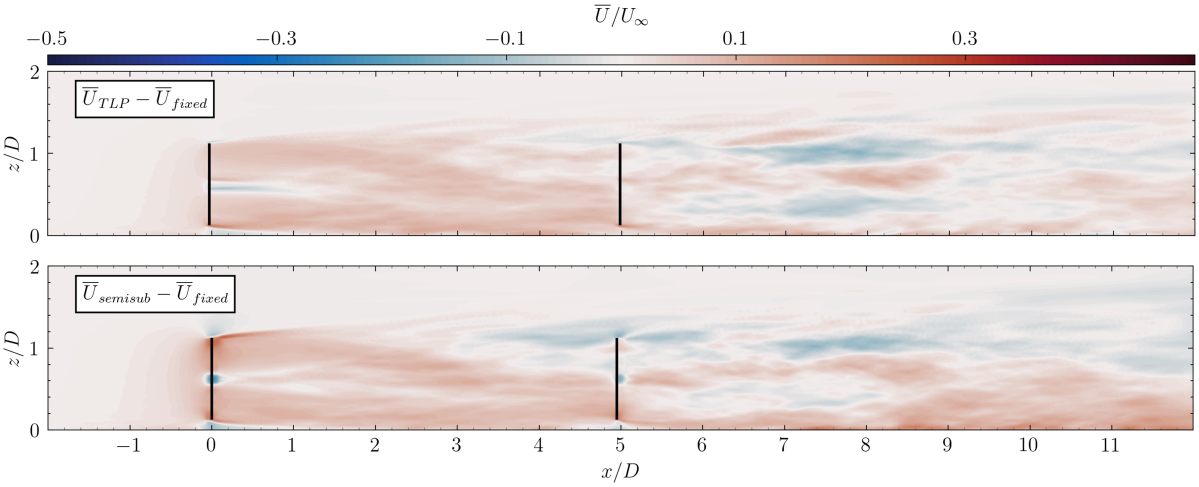

Figure 60: Averaged streamwise velocity difference between floating and fixed configurations for the $5D$ neutral ABL cases under calm sea state (Cases 16 and 18).

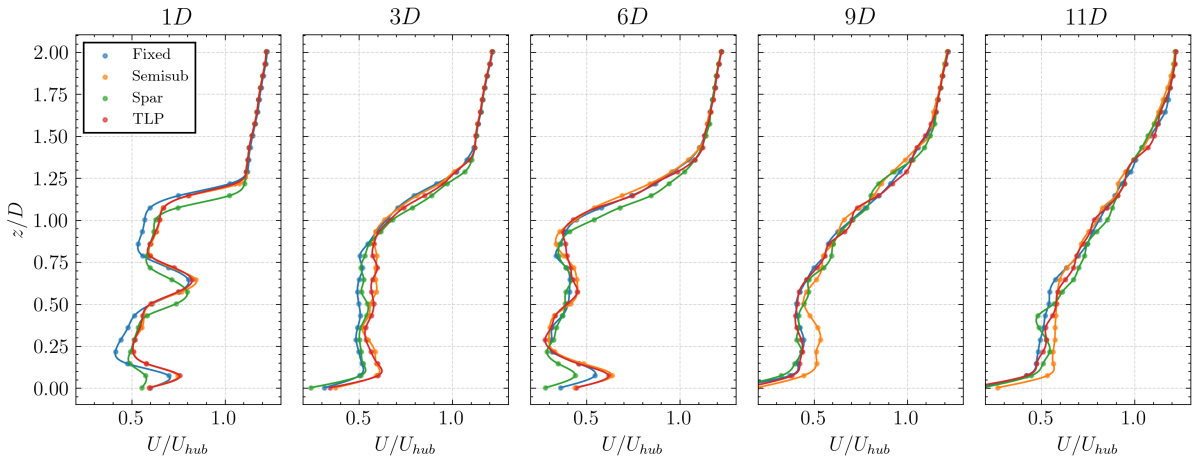

Figure 61: Streamwise averaged velocity along the wake for the $5D$ neutral ABL configurations under calm sea state (Cases 15-18).

Once again, the motion of the FOWTs increases the kinetic energy available in the upstream wake. Behind the second row, the semisub consistently shows higher velocities close to the water surface and lower velocities in the upper shear layer. The downstream TLP induces better recovery in its near wake, but the differences from the fixed configuration become smaller far downstream. The upper layers still present slightly lower wind speeds, suggesting that rotor motion may inhibit vertical mixing in the upper wake layer. Pitching, on the other hand, creates a clear separation between the bottom and top regions in the wake. The TKE profiles remain comparable to those in the 3D configurations, but with even larger and more concentrated levels in the upper shear layer behind the second row of turbines.

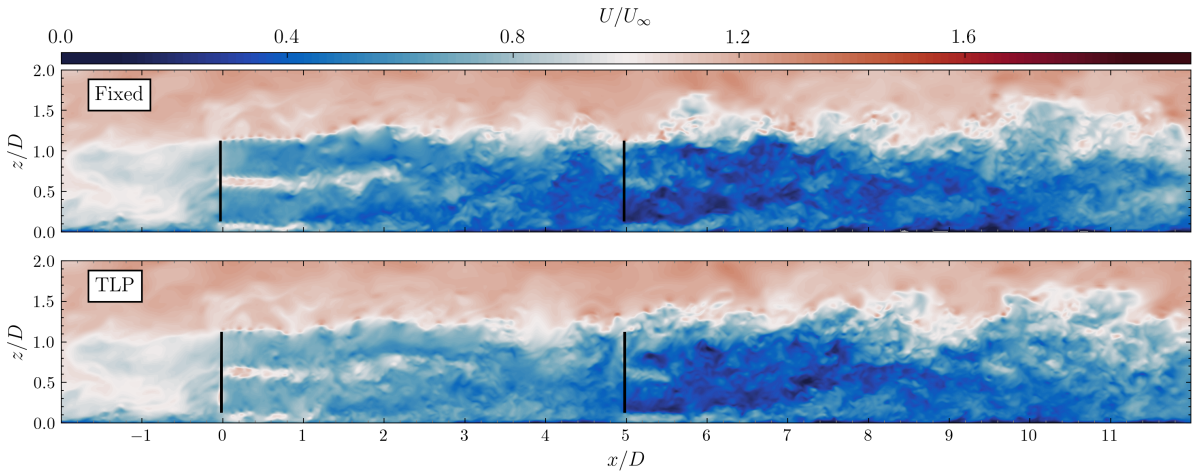

Figure 62: Instantaneous streamwise velocity for the $5D$ neutral ABL configurations under extreme sea state (Cases 15 and 19).

The flow in the extreme sea state cases does not exhibit any significant patterns or features that distinguish it from that observed under calm sea states. Resemblances of velocity fluctuations can be seen in the near wake of the freestream FOWTs, but they disappear after around 2 diameters downstream. The averaged wake statistics differ moderately from those under calm water conditions (see Appendix-A). First, the upstream near wake experiences larger velocities induced by the larger platform motions. Subsequently, the previously observed asymmetrical profile in the far wake becomes more pronounced, with even higher speeds at the bottom and reduced velocities at the top.

To investigate whether rotor motion can cause significant periodic changes in the downstream wakes under neutral ABL conditions, snapshots of the instantaneous velocity field alone have proven insufficient. As previously noted, the differences from the fixed case are minor, since the flow structures generated by platform motion are small relative to the dominant turbulent eddies. This suggests the absence of superposition effects between the ambient flow and oscillatory structures induced by motion [157]. Likewise,

the PSD plots appear considerably more chaotic compared to those under laminar conditions, without displaying noticeable peaks. According to Schliffke et al. [158], broadband motion indeed leaves no clear signatures, while harmonic motions can produce distinct signatures in the far wake energy spectra, particularly near the rotor top-tip. Pardo et al. [159] also report that the wake of a FOWT has a "memory" of harmonic surge motion, as reflected in its frequency content.

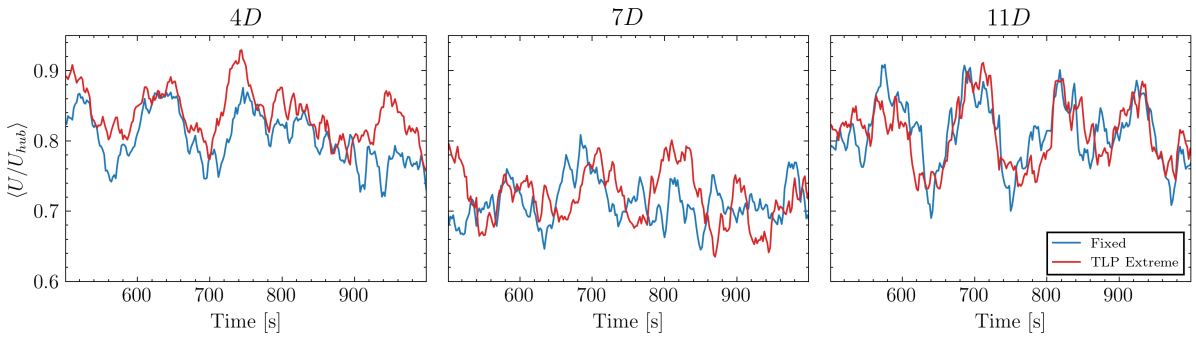

Figure 63: Plane-averaged streamwise velocity along different locations in the wake for the $5D$ neutral ABL configurations under extreme sea state (Cases 15 and 19).

Further insights can be gained by analyzing the plane-averaged streamwise velocities presented in Figure 63. As can be seen, no clear patterns of motion effects are observable by $4D$ downstream. Similarly, in the far wake behind the second turbine ($11D$), the wake evolution is very close to the reference case. However at $7D$, in the proximity of the downstream FOWT, the signal exhibits more distinct periodic oscillations compared to the fixed case, suggesting the presence of a wake signature induced by rotor movements.

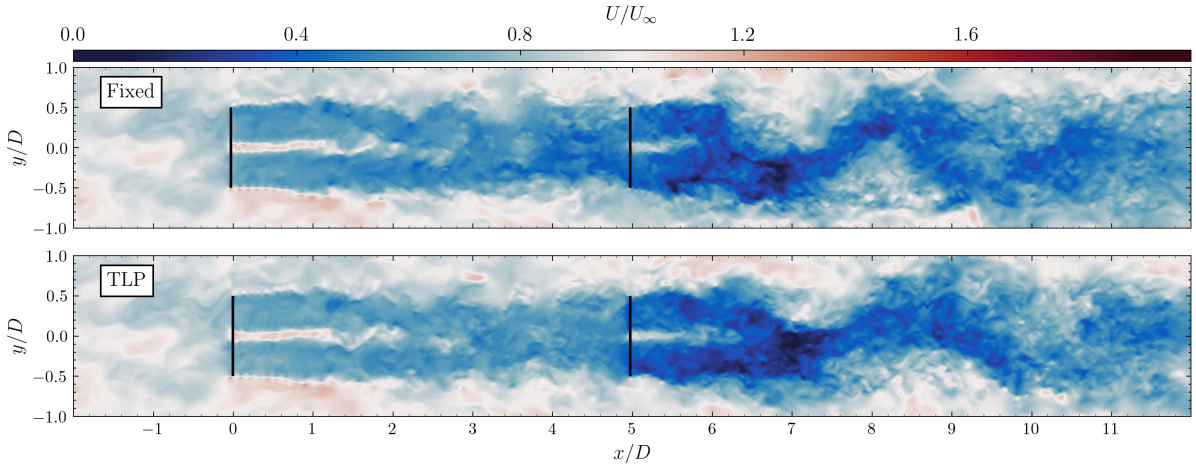

Figure 64: Instantaneous streamwise velocity for the $5D$ neutral ABL configurations under extreme sea state, top view (Cases 15 and 19).

Figure 64 shows a planar snapshot of the wind velocity for the fixed and TLP cases under extreme conditions. Pronounced lateral displacements in the wake can be observed, especially behind the second wind turbines. This phenomenon is known as wake meandering and is caused by the large turbulent structures in the incoming flow [18]. In order to effectively quantify the amplitude of these displacements, the horizontal wake centers and time temporal maxima and minima are computed (see Figure 65). The results indicate that the mean wake centers remain similar between the fixed and FOWT cases. The maxima displacements of the FOWTs appear slightly higher in the mid to far wake region.

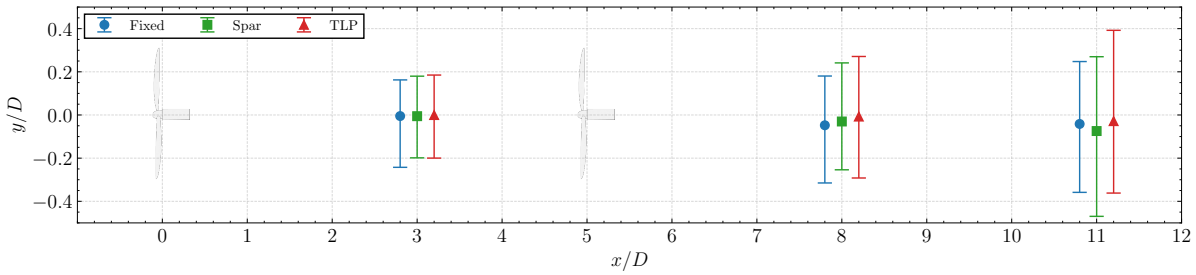

Figure 65: Horizontal wake center for different wind turbine configurations for the $5D$ neutral ABL conditions under extreme sea state (Cases 15, 19, 20).

Previous studies suggest that surge has no significant impact on wake meandering [159], but that side-to-side motions at specific frequencies can trigger larger displacements under small turbulence inflow [59]. In the current simulations, the FOWTs experience yaw, sway and roll within these frequency ranges but with very small amplitudes. Based on the current results, it cannot be firmly concluded that platform dynamics cause increased wake meandering. This is in agreement with Johlas et al. [47], who reported that under both neutral and stable ABL conditions, the differences in mean displacements remain minimal.

5.5 Turbines Performance

The power performance of the wind turbines is presented in Figures 66 and 67. Generally, the upstream FOWTs perform worse than the fixed case when operating at rated speed, while the downstream FOWTs have comparable or better production. When considering the two tandem turbines, the floating systems generate less electricity altogether. The deficit from the fixed reference diminishes as the spacing between turbines decreases. The reason is that, when placed closer to each other, FOWTs perform significantly better than the fixed configuration.

In the current simulations, the spar platforms show up to an 11% reduction in total energy output compared to the reference case. This is primarily due to the WindCrete spar design, which has a lower hub height of 15 meters.

The gap between floating and fixed turbines decreases under extreme sea states. The upstream FOWTs experience slightly lower performance than during calm waters, but the downstream ones face a large increase in generation. Notably, the second TLP generates $\approx 20\%$ more energy than the fixed counterpart.

The findings suggest that in a wind farm layout with more rows, FOWTs are likely to outperform bottom-fixed turbines. This should particularly be the case at operations below rated speed, where the upstream turbines might also benefit from higher power production due to surge and pitch motions [12]. Performance gains are also expected to be more pronounced under higher waves. However, since high-fidelity, large-scale simulations of floating wind farms have not yet been conducted in the literature, these observations require further validation through dedicated numerical studies.

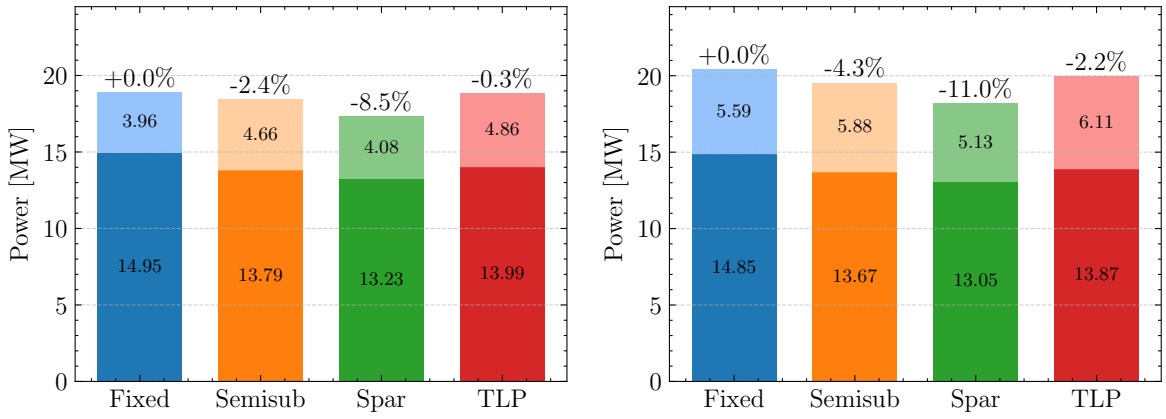

(a) $3D$ cases (b) $5D$ cases

Figure 66: Power performance of the wind turbines under neutral ABL and calm sea state. Dark colors represent first row, light colors represent second row.

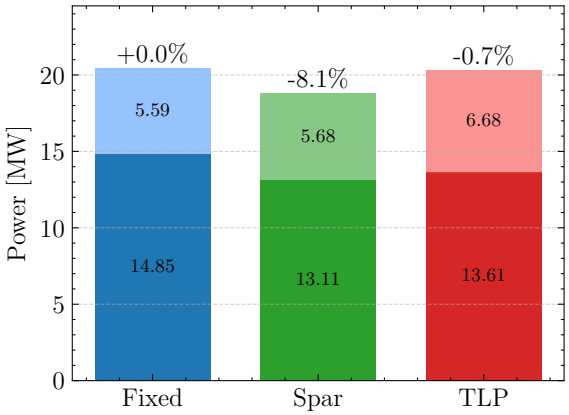

Figure 67: Power performance of the wind turbines under neutral ABL for the $5D$ configurations under extreme sea state.

5.6 Summary

In this chapter, wake interactions between different floating wind turbine concepts were examined under neutral ABL conditions. The dynamics of the platforms exhibited larger unsteadiness compared to the laminar inflow cases. In particular, the downstream semisub and spar platforms experienced a significant increase in surge and pitch, driven by the non-uniform thrust distribution and higher turbulence levels in the wake.

Fluctuations induced by the platform's motions were generally not evident, as the turbulent ambient structures dominated the wake evolution. Under extreme sea states, some oscillations were observed up to $2D$ in the near wakes. Power spectral density analysis did not reveal any clear frequency peaks in the far wake. Wake recovery increased behind all upstream FOWTs, promoted by lower thrust levels and higher mixing due to the rotor oscillations. However, beyond the second row of turbines, the differences from the fixed case became less pronounced. All FOWTs exhibited larger velocities near the bottom wake region, but reduced speeds in the upper shear layer. This asymmetry was particularly evident in cases with sustained pitch motion, such as the semisub. Overall, the flow-averaged statistics between floating and fixed turbines were much closer than during laminar inflow.

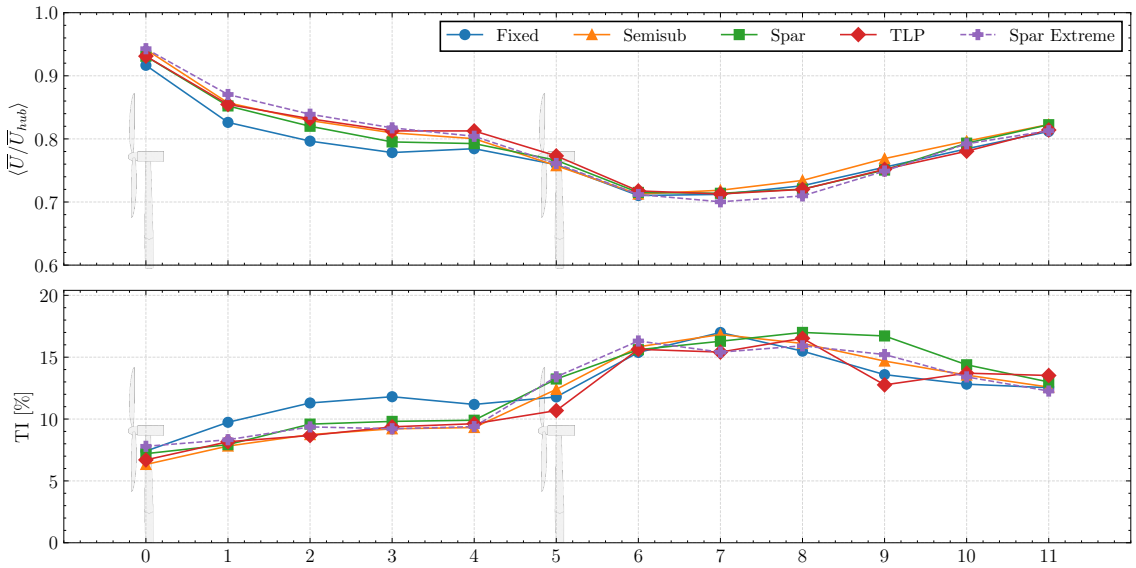

Figure 68: Comparison of the averaged streamwise velocity (top) and turbulence intensity (bot) for different wind turbine configurations under neutral ABL conditions ($\overline{U}_{hub} = 10.59$ m/s, TI = 5%).

Interestingly, fixed wind turbines produced higher turbulence levels behind the first rotor (up to 3%), which is in contrast with what was observed under laminar inflow. In the mid to far wake behind the second row, however, FOWTs exhibited higher turbulence

intensity. Analysis of the mean wake centerline showed similar results across all cases. Small increases in peak values were observed for the FOWTs, suggesting that motion might weakly enhance wake meandering.

In terms of power performance, the tandem FOWTs underperformed relative to the fixed-bottom case during both calm and extreme sea states. The upstream floaters consistently generated less electricity than their fixed counterparts. In contrast, the downstream FOWTs produced significantly more energy.

6 Conclusions

The current work aimed to develop a comprehensive understanding of wake evolution for various floating offshore wind turbine (FOWT) concepts and to identify key differences compared to the IEA-15MW reference bottom-fixed turbine. The analysis focused on wake interactions and power performance of two tandem wind turbines. Simulations considered calm and extreme sea states and included platform displacements in all six degrees of freedom (6-DOF). Both laminar inflow and a more realistic neutral atmospheric boundary layer (ABL) were investigated. The numerical framework involved a fully coupled approach between OpenFAST and AMR-Wind, where the rotor was modelled using a moving actuator line. The setup was verified and validated against existing numerical and experimental studies.

The following presents the answers to the research questions, based on the outcomes of the simulated cases:

1. **How does 6-DOF motion affect wake development and interactions of two tandem floating wind turbines?**

   The turbine's motion leads to the formation of coherent turbulent structures in the flow, along with velocity fluctuations that are caused by thrust variations induced by rotor displacements. Additionally, motion promotes vortex-pairing at the blade tips, leading to the creation of larger and stronger vortices. Among all 6-DOF, surge has the most pronounced effect on wake dynamics, while pitch and heave can further amplify flow unsteadiness. The amplitude of motions increases as the sea conditions intensify, leaving a more distinct signature in the wake. Moreover, sustained pitch introduces moderate vertical wake deflection.

   The effects of motion are more easily identifiable in laminar conditions, especially under extreme sea states. In these cases, when the downstream FOWT moves in phase with the upstream flow oscillations, the two wakes superimpose. Separated low-speed regions or "pulses" can then be observed in the downstream wake.

   Under neutral ABL conditions, the motion-induced flow features tend to dissolve quickly due to the presence of larger ambient turbulent structures. While these can persist up to $11D$ downstream in laminar flow, they are limited to the near wake (2–$3D$) in neutral ABL conditions. The freestream FOWTs exhibit faster wake recovery and lower turbulence levels compared to bottom-fixed cases. However, these differences become less distinct beyond the second row of turbines. Lastly, sustained pitch motion produces a vertical asymmetry in the mean velocity field and appears to negatively impact wake recovery in the upper shear layer.

2. **What are the key differences between TLP, Semi-Submersible and Spar floating platforms?**

   The dynamic response between platforms varies significantly in both frequency and amplitude. TLPs exhibit small, high-frequency motions with limited pitch. Spar platforms show medium-amplitude motions at relatively high frequencies, while semisubs tend to have larger, low-frequency motions. In extreme operating conditions, the motion behavior of the TLP and spar becomes very similar in magnitude, although the TLP continues to exhibit minimal pitch due to its mooring stiffness. Under neutral ABL conditions, the amplitude and unsteadiness of motion are amplified, particularly for the semisub platform.

   Downstream FOWTs experience larger displacements induced by higher turbulence levels. Wake deflection is most pronounced for the semisub, followed by the spar, while the TLP exhibits minimal deflection. Overall, wake recovery is promoted by higher frequency and larger amplitude motions in both laminar and neutral ABL conditions.

3. **How does 6-DOF motion affect the power performance of two tandem floating wind turbines?**

   Platform motions and in particular, surge, are likely to increase the mean power generation of FOWTs as they add a relative velocity component to the inflow speed. However, large sustained pitch contributes to a reduction in performance. When operating at or above rated wind speed, FOWTs tend to underperform because power production is capped by the controller, limiting the benefits of platform motions. In contrast, second-row FOWTs outperform their bottom-fixed counterparts, primarily due to higher incoming velocities in the wake of the upstream FOWTs, which become more pronounced during severe sea states. These FOWTs also benefit from the aforementioned displacement effects and experience a lower average pitch.

   Power generation differs significantly from laminar to neutral ABL inflow, with ambient turbulence significantly decreasing the power gains of downstream FOWTs. When considering just two wind systems, bottom-fixed turbines generally produce higher total power. However, for larger wind farms with multiple rows, FOWTs are expected to outperform bottom-fixed turbines.

6.1 Outlook and Recommendations

An extensive analysis has been conducted to understand the effects of motion on wake evolution and power performances of FOWTs. The findings provide valuable insights into the behavior of the most common floater concepts and can serve as a basis for optimizing the design of future floating wind farms. A few considerations related to the current setup must be addressed before discussing possible follow-up studies.

One of the primary limitations lies in the actuator line model itself, in particular its inability to properly represent blade tip vortices. This is due to the smoothing applied by the smearing function, whose width is governed by the ϵ parameter. The latter is directly related to the finest grid size, and low ϵ values cause numerical instabilities. On the other hand, if too large, the turbine experiences an overprediction of power generation compared to the reference BEM results. To address this issue, further grid refinements should be applied in the rotor region. In addition, this would allow for the generation of high-definition isosurface plots of Q-criterion, which would help examine 3D features in the wake.

Increasing mesh resolution would be beneficial to capture more precisely the motion effects on the wake, especially under calm sea states. In the current setup, the motion amplitudes of the floaters are on the order of the finest cell size, and it remains unclear whether this is sufficient to generate accurate results. This limitation has also been pointed out by other authors [64, 160].

Regarding the OpenFAST setup, it is recommended to use the newer BEM algorithm, i.e. `BEM_Mod = 2` in the aerodynamic module. This also includes the option to enable the flag `SkewMomCorr`, which should be more accurate for skewed flows and ensure a better aerodynamic representation of the pitch motion.

Within the AMR-Wind framework, the Coriolis force was excluded from the momentum source terms due to inconsistencies observed in wind direction within the refinement zones. However, omitting the Coriolis force impacts flow development and should be reconsidered in future work. Moreover, the current sampling settings have some limitations: AMR-Wind does not yet support independent sampling frequencies for point probes and planes. For this reason, it was not possible to perform a comprehensive spectral analysis of turbulence in the wake. Proper Orthogonal Decomposition could also then be conducted to extract traces of coherent structures from the flow and further investigate the wake signature induced by 6-DOF motions.

There are many research areas that require further investigation and could use the current findings as a starting point. In this study, only the blades of the turbines were represented using actuator lines, given the simplicity and widespread use in the literature. However, the tower and nacelle could be included to simulate a more realistic scenario. Additionally, the default turbine configuration should be used, i.e. including shaft-tilt and blade pre-coning. It would then be interesting to study the effect of larger vertical skewing on wake recovery.

Another direction would be to explore the role of aeroelasticity and enable blade flexibility in OpenFAST. This is reported to have some moderate impact on fixed turbines [36], but currently no high fidelity studies have looked into this for FOWTs.

An additional set of cases could include wind-wave misalignment, a common condition in the Scottish Sea. This misalignment is expected to amplify floating platform-induced

wake variations [47]. This scenario would also provide an opportunity to put a larger focus on wake meandering, as motions such and roll and sway would increase.

Furthermore, some simulations should be conducted at below-rated wind speeds to verify whether upstream FOWTs can generate more power than bottom-fixed ones. An annual energy production estimate based on a range of wind speeds should be carried out to evaluate the overall performance gains. This could also include varying sea conditions to account for more realistic operating scenarios. If computational resources allow for it, additional turbine rows should be included to test whether the performance advantage of downstream FOWTs holds in larger wind farm layouts.

Lastly, similar investigations should be conducted under both convective and stable ABL. The latter is particularly interesting as the wake signature induced by platform motion is expected to become more clearly visible [153]. Also, the wake recovery and power performance of the FOWTs are likely to change [47].

References

[1] M. Barooni, T. Ashuri, D. Velioglu Sogut, S. Wood, and S. Ghaderpour Taleghani, "Floating Offshore Wind Turbines: Current Status and Future Prospects," *Energies*, vol. 16, no. 1, p. 2, Dec. 2022. [Online]. Available: https://www.mdpi.com/1996-1073/16/1/2

[2] J. Bosch, I. Staffell, and A. D. Hawkes, "Temporally explicit and spatially resolved global offshore wind energy potentials," *Energy*, vol. 163, pp. 766–781, Nov. 2018. [Online]. Available: https://linkinghub.elsevier.com/retrieve/pii/S036054421831689X

[3] X. Wu, Y. Hu, Y. Li, J. Yang, L. Duan, T. Wang, T. Adcock, Z. Jiang, Z. Gao, Z. Lin, A. Borthwick, and S. Liao, "Foundations of offshore wind turbines: A review," *Renewable and Sustainable Energy Reviews*, vol. 104, pp. 379–393, Apr. 2019. [Online]. Available: https://linkinghub.elsevier.com/retrieve/pii/S1364032119300127

[4] A. Ghigo, L. Cottura, R. Caradonna, G. Bracco, and G. Mattiazzo, "Platform Optimization and Cost Analysis in a Floating Offshore Wind Farm," *Journal of Marine Science and Engineering*, vol. 8, no. 11, p. 835, Oct. 2020. [Online]. Available: https://www.mdpi.com/2077-1312/8/11/835

[5] S. Butterfield, W. Musial, J. Jonkman, and P. Sclavounos, "Engineering Challenges for Floating Offshore Wind Turbines." National Renewable Energy Lab. (NREL), Golden, CO (United States), Sep. 2007. [Online]. Available: https://www.osti.gov/biblio/917212

[6] B. Skaare, F. G. Nielsen, T. D. Hanson, R. Yttervik, O. Havmøller, and A. Rekdal, "Analysis of measurements and simulations from the Hywind Demo floating wind turbine: Dynamic analysis of the Hywind Demo floating wind turbine," *Wind Energy*, vol. 18, no. 6, pp. 1105–1122, Jun. 2015. [Online]. Available: https://onlinelibrary.wiley.com/doi/10.1002/we.1750

[7] M. Hannon, E. Topham, J. Dixon, D. McMillan, and M. Collu, "Offshore Wind, Ready to Float? Global and UK Trends in the Floating Offshore Wind Market," University of Strathclyde, Tech. Rep. [Online]. Available: https://strathprints.strath.ac.uk/69501/

[8] T. Stehly, P. Duffy, and D. Mulas Hernando, "2022 Cost of Wind Energy Review," Tech. Rep. NREL/PR–5000-88335, 2278805, MainId:89111, Dec. 2023. [Online]. Available: https://www.osti.gov/servlets/purl/2278805/

[9] J. Dhavle, F. Boshell, and R. Roesch, "Floating Offshore Wind Outlook," International Renewable Energy Agency, Abu Dhabi, Tech. Rep., 2024. [Online]. Available: https://www.irena.org/-/media/Files/IRENA/Agency/Publication/2024/Jul/IRENA_G7_Floating_offshore_wind_outlook_2024.pdf

[10] D. Micallef and A. Rezaeiha, "Floating offshore wind turbine aerodynamics: Trends and future challenges," *Renewable and Sustainable Energy Reviews*, vol. 152, p. 111696, Dec. 2021. [Online]. Available: https://linkinghub.elsevier.com/retrieve/pii/S1364032121009709

[11] T. Sebastian and M. Lackner, "Characterization of the unsteady aerodynamics of offshore floating wind turbines," *Wind Energy*, vol. 16, no. 3, pp. 339–352, 2013. [Online]. Available: https://onlinelibrary.wiley.com/doi/abs/10.1002/we.545

[12] H. M. Johlas, L. A. Martínez-Tossas, M. J. Churchfield, M. A. Lackner, and D. P. Schmidt, "Floating platform effects on power generation in spar and semisubmersible wind turbines," *Wind Energy*, vol. 24, no. 8, pp. 901–916, Aug. 2021. [Online]. Available: https://onlinelibrary.wiley.com/doi/10.1002/we.2608

[13] R. Farrugia, T. Sant, and D. Micallef, "A study on the aerodynamics of a floating wind turbine rotor," *Renewable Energy*, vol. 86, pp. 770–784, Feb. 2016. [Online]. Available: https://www.sciencedirect.com/science/article/pii/S0960148115302639

[14] J. McMorland, M. Collu, D. McMillan, and J. Carroll, "Operation and maintenance for floating wind turbines: A review," *Renewable and Sustainable Energy Reviews*, vol. 163, p. 112499, Jul. 2022. [Online]. Available: https://www.sciencedirect.com/science/article/pii/S1364032122004038

[15] M. O. L. Hansen, *Aerodynamics of wind turbines*, 2nd ed. London ; Sterling, VA: Earthscan, 2008, oCLC: ocm86172940.

[16] T. Burton, N. Jenkins, D. Sharpe, E. Bossanyi, and M. Graham, *Wind energy handbook*, third edition ed. Hoboken, NJ: Wiley, 2021.

[17] W. Zhang, C. D. Markfort, and F. Porté-Agel, "Near-wake flow structure downwind of a wind turbine in a turbulent boundary layer," *Experiments in Fluids*, vol. 52, no. 5, pp. 1219–1235, May 2012. [Online]. Available: http://link.springer.com/10.1007/s00348-011-1250-8

[18] F. Porté-Agel, M. Bastankhah, and S. Shamsoddin, "Wind-Turbine and Wind-Farm Flows: A Review," *Boundary-Layer Meteorology*, vol. 174, no. 1, pp. 1–59, Jan. 2020. [Online]. Available: http://link.springer.com/10.1007/s10546-019-00473-0

[19] L. Vermeer, J. Sørensen, and A. Crespo, "Wind turbine wake aerodynamics," *Progress in Aerospace Sciences*, vol. 39, no. 6-7, pp. 467–510, Aug. 2003. [Online]. Available: https://linkinghub.elsevier.com/retrieve/pii/S0376042103000782

[20] J. N. Sørensen, "Aerodynamic Analysis of Wind Turbines," in *Comprehensive Renewable Energy*. Elsevier, 2022, pp. 172–193. [Online]. Available: https://linkinghub.elsevier.com/retrieve/pii/B9780128197271001278

[21] J. N. Sørensen, R. F. Mikkelsen, D. S. Henningson, S. Ivanell, S. Sarmast, and S. J. Andersen, "Simulation of wind turbine wakes using the actuator line technique," *Philosophical Transactions of the Royal Society A: Mathematical, Physical and Engineering Sciences*, vol. 373, no. 2035, p. 20140071, Feb. 2015, publisher: Royal Society. [Online]. Available: https://royalsocietypublishing.org/doi/full/10.1098/rsta.2014.0071

[22] L. P. Chamorro and F. Porté-Agel, "A Wind-Tunnel Investigation of Wind-Turbine Wakes: Boundary-Layer Turbulence Effects," *Boundary-Layer Meteorology*, vol. 132, no. 1, pp. 129–149, Jul. 2009. [Online]. Available: https://doi.org/10.1007/s10546-009-9380-8

[23] Y.-T. Wu and F. Porté-Agel, "Atmospheric Turbulence Effects on Wind-Turbine Wakes: An LES Study," *Energies*, vol. 5, no. 12, pp. 5340–5362, Dec. 2012, number: 12 Publisher: Multidisciplinary Digital Publishing Institute. [Online]. Available: https://www.mdpi.com/1996-1073/5/12/5340

[24] N. Sezer-Uzol and O. Uzol, "Effect of steady and transient wind shear on the wake structure and performance of a horizontal axis wind turbine rotor," *Wind Energy*, vol. 16, no. 1, pp. 1–17, Jan. 2013. [Online]. Available: https://onlinelibrary.wiley.com/doi/10.1002/we.514

[25] M. J. Churchfield, S. Lee, J. Michalakes, and P. J. Moriarty, "A numerical study of the effects of atmospheric and wake turbulence on wind turbine dynamics," *Journal of Turbulence*, vol. 13, p. N14, Jan. 2012. [Online]. Available: https://www.tandfonline.com/doi/full/10.1080/14685248.2012.668191

[26] C. Santoni, K. Carrasquillo, I. Arenas-Navarro, and S. Leonardi, "Effect of tower and nacelle on the flow past a wind turbine," *Wind Energy*, vol. 20, no. 12, pp. 1927–1939, 2017. [Online]. Available: https://onlinelibrary.wiley.com/doi/abs/10.1002/we.2130

[27] S. Xie and C. Archer, "Self-similarity and turbulence characteristics of wind turbine wakes via large-eddy simulation," *Wind Energy*, vol. 18, no. 10, pp. 1815–1838, Oct. 2015. [Online]. Available: https://onlinelibrary.wiley.com/doi/10.1002/we.1792

[28] G. van Kuik, *The fluid dynamic basis for actuator disc and rotor theories*, revised second edition ed. Washington: IOS Press, 2022.

[29] B. Sanderse, "Aerodynamics of wind turbine wakes Literature review," Jan. 2009.

[30] S. Ivanell, "Wake Structures," in *Handbook of Wind Energy Aerodynamics*, B. Stoevesandt, G. Schepers, P. Fuglsang, and Y. Sun, Eds. Cham: Springer International Publishing, 2022, pp. 915–926. [Online]. Available: https://link.springer.com/10.1007/978-3-030-31307-4_48

[31] N.-J. Vermeer, J. Bemmelen, and E. Over, "How big is a tip vortex?" in *Tenth IEA Symposium on the Aerodynamics of Wind Turbines*, Dec. 1996, pp. 77–82.

[32] L. Lignarolo, D. Ragni, F. Scarano, C. Simão Ferreira, and G. Van Bussel, "Tip-vortex instability and turbulent mixing in wind-turbine wakes," *Journal of Fluid Mechanics*, vol. 781, pp. 467–493, Oct. 2015. [Online]. Available: https://www.cambridge.org/core/product/identifier/S002211201500470X/type/journal_article

[33] S. Sarmast, R. Dadfar, R. F. Mikkelsen, P. Schlatter, S. Ivanell, J. Sørensen, and D. Henningson, "Mutual inductance instability of the tip vortices behind a wind turbine," *Journal of Fluid Mechanics*, vol. 755, pp. 705–731, Sep. 2014. [Online]. Available: https://www.cambridge.org/core/product/identifier/S0022112014003267/type/journal_article

[34] T. Leweke, S. L. Dizès, and C. H. K. Williamson, "Dynamics and Instabilities of Vortex Pairs," *Annual Review of Fluid Mechanics*, vol. 48, no. Volume 48, 2016, pp. 507–541, Jan. 2016, publisher: Annual Reviews. [Online]. Available: https://www.annualreviews.org/content/journals/10.1146/annurev-fluid-122414-034558

[35] Z. Liu, Q. Li, T. Ishihara, and J. Peng, "Numerical simulations of fatigue loads on wind turbines operating in wakes," *Wind Energy*, vol. 23, no. 5, pp. 1301–1316, May 2020. [Online]. Available: https://onlinelibrary.wiley.com/doi/10.1002/we.2487

[36] F. Trigaux, P. Chatelain, and G. Winckelmans, "Investigation of blade flexibility effects on the loads and wake of a 15 MW wind turbine using a flexible actuator line method," *Wind Energy Science*, vol. 9, no. 8, pp. 1765–1789, Aug. 2024, publisher: Copernicus GmbH. [Online]. Available: https://wes.copernicus.org/articles/9/1765/2024/

[37] R. B. Stull, Ed., *An Introduction to Boundary Layer Meteorology*. Dordrecht: Springer Netherlands, 1988. [Online]. Available: http://link.springer.com/10.1007/978-94-009-3027-8

[38] S. S. Zilitinkevich and I. N. Esau, "On Integral Measures Of The Neutral Barotropic Planetary Boundary Layer," *Boundary-Layer Meteorology*, vol. 104, no. 3, pp. 371–379, Sep. 2002. [Online]. Available: http://link.springer.com/10.1023/A:1016540808958

[39] D. Allaerts, "Large-eddy Simulation of Wind Farms in Conventionally Neutral and Stable Atmospheric Boundary Layers," Ph.D. dissertation, KU Leuven, Nov. 2016.

[40] D. Allaerts and J. Meyers, "Wind farm performance in conventionally neutral atmospheric boundary layers with varying inversion strengths," *Journal of Physics: Conference Series*, vol. 524, p. 012114, Jun. 2014. [Online]. Available: https://iopscience.iop.org/article/10.1088/1742-6596/524/1/012114

[41] M. Abkar and F. Porté-Agel, "The effect of atmospheric stability on wind-turbine wakes: A large-eddy simulation study," *Journal of Physics: Conference Series*, vol. 524, p. 012138, Jun. 2014. [Online]. Available: https://iopscience.iop.org/article/10.1088/1742-6596/524/1/012138

[42] X. Yang, D. Foti, C. Kelley, D. Maniaci, and F. Sotiropoulos, "Wake Statistics of Different-Scale Wind Turbines under Turbulent Boundary Layer Inflow," *Energies*, vol. 13, no. 11, p. 3004, Jan. 2020, number: 11 Publisher: Multidisciplinary Digital Publishing Institute. [Online]. Available: https://www.mdpi.com/1996-1073/13/11/3004

[43] A. N. Robertson and J. M. Jonkman, "Loads Analysis of Several Offshore Floating Wind Turbine Concepts." OnePetro, Jun. 2011. [Online]. Available: https://dx.doi.org/

[44] Y. Huang, P. Cheng, and D. Wan, "Numerical Analysis of a Floating Offshore Wind Turbine by Coupled Aero-Hydrodynamic Simulation," *Journal of Marine Science and Application*, vol. 18, no. 1, pp. 82–92, Mar. 2019. [Online]. Available: https://doi.org/10.1007/s11804-019-00084-8

[45] J. M. Jonkman and D. Matha, "Dynamics of offshore floating wind turbines—analysis of three concepts," *Wind Energy*, vol. 14, no. 4, pp. 557–569, 2011. [Online]. Available: https://onlinelibrary.wiley.com/doi/abs/10.1002/we.442

[46] S. Hong, J. McMorland, H. Zhang, M. Collu, and K. H. Halse, "Floating offshore wind farm installation, challenges and opportunities: A comprehensive survey," *Ocean Engineering*, vol. 304, p. 117793, Jul. 2024. [Online]. Available: https://www.sciencedirect.com/science/article/pii/S0029801824011314

[47] H. M. Johlas, L. A. Martínez-Tossas, M. A. Lackner, D. P. Schmidt, and M. J. Churchfield, "Large eddy simulations of offshore wind turbine wakes for two floating platform types," *Journal of Physics: Conference Series*, vol. 1452, no. 1, p. 012034, Jan. 2020. [Online]. Available: https://iopscience.iop.org/article/10.1088/1742-6596/1452/1/012034

[48] A. J. Goupee, B. J. Koo, R. W. Kimball, K. F. Lambrakos, and H. J. Dagher, "Experimental Comparison of Three Floating Wind

Turbine Concepts," *Journal of Offshore Mechanics and Arctic Engineering*, vol. 136, no. 2, p. 020906, May 2014. [Online]. Available: https://asmedigitalcollection.asme.org/offshoremechanics/article/doi/10.1115/1.4025804/375202/Experimental-Comparison-of-Three-Floating-Wind

[49] M. Maktabi and E. Rusu, "Constant Wind Analyses on Eight Floating Wind Turbines," Nov. 2024. [Online]. Available: https://www.preprints.org/manuscript/202411.0362/v1

[50] G. R. Tomasicchio, A. M. Avossa, L. Riefolo, F. Ricciardelli, E. Musci, F. D'Alessandro, and D. Vicinanza, "Dynamic Modelling of a Spar Buoy Wind Turbine," in *Volume 10: Ocean Renewable Energy*. Trondheim, Norway: American Society of Mechanical Engineers, Jun. 2017, p. V010T09A083. [Online]. Available: https://asmedigitalcollection.asme.org/OMAE/proceedings/OMAE2017/57786/Trondheim,%20Norway/282147

[51] M. Leimeister, A. Kolios, and M. Collu, "Critical review of floating support structures for offshore wind farm deployment," *Journal of Physics: Conference Series*, vol. 1104, no. 1, p. 012007, Oct. 2018, publisher: IOP Publishing. [Online]. Available: https://dx.doi.org/10.1088/1742-6596/1104/1/012007

[52] J. G. Leishman, "Challenges in modelling the unsteady aerodynamics of wind turbines," *Wind Energy*, vol. 5, no. 2-3, pp. 85–132, Apr. 2002. [Online]. Available: https://onlinelibrary.wiley.com/doi/10.1002/we.62

[53] C. W. Schulz, S. Netzband, U. Özinan, P. W. Cheng, and M. Abdel-Maksoud, "Wind turbine rotors in surge motion: new insights into unsteady aerodynamics of floating offshore wind turbines (FOWTs) from experiments and simulations," *Wind Energy Science*, vol. 9, no. 3, pp. 665–695, Mar. 2024, publisher: Copernicus GmbH. [Online]. Available: https://wes.copernicus.org/articles/9/665/2024/

[54] H. Lee and D.-J. Lee, "Effects of platform motions on aerodynamic performance and unsteady wake evolution of a floating offshore wind turbine," *Renewable Energy*, vol. 143, pp. 9–23, Dec. 2019. [Online]. Available: https://www.sciencedirect.com/science/article/pii/S0960148119306184

[55] S. Fu, Y. Jin, Y. Zheng, and L. P. Chamorro, "Wake and power fluctuations of a model wind turbine subjected to pitch and roll oscillations," *Applied Energy*, vol. 253, p. 113605, Nov. 2019. [Online]. Available: https://linkinghub.elsevier.com/retrieve/pii/S0306261919312796

[56] S. Fu, Z. Li, W. Zhu, X. Han, X. Liang, H. Yang, and W. Shen, "Study on aerodynamic performance and wake characteristics of a floating offshore wind turbine under pitch motion," *Renewable Energy*, vol. 205, pp. 317–325, Mar. 2023. [Online]. Available: https://www.sciencedirect.com/science/article/pii/S0960148123000496

[57] Y. Li, "Numerical Investigation of Floating Wind Turbine Wake Interactions Using LES-AL Technique," Master's thesis, DTU & TU Delft, Aug. 2023.

[58] A. Arabgolarcheh, A. Rouhollahi, and E. Benini, "Analysis of middle-to-far wake behind floating offshore wind turbines in the presence of multiple platform motions," *Renewable Energy*, vol. 208, pp. 546–560, May 2023. [Online]. Available: https://www.sciencedirect.com/science/article/pii/S0960148123002616

[59] Z. Li, G. Dong, and X. Yang, "Onset of wake meandering for a floating offshore wind turbine under side-to-side motion," *Journal of Fluid Mechanics*, vol. 934, p. A29, Mar. 2022. [Online]. Available: https://www.cambridge.org/core/product/identifier/S0022112021011472/type/journal_article

[60] S. Rockel, E. Camp, J. Schmidt, J. Peinke, R. Cal, and M. Hölling, "Experimental Study on Influence of Pitch Motion on the Wake of a Floating Wind Turbine Model," *Energies*, vol. 7, no. 4, pp. 1954–1985, Mar. 2014. [Online]. Available: https://www.mdpi.com/1996-1073/7/4/1954

[61] S. Rockel, J. Peinke, M. Hölling, and R. B. Cal, "Wake to wake interaction of floating wind turbine models in free pitch motion: An eddy viscosity and mixing length approach," *Renewable Energy*, vol. 85, pp. 666–676, Jan. 2016. [Online]. Available: https://www.sciencedirect.com/science/article/pii/S0960148115301087

[62] A. Fontanella, A. Facchinetti, S. Di Carlo, and M. Belloli, "Wind tunnel investigation of the aerodynamic response of two 15 MW floating wind turbines," *Wind Energy Science*, vol. 7, no. 4, pp. 1711–1729, Aug. 2022. [Online]. Available: https://wes.copernicus.org/articles/7/1711/2022/

[63] N. Belvasi, B. Conan, B. Schliffke, L. Perret, C. Desmond, J. Murphy, and S. Aubrun, "Far-Wake Meandering of a Wind Turbine Model with Imposed Motions: An Experimental S-PIV Analysis," *Energies*, vol. 15, no. 20, p. 7757, Jan. 2022, number: 20 Publisher: Multidisciplinary Digital Publishing Institute. [Online]. Available: https://www.mdpi.com/1996-1073/15/20/7757

[64] H. M. Johlas, L. A. Martínez-Tossas, D. P. Schmidt, M. A. Lackner, and M. J. Churchfield, "Large eddy simulations of floating offshore wind turbine wakes with coupled platform motion," *Journal of Physics: Conference Series*, vol. 1256, no. 1, p. 012018, Jul. 2019. [Online]. Available: https://iopscience.iop.org/article/10.1088/1742-6596/1256/1/012018

[65] N. Troldborg, G. C. Larsen, H. A. Madsen, K. S. Hansen, J. N. Sørensen, and R. Mikkelsen, "Numerical simulations of wake interaction between two wind turbines at various inflow conditions," *Wind Energy*, vol. 14, no. 7, pp. 859–876, 2011, _eprint: https://onlinelibrary.wiley.com/doi/pdf/10.1002/we.433. [Online]. Available: https://onlinelibrary.wiley.com/doi/abs/10.1002/we.433

[66] A. Kirby, T. Nishino, and T. D. Dunstan, "Two-scale interaction of wake and blockage effects in large wind farms," *Journal of Fluid Mechanics*, vol. 953, p. A39, Dec. 2022. [Online]. Available: https://www.cambridge.org/core/product/identifier/S002211202200979X/type/journal_article

[67] K. Wang, S. Chen, J. Chen, M. Zhao, and Y. Lin, "Study on wake characteristics of fixed wind turbines and floating wind turbines arranged in tandem," *Ocean Engineering*, vol. 304, p. 117808, Jul. 2024. [Online]. Available: https://linkinghub.elsevier.com/retrieve/pii/S0029801824011466

[68] L. Carmo, J. Jonkman, and R. Thedin, "Investigating the interactions between wakes and floating wind turbines using FAST.Farm," Apr. 2024. [Online]. Available: https://wes.copernicus.org/preprints/wes-2024-40/wes-2024-40.pdf

[69] J. Cui, X. Wu, P. Lyu, T. Zhao, Q. Li, R. Ma, and Y. Liu, "Research on the Power Output of Different Floating Wind Farms Considering the Wake Effect," *Journal of Marine Science and Engineering*, vol. 12, no. 9, p. 1475, Aug. 2024. [Online]. Available: https://www.mdpi.com/2077-1312/12/9/1475

[70] L. Xue, J. Wang, L. Zhao, Z. Wei, M. Yu, and Y. Xue, "Wake Interactions of Two Tandem Semisubmersible Floating Offshore Wind Turbines Based on FAST.Farm," *Journal of Marine Science and Engineering*, vol. 10, no. 12, p. 1962, Dec. 2022. [Online]. Available: https://www.mdpi.com/2077-1312/10/12/1962

[71] T. Yao, Q. Lu, Y. Wang, Y. Zhang, L. Kuang, Z. Zhang, Y. Zhao, Z. Han, and Y. Shao, "Numerical investigation of wake-induced lifetime fatigue load of two floating wind turbines in tandem with different spacings," *Ocean Engineering*, vol. 285, p. 115464, Oct. 2023. [Online]. Available: https://www.sciencedirect.com/science/article/pii/S0029801823018486

[72] A. Arabgolarcheh, D. Micallef, A. Rezaeiha, and E. Benini, "Modelling of two tandem floating offshore wind turbines using an actuator line model," *Renewable Energy*, vol. 216, p. 119067, Nov. 2023. [Online]. Available: https://linkinghub.elsevier.com/retrieve/pii/S0960148123009813

[73] L. Zhang, Y. Li, W. Xu, Z. Gao, L. Fang, R. Li, B. Ding, B. Zhao, J. Leng, and F. He, "Systematic analysis of performance and cost of two floating offshore wind turbines with significant interactions," *Applied Energy*, vol. 321, p. 119341, Sep. 2022. [Online]. Available: https://linkinghub.elsevier.com/retrieve/pii/S0306261922006882

[74] A. Rezaeiha and D. Micallef, "Wake interactions of two tandem floating offshore wind turbines: CFD analysis using actuator disc model," *Renewable Energy*, vol. 179, pp. 859–876, Dec. 2021. [Online]. Available: https://linkinghub.elsevier.com/retrieve/pii/S0960148121010922

[75] Y. Huang, D. Wan, and C. Hu, "Numerical Study of Wake Interactions Between Two Floating Offshore Wind Turbines," Jun. 2018, pp. ISOPE–I–18–027.

[76] S. Hendriks, "Analysis of the Wake of Tandem Floating Wind Turbines," Master's thesis, DTU & TU Delft, Sep. 2024.

[77] P. Chen, J. Chen, and Z. Hu, "Review of Experimental-Numerical Methodologies and Challenges for Floating Offshore Wind Turbines," *Journal of Marine Science and Application*, vol. 19, no. 3, pp. 339–361, Sep. 2020. [Online]. Available: https://link.springer.com/10.1007/s11804-020-00165-z

[78] R. Haider, X. Li, W. Shi, Z. Lin, Q. Xiao, and H. Zhao, "Review of Computational Fluid Dynamics in the Design of Floating Offshore Wind Turbines," *Energies*, vol. 17, no. 17, p. 4269, Jan. 2024, number: 17 Publisher: Multidisciplinary Digital Publishing Institute. [Online]. Available: https://www.mdpi.com/1996-1073/17/17/4269

[79] F. Papi, J. Jonkman, A. Robertson, and A. Bianchini, "Going beyond BEM with BEM: an insight into dynamic inflow effects on floating wind turbines," *Wind Energy Science*, vol. 9, no. 5, pp. 1069–1088, May 2024. [Online]. Available: https://wes.copernicus.org/articles/9/1069/2024/

[80] C. Ferreira, W. Yu, A. Sala, and A. Viré, "Dynamic inflow model for a floating horizontal axis wind turbine in surge motion," *Wind Energy Science*, vol. 7, no. 2, pp. 469–485, Mar. 2022, publisher: Copernicus GmbH. [Online]. Available: https://wes.copernicus.org/articles/7/469/2022/

[81] K. Shaler, B. Anderson, L. A. Martínez-Tossas, E. Branlard, and N. Johnson, "Comparison of free vortex wake and blade element momentum results against large-eddy simulation results for highly flexible turbines under challenging inflow conditions," *Wind Energy Science*, vol. 8, no. 3, pp. 383–399, Mar. 2023, publisher: Copernicus GmbH. [Online]. Available: https://wes.copernicus.org/articles/8/383/2023/

[82] T. Syawitri, Y. Yao, B. Chandra, and J. Yao, "Comparison study of URANS and hybrid RANS-LES models on predicting vertical axis wind turbine performance at low, medium and high tip speed ratio ranges," *Renewable Energy*, vol. 168, pp. 247–269, May 2021. [Online]. Available: https://linkinghub.elsevier.com/retrieve/pii/S0960148120319716

[83] L. A. Martínez-Tossas, M. J. Churchfield, and S. Leonardi, "Large eddy simulations of the flow past wind turbines: actuator line and disk modeling," *Wind Energy*, vol. 18, no. 6, pp. 1047–1060, 2015. [Online]. Available: https://onlinelibrary.wiley.com/doi/abs/10.1002/we.1747

[84] J. Roenby, S. Aliyar, and H. Bredmose, "A robust algorithm for computational floating body dynamics," *Royal Society Open Science*, vol. 11, no. 4, p. 231453, Apr. 2024. [Online]. Available: https://royalsocietypublishing.org/doi/10.1098/rsos.231453

[85] Z. Yu, X. Zheng, and Q. Ma, "Study on Actuator Line Modeling of Two NREL 5-MW Wind Turbine Wakes," *Applied Sciences*, vol. 8, no. 3, p. 434, Mar. 2018, number: 3 Publisher: Multidisciplinary Digital Publishing Institute. [Online]. Available: https://www.mdpi.com/2076-3417/8/3/434

[86] P. Fleming, P. Gebraad, J. W. Wingerden, S. Lee, M. Churchfield, A. Scholbrock, J. Michalakes, K. Johnson, and P. Moriarty, "The SOWFA super-controller: A high-fidelity tool for evaluating wind plant control approaches," *European Wind Energy Conference and Exhibition, EWEC 2013*, vol. 3, pp. 1561–1570, Jan. 2013, https://www.nrel.gov/docs/fy13osti/57175.pdf.

[87] A. Croce, S. Cacciola, M. Montero Montenegro, S. Stipa, and R. Praticó, "A CFD-based analysis of dynamic induction techniques for wind farm control applications," *Wind Energy*, vol. 26, no. 3, pp. 325–343, Mar. 2023. [Online]. Available: https://onlinelibrary.wiley.com/doi/10.1002/we.2801

[88] H. M. Johlas, D. P. Schmidt, and M. A. Lackner, "Large eddy simulations of curled wakes from tilted wind turbines," *Renewable Energy*, vol. 188, pp. 349–360, Apr. 2022. [Online]. Available: https://www.sciencedirect.com/science/article/pii/S0960148122001574

[89] S. Liu, Z. Xin, L. Wang, and Z. Cai, "Fluid-structure interaction simulation of dynamic response and wake of floating offshore wind turbine considering tower shadow effect," *Acta Mechanica Sinica*, vol. 40, no. 8, p. 323567, Aug. 2024. [Online]. Available: https://link.springer.com/10.1007/s10409-024-23567-x

[90] A. Matiz-Chicacausa and O. D. Lopez, "Full Downwind Turbine Simulations Using Actuator Line Method," *Modelling and Simulation in Engineering*, vol. 2018, no. 1, p. 2536897, 2018. [Online]. Available: https://onlinelibrary.wiley.com/doi/abs/10.1155/2018/2536897

[91] A. Sharma, M. J. Brazell, G. Vijayakumar, S. Ananthan, L. Cheung, N. deVelder, M. T. Henry de Frahan, N. Matula, P. Mullowney, J. Rood, P. Sakievich, A. Almgren, P. S. Crozier, and M. Sprague, "ExaWind: Open-source CFD for hybrid-RANS/LES geometry-resolved wind turbine simulations in atmospheric flows," *Wind Energy*, vol. 27, no. 3, pp. 225–257, Mar. 2024. [Online]. Available: https://onlinelibrary.wiley.com/doi/10.1002/we.2886

[92] M. Kuhn, M. Henry de Frahan, P. Mohan, G. Deskos, M. Churchfield, L. Cheung, A. Sharma, A. Almgren, S. Ananthan, M. Brazell, L. Martínez-Tossas, R. Thedin,

J. Rood, P. Sakievich, G. Vijayakumar, W. Zhang, and M. Sprague, "AMR-Wind: A Performance-Portable, High-Fidelity Flow Solver for Wind Farm Simulations," *Wind Energy*, vol. 28, no. 5, p. e70010, May 2025. [Online]. Available: https://onlinelibrary.wiley.com/doi/10.1002/we.70010

[93] P. Crozier, R. Knaus, P. Sakievich, S. Domino, M. Barone, A. Williams, J. Overfelt, S. Ananthan, M. Henry De Frahn, G. Vijayakumar, J. Rood, A. Sharma, T. Lund, M. Churchfield, L. Martinez, and J. Melvin, "Nalu-Wind v.1.2.0," 2019, language: en. [Online]. Available: https://www.osti.gov/doecode/biblio/33223

[94] E. Muller, S. Gremmo, F. Houtin-Mongrolle, B. Duboc, and P. Bénard, "Field data based validation of an aero-servo-elastic solver for high-fidelity LES of industrial wind turbines," May 2023. [Online]. Available: https://wes.copernicus.org/preprints/wes-2023-41/wes-2023-41.pdf

[95] P. Bachant, A. Goude, daa mec, M. Wosnik, Adhyanth, and M. G. Delicious, "turbinesFoam/turbinesFoam: v0.2.1," Jan. 2025. [Online]. Available: https://zenodo.org/doi/10.5281/zenodo.14640307

[96] J.-h. Wang, W.-w. Zhao, and D.-c. Wan, "Development of naoe-FOAM-SJTU solver based on OpenFOAM for marine hydrodynamics," *Journal of Hydrodynamics*, vol. 31, no. 1, pp. 1–20, Feb. 2019. [Online]. Available: http://link.springer.com/10.1007/s42241-019-0020-6

[97] G. Campaña-Alonso, R. Martin-San-Román, B. Méndez-López, P. Benito-Cia, and J. Azcona-Armendáriz, "OF^2 : coupling OpenFAST and OpenFOAM for high fidelity aero-hydro-servo-elastic FOWT simulations," Mar. 2023. [Online]. Available: https://wes.copernicus.org/preprints/wes-2023-19/wes-2023-19.pdf

[98] P. Frontera, "CFD Simulation of a Floating Wind Turbine with OpenFOAM: an FSI approach based on the actuator line and relaxation zone methods," Master's thesis, TU Delft, Dec. 2022.

[99] G. Chourdakis, D. Schneider, and B. Uekermann, "OpenFOAM-preCICE: Coupling OpenFOAM with External Solvers for Multi-Physics Simulations," *OpenFOAM® Journal*, vol. 3, pp. 1–25, Feb. 2023. [Online]. Available: https://journal.openfoam.com/index.php/ofj/article/view/88

[100] S. Xu, X. Yang, W. Zhao, and D. Wan, "Numerical analysis of aero-hydrodynamic wake flows of a floating offshore wind turbine subjected to atmospheric turbulence inflows," *Ocean Engineering*, vol. 300, p. 117498, May 2024. [Online]. Available: https://www.sciencedirect.com/science/article/pii/S0029801824008357

[101] J. Smagorinsky, "GENERAL CIRCULATION EXPERIMENTS WITH THE PRIMITIVE EQUATIONS: I. THE BASIC EXPERIMENT*," *Monthly Weather*

Review, vol. 91, no. 3, pp. 99–164, Mar. 1963. [Online]. Available: http://journals.ametsoc.org/doi/10.1175/1520-0493(1963)091<0099:GCEWTP>2.3.CO;2

[102] A. N. Kolmogorov, "The local structure of turbulence in incompressible viscous fluid for very large Reynolds," *Numbers. In Dokl. Akad. Nauk SSSR*, vol. 30, p. 301, 1941.

[103] G. Erlebacher, M. Y. Hussaini, C. G. Speziale, and T. A. Zang, "Toward the large-eddy simulation of compressible turbulent flows," *Journal of Fluid Mechanics*, vol. 238, pp. 155–185, May 1992. [Online]. Available: https://www.cambridge.org/core/product/identifier/S0022112092001678/type/journal_article

[104] M. Germano, U. Piomelli, P. Moin, and W. H. Cabot, "A dynamic subgrid-scale eddy viscosity model," *Physics of Fluids A: Fluid Dynamics*, vol. 3, no. 7, pp. 1760–1765, Jul. 1991. [Online]. Available: https://pubs.aip.org/pof/article/3/7/1760/402287/A-dynamic-subgrid-scale-eddy-viscosity-model

[105] F. Ducros, F. Nicoud, and T. Poinsot, "Wall-adapting local eddy-viscosity models for simulations in complex geometries," *Numerical Methods for Fluid Dynamics VI*, vol. 6, pp. 293–299, 1998, publisher: Oxford University Computing Laboratory Oxford, UK.

[106] E. Bou-Zeid, C. Meneveau, and M. Parlange, "A scale-dependent Lagrangian dynamic model for large eddy simulation of complex turbulent flows," *Physics of Fluids*, vol. 17, no. 2, p. 025105, Feb. 2005. [Online]. Available: https://pubs.aip.org/pof/article/17/2/025105/895722/A-scale-dependent-Lagrangian-dynamic-model-for

[107] H. Sarlak, C. Meneveau, and J. Sørensen, "Role of subgrid-scale modeling in large eddy simulation of wind turbine wake interactions," *Renewable Energy*, vol. 77, pp. 386–399, May 2015. [Online]. Available: https://linkinghub.elsevier.com/retrieve/pii/S0960148114008635

[108] L. A. Martínez-Tossas, M. J. Churchfield, A. E. Yilmaz, H. Sarlak, P. L. Johnson, J. N. Sørensen, J. Meyers, and C. Meneveau, "Comparison of four large-eddy simulation research codes and effects of model coefficient and inflow turbulence in actuator-line-based wind turbine modeling," *Journal of Renewable and Sustainable Energy*, vol. 10, no. 3, p. 033301, May 2018. [Online]. Available: https://pubs.aip.org/jrse/article/10/3/033301/285497/Comparison-of-four-large-eddy-simulation-research

[109] W. Rozema, H. J. Bae, P. Moin, and R. Verstappen, "Minimum-dissipation models for large-eddy simulation," *Physics of Fluids*, vol. 27, no. 8, p. 085107, Aug. 2015. [Online]. Available: https://pubs.aip.org/pof/article/27/8/085107/316067/Minimum-dissipation-models-for-large-eddy

[110] M. Abkar and P. Moin, "Large-Eddy Simulation of Thermally Stratified Atmospheric Boundary-Layer Flow Using a Minimum Dissipation Model," *Boundary-Layer Meteorology*, vol. 165, no. 3, pp. 405–419, Dec. 2017. [Online]. Available: http://link.springer.com/10.1007/s10546-017-0288-4

[111] S. B. Pope, "Ten questions concerning the large-eddy simulation of turbulent flows," *New Journal of Physics*, vol. 6, pp. 35–35, Mar. 2004. [Online]. Available: https://iopscience.iop.org/article/10.1088/1367-2630/6/1/035

[112] L. Davidson, "Large Eddy Simulations: How to evaluate resolution," *International Journal of Heat and Fluid Flow*, vol. 30, no. 5, pp. 1016–1025, Oct. 2009. [Online]. Available: https://linkinghub.elsevier.com/retrieve/pii/S0142727X09001039

[113] J. N. Sorensen and W. Z. Shen, "Numerical Modeling of Wind Turbine Wakes," *Journal of Fluids Engineering*, vol. 124, no. 2, pp. 393–399, Jun. 2002. [Online]. Available: https://asmedigitalcollection.asme.org/fluidsengineering/article/124/2/393/444521/Numerical-Modeling-of-Wind-Turbine-Wakes

[114] P. F. Melani, O. S. Mohamed, S. Cioni, F. Balduzzi, and A. Bianchini, "An insight into the capability of the actuator line method to resolve tip vortices," *Wind Energy Science*, vol. 9, no. 3, pp. 601–622, Mar. 2024. [Online]. Available: https://wes.copernicus.org/articles/9/601/2024/

[115] M. J. Churchfield, S. J. Schreck, L. A. Martinez, C. Meneveau, and P. R. Spalart, "An Advanced Actuator Line Method for Wind Energy Applications and Beyond," in *35th Wind Energy Symposium*. Grapevine, Texas: American Institute of Aeronautics and Astronautics, Jan. 2017. [Online]. Available: https://arc.aiaa.org/doi/10.2514/6.2017-1998

[116] M. Schollenberger, T. Lutz, and E. Krämer, "Boundary Condition Based Actuator Line Model to Simulate the Aerodynamic Interactions at Wingtip Mounted Propellers," in *New Results in Numerical and Experimental Fluid Mechanics XII*, A. Dillmann, G. Heller, E. Krämer, C. Wagner, C. Tropea, and S. Jakirlić, Eds. Cham: Springer International Publishing, 2020, vol. 142, pp. 608–618, series Title: Notes on Numerical Fluid Mechanics and Multidisciplinary Design. [Online]. Available: http://link.springer.com/10.1007/978-3-030-25253-3_58

[117] L. A. Martínez-Tossas, M. J. Churchfield, and C. Meneveau, "Optimal smoothing length scale for actuator line models of wind turbine blades based on Gaussian body force distribution," *Wind Energy*, vol. 20, no. 6, pp. 1083–1096, Jun. 2017. [Online]. Available: https://onlinelibrary.wiley.com/doi/10.1002/we.2081

[118] L. A. Martínez-Tossas and C. Meneveau, "Filtered lifting line theory and application to the actuator line model," *Journal of Fluid Mechanics*, vol. 863, pp. 269–292, Mar. 2019. [Online]. Available: https://www.cambridge.org/core/product/identifier/S0022112018009941/type/journal_article

[119] L. A. Martínez-Tossas, P. Sakievich, M. J. Churchfield, and C. Meneveau, "Generalized filtered lifting line theory for arbitrary chord lengths and application to wind turbine blades," *Wind Energy*, vol. 27, no. 1, pp. 101–106, Jan. 2024. [Online]. Available: https://onlinelibrary.wiley.com/doi/10.1002/we.2872

[120] L. A. Martinez-Tossas, D. Allaerts, E. Branlard, and M. J. Churchfield, "A Solution Method for the Filtered Lifting Line Theory," *Journal of Fluids Engineering*, vol. 147, no. 1, p. 011502, Jan. 2025. [Online]. Available: https://asmedigitalcollection.asme.org/fluidsengineering/article/147/1/011502/1203343/A-Solution-Method-for-the-Filtered-Lifting-Line

[121] B. Jonkman, A. Platt, R. M. Mudafort, E. Branlard, L. Wang, D. Slaughter, M. Sprague, H. Ross, HaymanConsulting, jjonkman, cortadocodes, M. Chetan, R. Davies, M. Hall, G. Vijayakumar, M. Buhl, reos rcrozier, Russell9798, P. Bortolotti, R. Bergua, S. Ananthan, J. Rood, rdamiani, nrmendoza, sinolonghai, A. Gupta, psakievich, F. H. Bhuiyan, pschuenemann, and A. Sharma, "OpenFAST/openfast: v4.0.2," Feb. 2025. [Online]. Available: https://zenodo.org/doi/10.5281/zenodo.14847846

[122] R. Amaral, K. Laugesen, M. Masciola, D. Von Terzi, P. Deglaire, and A. Viré, "A frequency-time domain method for annual energy production estimation in floating wind turbines," *Journal of Physics: Conference Series*, vol. 2265, no. 4, p. 042025, May 2022. [Online]. Available: https://iopscience.iop.org/article/10.1088/1742-6596/2265/4/042025

[123] E. Gaertner, J. Rinker, L. Sethuraman, F. Zahle, B. Anderson, G. Barter, N. Abbas, F. Meng, P. Bortolotti, W. Skrzypinski, G. Scott, R. Feil, H. Bredmose, K. Dykes, M. Sheilds, C. Allen, and A. Viselli, "Definition of the IEA 15-Megawatt Offshore Reference Wind Turbine," International Energy Agency, Tech. Rep., 2020, published: NREL/TP-75698. [Online]. Available: https://www.nrel.gov/docs/fy20osti/75698.pdf

[124] C. Allen, A. Viselli, H. Dagher, A. Goupee, E. Gaertner, N. Abbas, M. Hall, and G. Barter, "Definition of the UMaine VolturnUS-S Reference Platform Developed for the IEA Wind 15-Megawatt Offshore Reference Wind Turbine," International Energy Agency, Tech. Rep., published: NREL/TP-76773.

[125] M. Y. Mahfouz, C. Molins, P. Trubat, S. Hernández, F. Vigara, A. Pegalajar-Jurado, H. Bredmose, and M. Salari, "Response of the International Energy Agency (IEA) Wind 15 MW WindCrete and Activefloat floating wind turbines to wind and second-order waves," *Wind Energy Science*, vol. 6, no. 3, pp. 867–883, Jun. 2021. [Online]. Available: https://wes.copernicus.org/articles/6/867/2021/

[126] H. Dagher, "VolturnUS Floating Offshore Wind Technology," Jan. 2022.

[127] M. Y. Mahfouz, M. Salari, and S. Hernández, "Public design and FAST models of the two 15MW floater-turbine concepts," Tech. Rep., Apr. 2020.

[128] "INF4INITY Project [HORIZON-CL5-2023-D3-01]," Tech. Rep. 101136087, Apr. 2025.

[129] "The INF4INiTY Project." [Online]. Available: https://inf4inity.com/

[130] L. Cheung, A. Hsieh, M. Blaylock, T. Herges, N. deVelder, K. Brown, P. Sakievich, D. Houck, D. Maniaci, C. Kaul, R. Rai, N. Hamilton, A. Rybchuk, R. Scott, R. Thedin, M. Brazell, M. Churchfield, and M. Sprague, "Investigations of Farm-to-Farm Interactions and Blockage Effects from AWAKEN Using Large-Scale Numerical Simulations," *Journal of Physics: Conference Series*, vol. 2505, no. 1, p. 012023, May 2023. [Online]. Available: https://iopscience.iop.org/article/10.1088/1742-6596/2505/1/012023

[131] DTU Computing Center, "DTU Computing Center resources," 2024. [Online]. Available: https://doi.org/10.48714/DTU.HPC.0001

[132] M. Penalba, A. Martinez Perurena, and M. Centeno-Telleria, "Site-specific Design Load Cases for floating offshore wind turbine applications I: Historical data," Jul. 2024. [Online]. Available: https://leopard.tu-braunschweig.de/receive/dbbs_mods_00077703

[133] P. Marek, T. Grey, and A. Hay, "A study of the variation in offshore turbulence intensity around the British Isles," Wind Europe Hamburg, 2016.

[134] G. Jeans, "Converging profile relationships for offshore wind speed and turbulence intensity," *Wind Energy Science*, vol. 9, no. 10, pp. 2001–2015, Oct. 2024. [Online]. Available: https://wes.copernicus.org/articles/9/2001/2024/

[135] R. Borges, M. Carmona, B. Costa, and W. S. Don, "An improved weighted essentially non-oscillatory scheme for hyperbolic conservation laws," *Journal of Computational Physics*, vol. 227, no. 6, pp. 3191–3211, Mar. 2008. [Online]. Available: https://linkinghub.elsevier.com/retrieve/pii/S0021999107005232

[136] J. G. Brasseur and T. Wei, "Designing large-eddy simulation of the turbulent boundary layer to capture law-of-the-wall scaling," *Physics of Fluids*, vol. 22, no. 2, Feb. 2010, publisher: AIP Publishing. [Online]. Available: https://pubs.aip.org/pof/article/22/2/021303/256409/Designing-large-eddy-simulation-of-the-turbulent

[137] H. Wurps, G. Steinfeld, and S. Heinz, "Grid-Resolution Requirements for Large-Eddy Simulations of the Atmospheric Boundary Layer," *Boundary-Layer Meteorology*, vol. 175, no. 2, pp. 179–201, May 2020. [Online]. Available: http://link.springer.com/10.1007/s10546-020-00504-1

[138] G. P. Navarro Diaz, A. D. Otero, H. Asmuth, J. N. Sørensen, and S. Ivanell, "Actuator line model using simplified force calculation methods," *Wind Energy Science*, vol. 8, no. 3, pp. 363–382, Mar. 2023, publisher: Copernicus GmbH. [Online]. Available: https://wes.copernicus.org/articles/8/363/2023/

[139] M. F. Howland, J. Bossuyt, L. A. Martínez-Tossas, J. Meyers, and C. Meneveau, "Wake structure in actuator disk models of wind turbines in yaw under uniform inflow conditions," *Journal of Renewable and Sustainable Energy*, vol. 8, no. 4, p. 043301, Jul. 2016. [Online]. Available: https://pubs.aip.org/jrse/article/8/4/043301/841090/Wake-structure-in-actuator-disk-models-of-wind

[140] Y. Li, W. Yu, and H. Sarlak, "Wake interaction of dual surging FOWT rotors in tandem," *Renewable Energy*, vol. 239, p. 122062, Feb. 2025. [Online]. Available: https://www.sciencedirect.com/science/article/pii/S096014812402130X

[141] E. L. Hodgson, M. H. A. Madsen, and S. J. Andersen, "Effects of turbulent inflow time scales on wind turbine wake behavior and recovery," *Physics of Fluids*, vol. 35, no. 9, p. 095125, Sep. 2023. [Online]. Available: https://pubs.aip.org/pof/article/35/9/095125/2911422/Effects-of-turbulent-inflow-time-scales-on-wind

[142] A. Parinam, P. Benard, D. V. Terzi, and A. Viré, "Large-Eddy Simulations of wind turbine wakes in sheared inflows," *Journal of Physics: Conference Series*, vol. 2505, no. 1, p. 012039, May 2023. [Online]. Available: https://iopscience.iop.org/article/10.1088/1742-6596/2505/1/012039

[143] M. Abkar, "Impact of Subgrid-Scale Modeling in Actuator-Line Based Large-Eddy Simulation of Vertical-Axis Wind Turbine Wakes," *Atmosphere*, vol. 9, no. 7, p. 257, Jul. 2018. [Online]. Available: https://www.mdpi.com/2073-4433/9/7/257

[144] S. N. Gadde, A. Stieren, and R. J. A. M. Stevens, "Large-Eddy Simulations of Stratified Atmospheric Boundary Layers: Comparison of Different Subgrid Models," *Boundary-Layer Meteorology*, vol. 178, no. 3, pp. 363–382, Mar. 2021. [Online]. Available: https://link.springer.com/10.1007/s10546-020-00570-5

[145] M. Ghobrial, T. Stallard, D. M. Schultz, and P. Ouro, "Evaluation of Six Subgrid-Scale Models for LES of Wind Farms in Stable and Conventionally-Neutral Atmospheric Stratification," *Boundary-Layer Meteorology*, vol. 191, no. 4, p. 19, Apr. 2025. [Online]. Available: https://link.springer.com/10.1007/s10546-025-00907-y

[146] R. Stanly, L. A. Martínez-Tossas, S. H. Frankel, and Y. Delorme, "Large-Eddy Simulation of a wind turbine using a Filtered Actuator Line Model," *Journal of Wind Engineering and Industrial Aerodynamics*, vol. 222, p. 104868, Mar. 2022. [Online]. Available: https://linkinghub.elsevier.com/retrieve/pii/S016761052100341X

[147] L. Liu, L. Franceschini, D. F. Oliveira, F. C. Galeazzo, B. S. Carmo, and R. J. A. M. Stevens, "Evaluating the accuracy of the actuator line model against blade element momentum theory in uniform inflow," *Wind Energy*, vol. 25, no. 6, pp. 1046–1059, Jun. 2022. [Online]. Available: https://onlinelibrary.wiley.com/doi/10.1002/we.2714

[148] D.-G. Caprace, P. Chatelain, and G. Winckelmans, "Lifting Line with Various Mollifications: Theory and Application to an Elliptical Wing," *AIAA Journal*, vol. 57, no. 1, pp. 17–28, Jan. 2019. [Online]. Available: https://arc.aiaa.org/doi/10.2514/1.J057487

[149] J. Lei, D.-l. Li, Y.-l. Zhou, and W. Liu, "Optimization and acceleration of flow simulations for CFD on CPU/GPU architecture," *Journal of the Brazilian Society of Mechanical Sciences and Engineering*, vol. 41, no. 7, p. 290, Jul. 2019. [Online]. Available: http://link.springer.com/10.1007/s40430-019-1793-9

[150] Y. Li, W. Yu, and H. Sarlak, "Wake Structures and Performance of Wind Turbine Rotor With Harmonic Surging Motions Under Laminar and Turbulent Inflows," *Wind Energy*, vol. 27, no. 12, pp. 1499–1525, Dec. 2024. [Online]. Available: https://onlinelibrary.wiley.com/doi/10.1002/we.2949

[151] V. G. Kleine, L. Franceschini, B. S. Carmo, A. Hanifi, and D. S. Henningson, "The stability of wakes of floating wind turbines," *Physics of Fluids*, vol. 34, no. 7, p. 074106, Jul. 2022. [Online]. Available: https://pubs.aip.org/pof/article/34/7/074106/2847059/The-stability-of-wakes-of-floating-wind-turbines

[152] F. Taruffi, R. Combette, and A. Viré, "Experimental and CFD analysis of a floating offshore wind turbine under imposed motions," *Journal of Physics: Conference Series*, vol. 2767, no. 6, p. 062010, Jun. 2024. [Online]. Available: https://iopscience.iop.org/article/10.1088/1742-6596/2767/6/062010

[153] A. Jacobsen and M. Godvik, "Influence of wakes and atmospheric stability on the floater responses of the Hywind Scotland wind turbines," *Wind Energy*, vol. 24, no. 2, pp. 149–161, Feb. 2021. [Online]. Available: https://onlinelibrary.wiley.com/doi/10.1002/we.2563

[154] E. Kleusberg, S. Benard, and D. S. Henningson, "Tip-vortex breakdown of wind turbines subject to shear," *Wind Energy*, vol. 22, no. 12, pp. 1789–1799, Dec. 2019. [Online]. Available: https://onlinelibrary.wiley.com/doi/10.1002/we.2403

[155] J. Bossuyt, R. Scott, N. Ali, and R. B. Cal, "Quantification of wake shape modulation and deflection for tilt and yaw misaligned wind turbines," *Journal of Fluid Mechanics*, vol. 917, p. A3, Jun. 2021. [Online]. Available: https://www.cambridge.org/core/product/identifier/S0022112021002378/type/journal_article

[156] K. Su and D. Bliss, "A numerical study of tilt-based wake steering using a hybrid free-wake method," *Wind Energy*, vol. 23, no. 2, pp. 258–273, Feb. 2020. [Online]. Available: https://onlinelibrary.wiley.com/doi/10.1002/we.2426

[157] L. Pagamonci, F. Papi, G. Cojocaru, M. Belloli, and A. Bianchini, "How does turbulence affect wake development in floating wind turbines? A critical assessment," Jan. 2025. [Online]. Available: https://wes.copernicus.org/preprints/wes-2024-169/

[158] B. Schliffke, B. Conan, and S. Aubrun, "Floating wind turbine motion signature in the far-wake spectral content – a wind tunnel experiment," *Wind Energy Science*, vol. 9, no. 3, pp. 519–532, Mar. 2024. [Online]. Available: https://wes.copernicus.org/articles/9/519/2024/

[159] L. Pardo Garcia, B. Conan, S. Aubrun, L. Perret, T. Piquet, C. Raibaudo, and B. Schliffke, "Experimental Analysis of the Wake Meandering of a Floating Wind Turbine under Imposed Surge Motion," *Journal of Physics: Conference Series*, vol. 2265, no. 4, p. 042003, May 2022. [Online]. Available: https://iopscience.iop.org/article/10.1088/1742-6596/2265/4/042003

[160] R. Combette, "Large-Eddy Simulation of a Floating Offshore Wind Turbine with imposed motion," Master's thesis, Delft University of Technology, Jan. 2023.

Use of Artificial Intelligence

Some aspects of the work have been supported by Artificial Intelligence (AI) through the use of ChatGPT 4.0, including:

- Assisting with post-processing and code debugging
- Rephrasing of some sentences to improve clarity
- Increasing the resolution of existing images for clearer visualization

The author remains fully responsible for the content, analysis, and conclusions presented in this thesis.

Appendix

A - Extreme Sea State

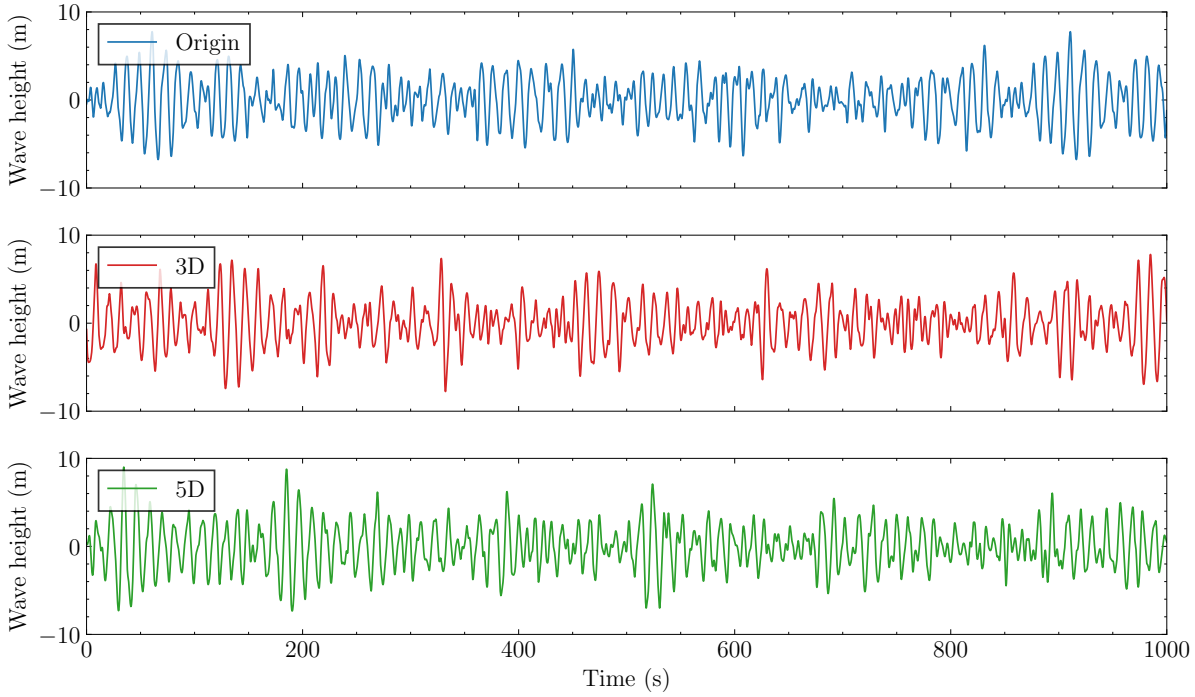

Figure 69: Wave height evolution of the extreme sea state at different spatial locations.

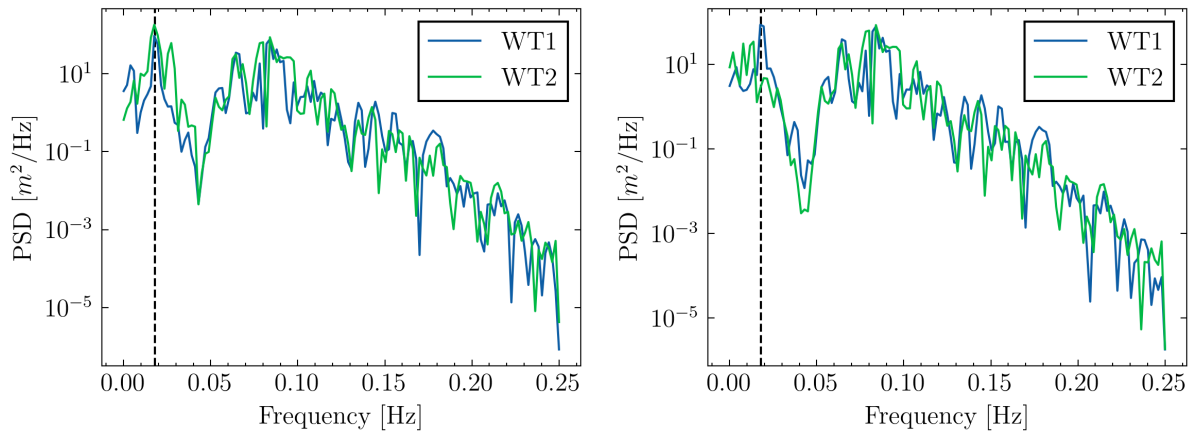

(a) Laminar inflow

(b) Neutral ABL

Figure 70: PSD of surge motion for the $5D$-spaced spar wind turbines in laminar inflow under extreme sea state (Case 10).

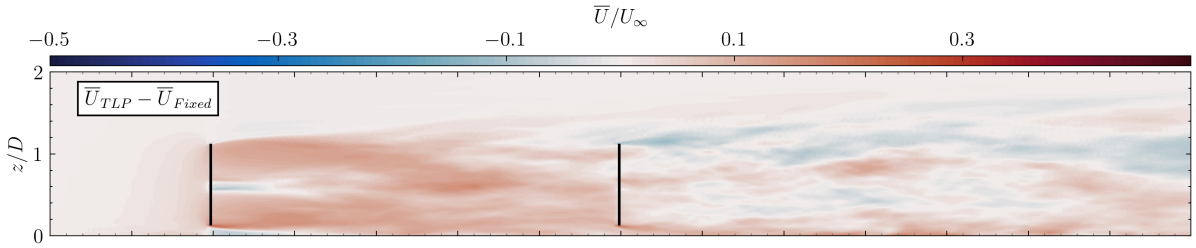

Figure 71: Streamwise averaged velocity along the wake for the $5D$ neutral ABL configurations under extreme sea state (Case 19).

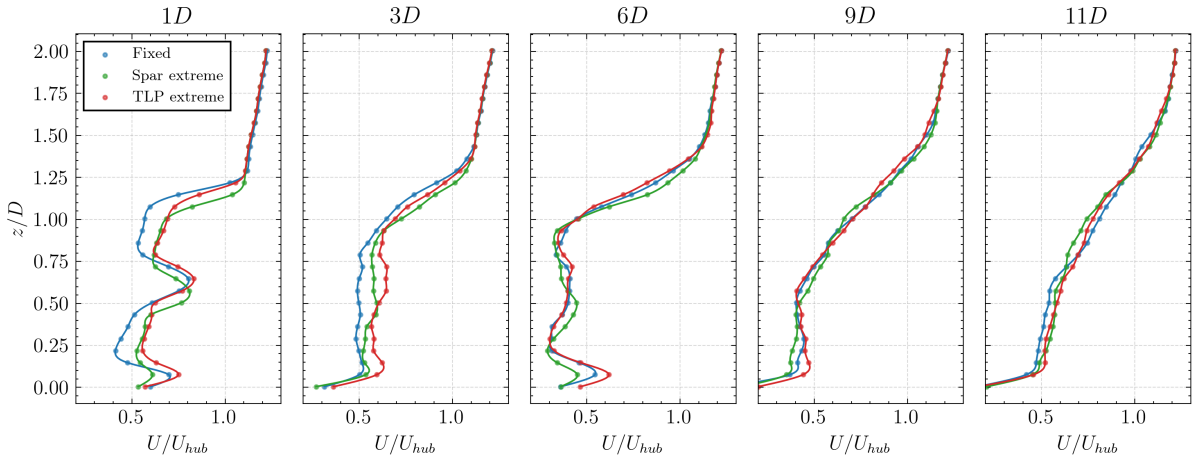

Figure 72: Streamwise averaged velocity along the wake for the $5D$ neutral ABL configurations under extreme sea state.

B - Statistical Convergence

Figure 73 shows surge and pitch motion versus simulation time. The displacements of the floaters stabilize after ≈ 600 s. Figures 74 and 75 present the backwards-looking moving average of the plane-averaged streamwise velocity, with period $\Delta t = 100$ s. The mean and standard deviation remain satisfactorily stable over time.

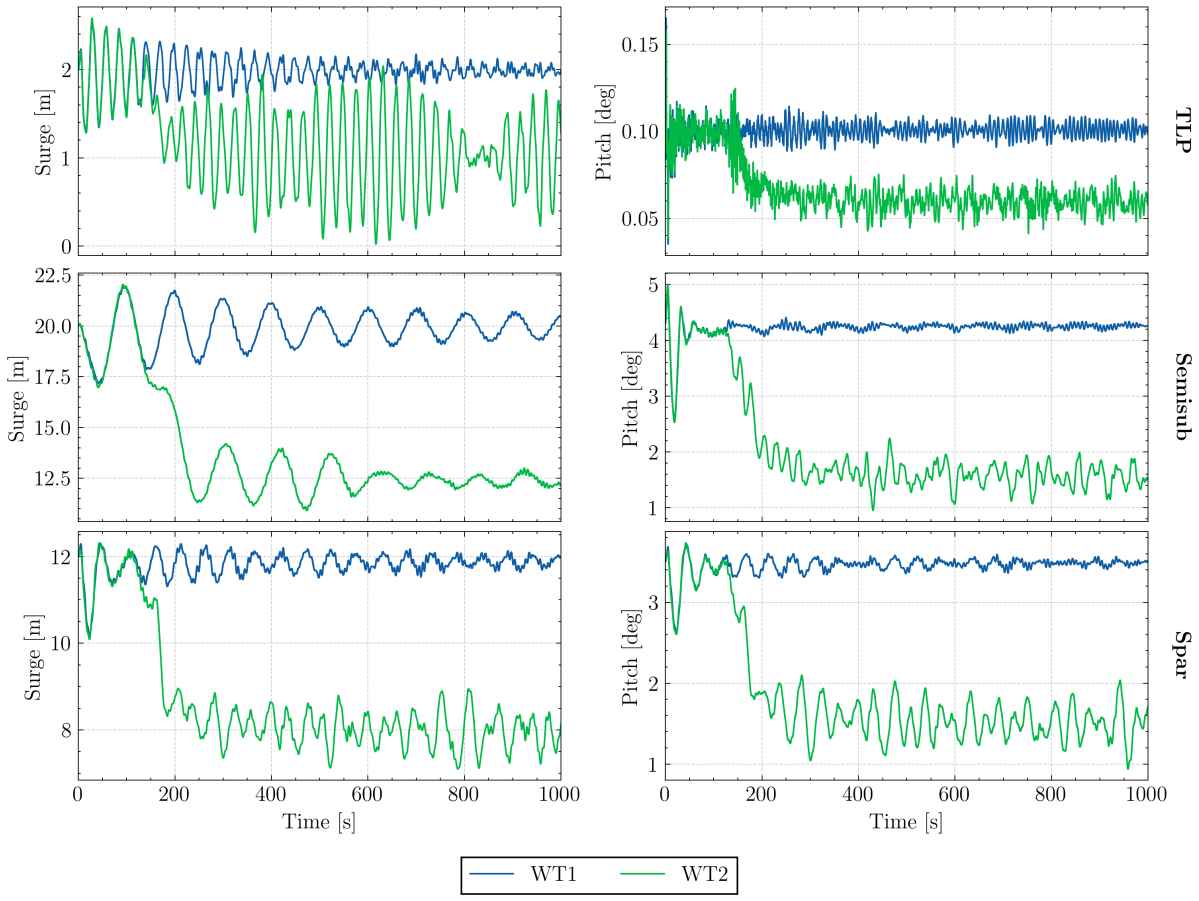

Figure 73: Surge and pitch evolution for the $5D$-spaced floating wind turbines in laminar inflow under calm sea state (Cases 6-8).

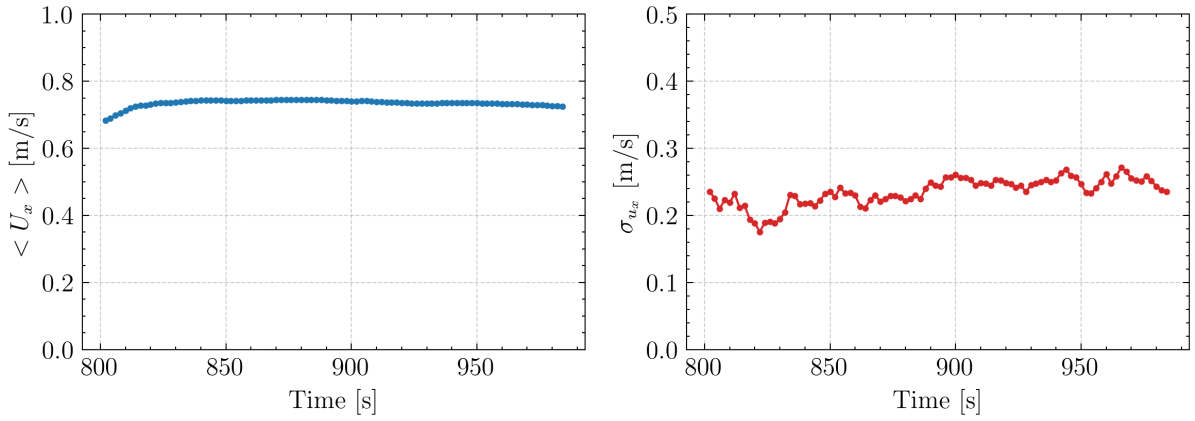

Figure 74: Moving average of the plane-averaged streamwise velocity (left) and standard deviation (right) at $10D$ in the wake for laminar inflow (Case 5).

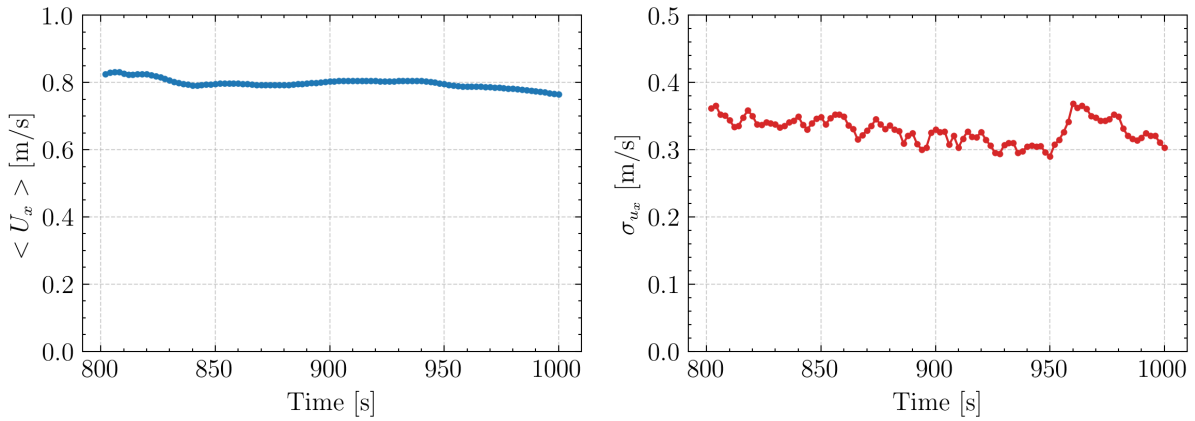

Figure 75: Moving average of the plane-averaged streamwise velocity (left) and standard deviation (right) at $10D$ in the wake for neutral ABL (Case 15).

C - Experimental Setup

Figure 76 shows the computational domain with mesh refinements used to replicate the experiment of the 1:100 scale IEA 15 MW turbine in the wind tunnel of Politecnico di Milano. The system configuration (shaft tilt, overhang, pre-cone, etc.) is reproduced closely in OpenFAST. The upstream distance is shorter than in the physical experiment, but remains sufficient for the development of the boundary layer along the wall. The downstream distance is extended to $7D$ to ensure accurate numerical results. Lateral wall spacing matches that of the wind tunnel. A log-law wall model is applied at the solid boundaries. The blockage ratio is slightly lower than in the experiment, as numerical instabilities were observed in OpenFAST when the blades were too close to the wall.

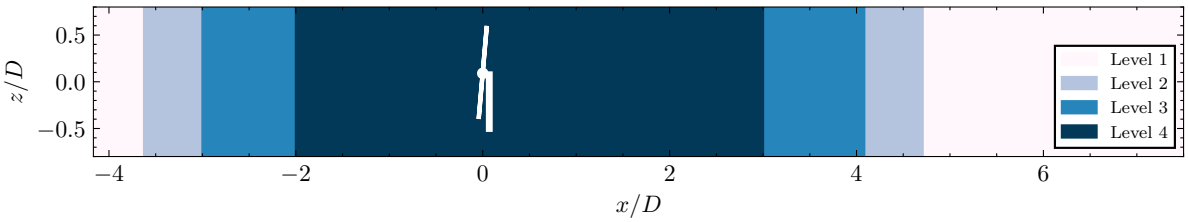

Figure 76: Lateral view of the numerical domain used for the experimental setup.

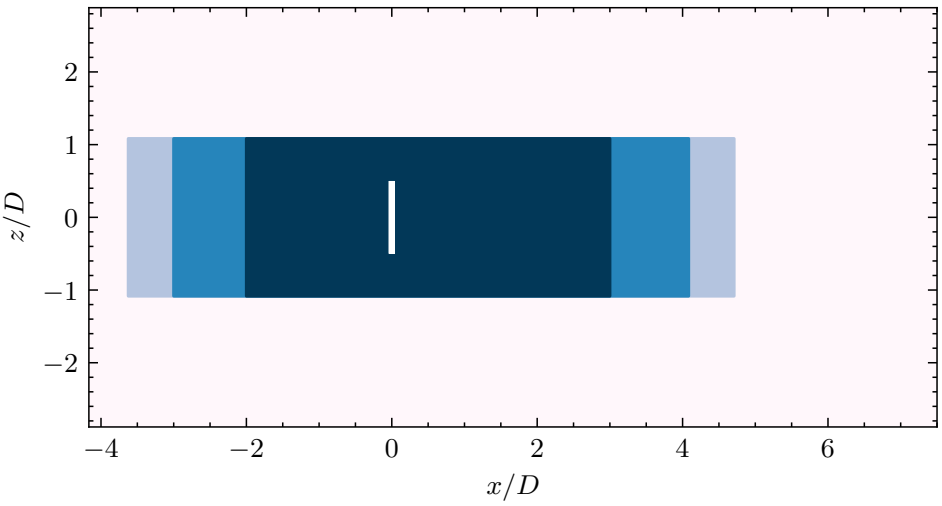

Figure 77: Upper view of the numerical domain used for the experimental setup.

D - OpenFAST Inputs

The settings of the main OpenFAST modules are reported below. For conciseness, only the relevant portions of each file are included.

Aerodyn

```
------- AERODYN v15.03.* INPUT FILE ------------------------------------------------
IEA 15 MW Offshore Reference Turbine
======  General Options  ============================================================================
False                   Echo        - Echo the input to "<rootname>.AD.ech"?  (flag)
Default                 DTAero      - Time interval for aerodynamic calculations {or "default"} (s)
0                       Wake_Mod    - Wake/induction model (switch) {0=none, 1=BEMT, 3=OLAF} [Wake_Mod cannot be 2 or 3 when linearizing]
1                       TwrPotent   - Type tower influence on wind based on potential flow around the tower (switch) {0=none, 1=baseline potential flow, 2=potential flow with Bak correction}
1                       TwrShadow   - Calculate tower influence on wind based on downstream tower shadow (switch) {0=none, 1=Powles model, 2=Eames model}
False                   TwrAero     - Calculate tower aerodynamic loads? (flag)
False                   CavitCheck  - Perform cavitation check? (flag) [UA_Mod must be 0 when CavitCheck=true]
False                   Buoyancy    - Include buoyancy effects? (flag)
False                   NacelleDrag - Include Nacelle Drag effects? (flag)
False                   CompAA      - Flag to compute AeroAcoustics calculation [used only when Wake_Mod = 1 or 2]
AeroAcousticsInput.dat AA_InputFile - AeroAcoustics input file [used only when CompAA=true]
======  Environmental Conditions  ===================================================================
"default"               AirDens     - Air density (kg/m^3)
"default"               KinVisc     - Kinematic viscosity of working fluid (m^2/s)
"default"               SpdSound    - Speed of sound in working fluid (m/s)
"default"               Patm        - Atmospheric pressure (Pa) [used only when CavitCheck=True]
"default"               Pvap        - Vapour pressure of working fluid (Pa) [used only when CavitCheck=True]
======  Blade-Element/Momentum Theory Options  ========================================================== [unused when Wake_Mod=0 or 3, except for BEM_Mod]
1                       BEM_Mod     - BEM model {1=legacy NoSweepPitchTwist, 2=polar} (switch) [used for all Wake_Mod to determine output coordinate system]
--- Skew correction
1                       Skew_Mod    - Skew model {0=No skew model, -1=Remove non-normal component for linearization, 1=skew model active}
False                   SkewMomCorr - Turn the skew momentum correction on or off [used only when Skew_Mod=1]
default                 SkewRedistr_Mod - Type of skewed-wake correction model (switch) {0=no redistribution, 1=Glauert/Pitt/Peters, default=1} [used only when Skew_Mod=1]
default                 SkewRedistrFactor - Constant used in Pitt/Peters skewed wake model {or "default" is 15/32*pi} (-) [used only when Skew_Mod=1 and SkewRedistr_Mod=1]
--- BEM algorithm
True                    TipLoss     - Use the Prandtl tip-loss model? (flag) [unused when Wake_Mod=0 or 3]
True                    HubLoss     - Use the Prandtl hub-loss model? (flag) [unused when Wake_Mod=0 or 3]
True                    TanInd      - Include tangential induction in BEMT calculations? (flag) [unused when Wake_Mod=0 or 3]
True                    AIDrag      - Include the drag term in the axial-induction calculation? (flag) [unused when Wake_Mod=0 or 3]
True                    TIDrag      - Include the drag term in the tangential-induction calculation? (flag) [unused when Wake_Mod=0,3 or TanInd=FALSE]
Default                 IndToler    - Convergence tolerance for BEMT nonlinear solve residual equation {or "default"} (-) [unused when Wake_Mod=0 or 3]
500                     MaxIter     - Maximum number of iteration steps (-) [unused when Wake_Mod=0]
--- Shear correction
False                   SectAvg     - Use sector averaging (flag)
1                       SectAvgWeighting - Weighting function for sector average {1=Uniform, default=1} within a sector centered on the blade (switch) [used only when SectAvg=True]
default                 SectAvgNPoints - Number of points per sectors (-) {default=5} [used only when SectAvg=True]
default                 SectAvgPsiBwd - Backward azimuth relative to blade where the sector starts (<=0) {default=-60} (deg) [used only when SectAvg=True]
default                 SectAvgPsiFwd - Forward azimuth relative to blade where the sector ends (>=0) {default=60} (deg) [used only when SectAvg=True]
--- Dynamic wake/inflow
2                       DBEMT_Mod   - Type of dynamic BEMT (DBEMT) model {0=No Dynamic Wake, -1=Frozen Wake for linearization, 1:constant tau1, 2=time-dependent tau1, 3=constant tau1 with continuous formulation} (-)
29.03                   tau1_const  - Time constant for DBEMT (s) [used only when Wake_Mod=2 and DBEMT_Mod=1]
======  OLAF -- cOnvecting LAgrangian Filaments (Free Vortex Wake) Theory Options  ================== [used only when Wake_Mod=3]
../IEA-15-240-RWT-OLAF/IEA-15-240-RWT_OLAF.dat OLAFInputFileName - Input file for OLAF [used only when Wake_Mod=3]
======  Unsteady Airfoil Aerodynamics Options  ====================================================
True                    AoA34       - Sample the angle of attack (AoA) at the 3/4 chord or the AC point {default=True} [always used]
3                       UA_Mod      - Unsteady Aero Model Switch (switch) {0=Quasi-steady (no UA), 2=B-L Gonzalez, 3=B-L Minnema/Pierce, 4=B-L HGM 4-states, 5=B-L HGM+vortex 5 states, 6=Oye, 7=Boeing-Vertol}
True                    FLookup     - Flag to indicate whether a lookup for f' will be calculated (TRUE) or whether best-fit exponential equations will be used (FALSE); if FALSE S1-S4 must be provided in airfoil input files (flag) [used only when UA_Mod>0]
3               IntegrationMethod  - Switch to indicate which integration method UA uses (1=RK4, 2=AB4, 3=ABM4, 4=BDF2)
```

```
0.1                     UAStartRad  - Starting radius for dynamic stall (fraction of rotor radius [0.0,1.0]) [used only when UA_Mod>0; if line is missing UAStartRad=0]
1                     UAEndRad    - Ending radius for dynamic stall (fraction of rotor radius [0.0,1.0]) [used only when UA_Mod>0; if line is missing UAEndRad=1]
```

Elastodyn

```
------- ELASTODYN v1.03.* INPUT FILE -------------------------------------------
IEA 15 MW offshore reference model on UMaine VolturnUS-S semi-submersible floating platform
---------------------- SIMULATION CONTROL --------------------------------------
False         Echo        - Echo input data to "<RootName>.ech" (flag)
          3   Method      - Integration method: {1: RK4, 2: AB4, or 3: ABM4} (-)
"default"     DT          - Integration time step (s)
---------------------- DEGREES OF FREEDOM --------------------------------------
False          FlapDOF1    - First flapwise blade mode DOF (flag)
False          FlapDOF2    - Second flapwise blade mode DOF (flag)
False          EdgeDOF     - First edgewise blade mode DOF (flag)
False         TeetDOF     - Rotor-teeter DOF (flag) [unused for 3 blades]
False         DrTrDOF     - Drivetrain rotational-flexibility DOF (flag)
True          GenDOF      - Generator DOF (flag)
False         YawDOF      - Yaw DOF (flag)
False          TwFADOF1    - First fore-aft tower bending-mode DOF (flag)
False          TwFADOF2    - Second fore-aft tower bending-mode DOF (flag)
False          TwSSDOF1    - First side-to-side tower bending-mode DOF (flag)
False          TwSSDOF2    - Second side-to-side tower bending-mode DOF (flag)
True          PtfmSgDOF   - Platform horizontal surge translation DOF (flag)
True          PtfmSwDOF   - Platform horizontal sway translation DOF (flag)
True          PtfmHvDOF   - Platform vertical heave translation DOF (flag)
True          PtfmRDOF    - Platform roll tilt rotation DOF (flag)
True          PtfmPDOF    - Platform pitch tilt rotation DOF (flag)
True          PtfmYDOF    - Platform yaw rotation DOF (flag)
---------------------- INITIAL CONDITIONS --------------------------------------
          0   OoPDefl     - Initial out-of-plane blade-tip displacement (meters)
          0   IPDefl      - Initial in-plane blade-tip deflection (meters)
         0.   BlPitch(1)  - Blade 1 initial pitch (degrees)
         0.   BlPitch(2)  - Blade 2 initial pitch (degrees)
         0.   BlPitch(3)  - Blade 3 initial pitch (degrees) [unused for 2 blades]
          0   TeetDefl    - Initial or fixed teeter angle (degrees) [unused for 3 blades]
          0   Azimuth     - Initial azimuth angle for blade 1 (degrees)
       7.55   RotSpeed    - Initial or fixed rotor speed (rpm)
          0   NacYaw      - Initial or fixed nacelle-yaw angle (degrees)
          0   TTDspFA     - Initial fore-aft tower-top displacement (meters)
          0   TTDspSS     - Initial side-to-side tower-top displacement (meters)
         20   PtfmSurge   - Initial or fixed horizontal surge translational displacement of platform (meters)
          0   PtfmSway    - Initial or fixed horizontal sway translational displacement of platform (meters)
          0   PtfmHeave   - Initial or fixed vertical heave translational displacement of platform (meters)
        0.5   PtfmRoll    - Initial or fixed roll tilt rotational displacement of platform (degrees)
        4.3   PtfmPitch   - Initial or fixed pitch tilt rotational displacement of platform (degrees)
        0.6   PtfmYaw     - Initial or fixed yaw rotational displacement of platform (degrees)
---------------------- TURBINE CONFIGURATION -----------------------------------
          3   NumBl       - Number of blades (-)
     120.97   TipRad      - The distance from the rotor apex to the blade tip (meters)
       3.97   HubRad      - The distance from the rotor apex to the blade root (meters)
          0   PreCone(1)  - Blade 1 cone angle (degrees)
          0   PreCone(2)  - Blade 2 cone angle (degrees)
          0   PreCone(3)  - Blade 3 cone angle (degrees) [unused for 2 blades]
          0   HubCM       - Distance from rotor apex to hub mass [positive downwind] (meters)
          0   UndSling    - Undersling length [distance from teeter pin to the rotor apex] (meters) [unused for 3 blades]
          0   Delta3      - Delta-3 angle for teetering rotors (degrees) [unused for 3 blades]
          0   AzimB1Up    - Azimuth value to use for I/O when blade 1 points up (degrees)
    -12.098   OverHang    - Distance from yaw axis to rotor apex [3 blades] or teeter pin [2 blades] (meters)
        0.0   ShftGagL    - Distance from rotor apex [3 blades] or teeter pin [2 blades] to shaft strain gages [positive for upwind rotors] (meters)
          0   ShftTilt    - Rotor shaft tilt angle (degrees)
     -5.125   NacCMxn     - Downwind distance from the tower-top to the nacelle CM (meters)
        0.0   NacCMyn     - Lateral  distance from the tower-top to the nacelle CM (meters)
      4.315   NacCMzn     - Vertical distance from the tower-top to the nacelle CM (meters)
        0.0   NcIMUxn     - Downwind distance from the tower-top to the nacelle IMU (meters)
        0.0   NcIMUyn     - Lateral  distance from the tower-top to the nacelle IMU (meters)
        0.0   NcIMUzn     - Vertical distance from the tower-top to the nacelle IMU (meters)
     4.3495   Twr2Shft    - Vertical distance from the tower-top to the rotor shaft (meters)
    144.386   TowerHt     - Height of tower relative to ground level [onshore], MSL [offshore wind or floating MHK], or seabed [fixed MHK] (meters)
         15   TowerBsHt   - Height of tower base relative to ground level [onshore], MSL [offshore wind or floating MHK], or seabed [fixed MHK] (meters)
          0   PtfmCMxt    - Downwind distance from the ground level [onshore], MSL [offshore wind or floating MHK], or seabed [fixed MHK] to the platform CM (meters)
          0   PtfmCMyt    - Lateral distance from the ground level [onshore], MSL [offshore wind or floating MHK], or seabed [fixed MHK] to the platform CM (meters)
    -14.400   PtfmCMzt    - Vertical distance from the ground level [onshore], MSL [offshore wind or floating MHK], or seabed [fixed MHK] to the platform CM (meters)
```

```
          0   PtfmRefzt    - Vertical distance from the ground level [onshore], MSL [offshore wind or floating MHK], or
      seabed [fixed MHK] to the platform reference point (meters)
```

SeaState

```
------- SeaState Input File ----------------------------------------------------
IEA 15 MW offshore reference model on UMaine VolturnUS-S semi-submersible floating platform
False             Echo           - Echo the input file data (flag)
---------------------- ENVIRONMENTAL CONDITIONS --------------------------------
        "default"     WtrDens        - Water density (kg/m^3)
        "default"     WtrDpth        - Water depth (meters)
        "default"     MSL2SWL        - Offset between still-water level and mean sea level (meters) [positive upward; unused
       when WaveMod = 6; must be zero if PotMod=1 or 2]
---------------------- SPATIAL DISCRETIZATION ----------------------------------------------------
            5   X_HalfWidth    - Half-width of the domain in the X direction (m) [>0, NOTE: X[nX] = nX*dX, where nX = {-NX
      +1,-NX…+2,,NX-1} and dX = X_HalfWidth/(NX-1)]
            5   Y_HalfWidth    - Half-width of the domain in the Y direction (m) [>0, NOTE: Y[nY] = nY*dY, where nY = {-NY
      +1,-NY…+2,,NY-1} and dY = Y_HalfWidth/(NY-1)]
"default"         Z_Depth        - Depth of the domain the Z direction (m) relative to SWL [0 < Z_Depth <= WtrDpth+MSL2SWL; "
      default": Z_Depth = WtrDpth+MSL2SWL; Z[nZ] = ( COS( nZ*dthetaZ ) - 1 )*Z_Depth, where nZ = …{0,1,NZ-1} and dthetaZ = pi
      /( 2*(NZ-1) )]
            2   NX             - Number of nodes in half of the X-direction domain (-) [>=2]
            2   NY             - Number of nodes in half of the Y-direction domain (-) [>=2]
           15   NZ             - Number of nodes in the Z direction (-) [>=2]
---------------------- WAVES ---------------------------------------------------
          2     WaveMod     - Incident wave kinematics model {0: none=still water, 1: regular (periodic), 1P: regular with
      user-specified phase, 2: JONSWAP/Pierson-Moskowitz spectrum (irregular), 3: White noise spectrum (irregular), 4: user-
      defined spectrum from routine UserWaveSpctrm (irregular), 5: Externally generated wave-elevation time series, 6:
      Externally generated full wave-kinematics time series [option 6 is invalid for PotMod/=0]} (switch)
          0     WaveStMod      - Model for stretching incident wave kinematics to instantaneous free surface {0: none=no
      stretching, 1: vertical stretching, 2: extrapolation stretching, 3: Wheeler stretching} (switch) [unused when WaveMod=0
       or when PotMod/=0]
         850.00  WaveTMax       - Analysis time for incident wave calculations (sec) [unused when WaveMod=0; determines
      WaveDOmega=2Pi/WaveTMax in the IFFT]
          0.25  WaveDT          - Time step for incident wave calculations     (sec) [unused when WaveMod=0; 0.1<=WaveDT
      <=1.0 recommended; determines WaveOmegaMax=Pi/WaveDT in the IFFT]
             1     WaveHs         - Significant wave height of incident waves (meters) [used only when WaveMod=1 or 2]
           7.5  WaveTp         - Peak spectral period of incident waves (sec) [used only when WaveMod=1 or 2]
        DEFAULT  WavePkShp      - Peak-shape parameter of incident wave spectrum (-) or DEFAULT (string) [used only when
      WaveMod=2; use 1.0 for Pierson-Moskowitz]
        0.111527  WvLowCOff      - Low  cut-off frequency or lower frequency limit of the wave spectrum beyond which the wave
       spectrum is zeroed (rad/s) [unused when WaveMod=0, 1, or 6]
             3.2  WvHiCOff       - High cut-off frequency or upper frequency limit of the wave spectrum beyond which the wave
       spectrum is zeroed (rad/s) [unused when WaveMod=0, 1, or 6]
          0.00  WaveDir         - Incident wave propagation heading direction                          (degrees) [unused when
       WaveMod=0 or 6]
             0     WaveDirMod     - Directional spreading function {0: none, 1: COS2S}                  (-)       [only used
      when WaveMod=2,3, or 4]
             1     WaveDirSpread  - Wave direction spreading coefficient ( > 0 )                        (-)       [only used
      when WaveMod=2,3, or 4 and WaveDirMod=1]
             1     WaveNDir       - Number of wave directions                                           (-)       [only used
      when WaveMod=2,3, or 4 and WaveDirMod=1; odd number only]
            90     WaveDirRange   - Range of wave directions (full range: WaveDir +/- 1/2*WaveDirRange) (degrees) [only used
      when WaveMod=2,3,or 4 and WaveDirMod=1]
  -561580799     WaveSeed(1)    - First  random seed of incident waves [-2147483648 to 2147483647]    (-)       [unused when
       WaveMod=0, 5, or 6]
       RANLUX     WaveSeed(2)    - Second random seed of incident waves [-2147483648 to 2147483647]    (-)       [unused when
       WaveMod=0, 5, or 6]
         TRUE     WaveNDAmp      - Flag for normally distributed amplitudes                            (flag)    [only used
      when WaveMod=2, 3, or 4]
        "none"    WvKinFile      - Root name of externally generated wave data file(s)       (quoted string)    [used only
      when WaveMod=5 or 6]
---------------------- 2ND-ORDER WAVES ------------------------------------------ [unused with WaveMod=0 or 6]
         True     WvDiffQTF      - Full difference-frequency 2nd-order wave kinematics (flag)
         True     WvSumQTF       - Full summation-frequency  2nd-order wave kinematics (flag)
            0     WvLowCOffD     - Low  frequency cutoff used in the difference-frequencies (rad/s) [Only used with a
      difference-frequency method]
       0.737863   WvHiCOffD      - High frequency cutoff used in the difference-frequencies (rad/s) [Only used with a
      difference-frequency method]
       0.314159   WvLowCOffS     - Low  frequency cutoff used in the summation-frequencies  (rad/s) [Only used with a
      summation-frequency  method]
       3.2        WvHiCOffS      - High frequency cutoff used in the summation-frequencies  (rad/s) [Only used with a
      summation-frequency  method]
---------------------- CONSTRAINED WAVES ---------------------------------------
            0   ConstWaveMod   - Constrained wave model: 0=none; 1=Constrained wave with specified crest elevation, alpha;
      2=Constrained wave with guaranteed peak-to-trough crest height, HCrest (flag)
            1   CrestHmax      - Crest height (2*alpha for ConstWaveMod=1 or HCrest for ConstWaveMod=2), must be larger
      than WaveHs (m) [unused when ConstWaveMod=0]
           60   CrestTime      - Time at which the crest appears (s) [unused when ConstWaveMod=0]
            0   CrestXi        - X-position of the crest (m) [unused when ConstWaveMod=0]
            0   CrestYi        - Y-position of the crest (m) [unused when ConstWaveMod=0]
```

```
---------------------- CURRENT ------------------------------------------------- [unused with WaveMod=6]
           0     CurrMod        - Current profile model {0: none=no current, 1: standard, 2: user-defined from routine
      UserCurrent} (switch)
           0     CurrSSV0       - Sub-surface current velocity at still water level  (m/s) [used only when CurrMod=1]
    "DEFAULT"    CurrSSDir      - Sub-surface current heading direction (degrees) or DEFAULT (string) [used only when
       CurrMod=1]
          20     CurrNSRef      - Near-surface current reference depth            (meters) [used only when CurrMod=1]
           0     CurrNSV0       - Near-surface current velocity at still water level (m/s) [used only when CurrMod=1]
           0     CurrNSDir      - Near-surface current heading direction         (degrees) [used only when CurrMod=1]
           0     CurrDIV        - Depth-independent current velocity                (m/s) [used only when CurrMod=1]
           0     CurrDIDir      - Depth-independent current heading direction    (degrees) [used only when CurrMod=1]
---------------------- MacCamy-Fuchs diffraction model ------------------------
             0   MCFD           - MacCamy-Fuchs member radius (ignored if radius <= 0) [must be 0 when WaveMod 0 or 6]
```

E - AMR-Wind Inputs

Laminar Inflow

```
#..................................#
#           SIMULATION CONTROL     #
#..................................#

time.stop_time                          = 1000               # Max (simulated) time to evolve [s]
time.max_step                           = -1
time.fixed_dt                           = 0.02               # Fixed timestep size (in seconds). If negative, then time.cfl is used
time.plot_time_interval      = 450          # in seconds
time.checkpoint_delay      = 20000        # at 400 seconds
time.checkpoint_interval                = 2500          # every 50 seconds

incflo.physics                          = FreeStream Actuator # List of physics models to include in simulation.
incflo.verbose                          = 0          # Level of detail of log outputs (0 to 3)
io.outputs                              = "actuator_src_term"
io.derived_outputs             = "mag_vorticity" "q_criterion"
io.check_file                           = chk
incflo.use_godunov                      = true
incflo.godunov_type                     = weno_z
incflo.diffusion_type                   = 1                  # Type of diffusion scheme used.  0 = explicit diffusion, 1 = Crank-Nicolson, 2 = fully implicit
turbulence.model                    = AMDNoTherm
incflo.density                          = 1.225              # Fluid density [kg/m^3]
incflo.gravity                          = 0.  0. -9.81       # Gravitational force (3D)

transport.viscosity                     = 1.464e-05          # Fluid kinematic viscosity [kg/m-s]   at 15 deg
transport.laminar_prandtl               = 0.7                # Laminar prandtl number
transport.turbulent_prandtl             = 0.3333             # Turbulent prandtl number
ConstValue.density.value                = 1.225
ConstValue.velocity.value               = 10.59 0.0 0.0

#..................................#
#            GEOMETRY & BCs        #
#..................................#

geometry.prob_lo                        = -720.0 -600.0 -600.0
geometry.prob_hi                        = 2880.0 600.0 600.0
amr.n_cell                              = 180 60 60          # Number of cells in x, y, and z directions. Currently smallest delta_x_y_z = 2.5 m
amr.max_level                           = 3
amr.blocking_factor      = 2
geometry.is_periodic                    = 0 1 1
xlo.type                                = mass_inflow
xlo.density                             = 1.225
xlo.velocity                            = 10.59 0.0 0.0
xhi.type                                = pressure_outflow


#..................................#
#              PHYSICS             #
#..................................#

ICNS.source_terms                       = ActuatorForcing
incflo.velocity                         = 10.59 0.0 0.0
io.plot_file                            = plt
io.KE_int                               = -1


#..................................#
#            MESH REFINEMENT       #
#..................................#

tagging.labels                          = newrefinement0 newrefinement1 newrefinement2

#1st refinement
tagging.newrefinement0.type             = GeometryRefinement
tagging.newrefinement0.shapes           = Level0
tagging.newrefinement0.level            = 0
tagging.newrefinement0.Level0.type      = cylinder
tagging.newrefinement0.Level0.start     = -720.0 0.0 0.0
tagging.newrefinement0.Level0.end       = 2880.0 0.0 0.0
tagging.newrefinement0.Level0.outer_radius = 360      # 3D

# 2nd refinement level
tagging.newrefinement1.type             = GeometryRefinement
tagging.newrefinement1.shapes           = Level1
tagging.newrefinement1.level            = 1
tagging.newrefinement1.Level1.type      = cylinder
tagging.newrefinement1.Level1.start     = -720.0 0.0 0.0
```

```
tagging.newrefinement1.Level1.end        = 2880.0 0.0 0.0
tagging.newrefinement1.Level1.outer_radius = 240      # 2D

# 3rd refinement level
tagging.newrefinement2.type              = GeometryRefinement
tagging.newrefinement2.shapes            = Level2
tagging.newrefinement2.level             = 2
tagging.newrefinement2.Level2.type       = cylinder
tagging.newrefinement2.Level2.start      = -480.0 0.0 0.0       # -2D
tagging.newrefinement2.Level2.end        = 2880.0 0.0 0.0
tagging.newrefinement2.Level2.outer_radius = 170    # 1.4D


#...................................#
#              TURBINES             #
#...................................#

Actuator.type                            = TurbineFastLine
Actuator.TurbineFastLine.epsilon         = 2.5 2.5 2.5         # based on delta_x. Currently eps = delta_x * 1
Actuator.TurbineFastLine.fllc            = true
Actuator.TurbineFastLine.fllc_nonuniform = 1
Actuator.TurbineFastLine.fllc_type   = variable_chord
Actuator.TurbineFastLine.fllc_eps_dr_ratio = 3
Actuator.TurbineFastLine.fllc_start_time = 5
Actuator.TurbineFastLine.density         = 1.225

Actuator.labels                          = T0 T1


Actuator.T0.type                         = TurbineFastLine
Actuator.T0.openfast_input_file          = T1_IEA-15-240-RWT-UMaineSemi/IEA-15-240-RWT-UMaineSemi.fst
Actuator.T0.base_position                = 0.0 0.0 -150.0
Actuator.T0.rotor_diameter               = 240.0
Actuator.T0.hub_height                   = 150.0
Actuator.T0.num_points_blade             = 300
Actuator.T0.num_points_tower             = 0
Actuator.T0.fllc                         = true
Actuator.T0.epsilon              = 2.5 2.5 2.5
Actuator.T0.epsilon_min          = 2.5 2.5 2.5
Actuator.T0.epsilon_chord        = 0.25 0.25 0.25
Actuator.T0.openfast_start_time          = 0.0
Actuator.T0.openfast_stop_time           = 1000.0
Actuator.T0.nacelle_drag_coeff           = 0.0
Actuator.T0.nacelle_area                 = 0.0
Actuator.T0.yaw                          = 0
Actuator.T0.output_frequency             = 10
Actuator.T0.num_blades                   = 3
Actuator.T0.use_tip_correction           = true
Actuator.T0.use_root_correction          = true


Actuator.T1.type                         = TurbineFastLine
Actuator.T1.openfast_input_file          = T2_IEA-15-240-RWT-UMaineSemi/IEA-15-240-RWT-UMaineSemi.fst
Actuator.T1.base_position                = 1200.0 0.0 -150.0  # 5D
Actuator.T1.rotor_diameter               = 240.0
Actuator.T1.hub_height                   = 150.0
Actuator.T1.num_points_blade             = 300
Actuator.T1.num_points_tower             = 0
Actuator.T1.fllc                         = true
Actuator.T1.epsilon              = 2.5 2.5 2.5
Actuator.T1.epsilon_min          = 2.5 2.5 2.5
Actuator.T1.epsilon_chord        = 0.25 0.25 0.25
Actuator.T1.openfast_start_time          = 0.0
Actuator.T1.openfast_stop_time           = 1000.0
Actuator.T1.nacelle_drag_coeff           = 0.0
Actuator.T1.nacelle_area                 = 0.0
Actuator.T1.yaw                          = 0
Actuator.T1.output_frequency             = 10
Actuator.T1.num_blades                   = 3
Actuator.T1.use_tip_correction           = true
Actuator.T1.use_root_correction          = true



#...................................#
#              SAMPLING             #
#...................................#

incflo.post_processing                   = sampling averaging
sampling.type                            = Sampling
sampling.output_frequency                = 100      #frequency*dt -- every 2 sec
sampling.fields                          = velocity p
sampling.derived_fields            = mag_vorticity mag_strainrate

sampling.labels                          = xy-domain xz-domain vert-line-yz0 vert-line-yz1 vert-line-yz2  vert-line-yz3 vert
      -line-yz4 vert-line-yz5 vert-line-yz6 vert-line-yz7 vert-line-yz8 vert-line-yz9 vert-line-yz10 vert-line-yz11

```

```
163
164 # XY-plane: Capturing flow at hub height
165 sampling.xy-domain.type                  = PlaneSampler
166 sampling.xy-domain.num_points            = 1345 193     # every 2.5m
167 sampling.xy-domain.origin                = -480.0 -240.0 0    #-2D
168 sampling.xy-domain.axis1                 = 3360.0 0.0 0.0   #7D
169 sampling.xy-domain.axis2                 = 0.0 480.0 0.0
170
171 # XZ-plane: Along the streamwise direction
172 sampling.xz-domain.type                  = PlaneSampler
173 sampling.xz-domain.num_points            = 1345 193
174 sampling.xz-domain.origin                = -480.0 0.0 -240.0    # -2D
175 sampling.xz-domain.axis1                 = 3360.0 0.0 0.0
176 sampling.xz-domain.axis2                 = 0.0 0.0 480.0
177
178
179 #Line Sampling
180
181 # Vertical line sampler in YZ-plane (along Z-axis, through full rotor diameter)     at 0D downstream
182 sampling.vert-line-yz0.type               = LineSampler
183 sampling.vert-line-yz0.num_points         = 29
184 sampling.vert-line-yz0.start              = 0.0 0.0 -240.0
185 sampling.vert-line-yz0.end                = 0.0 0.0 240.0
186
187 # Vertical line sampler in YZ-plane (along Z-axis, through full rotor diameter)     at 1D downstream
188 sampling.vert-line-yz1.type               = LineSampler
189 sampling.vert-line-yz1.num_points         = 29
190 sampling.vert-line-yz1.start              = 240 0.0 -240.0
191 sampling.vert-line-yz1.end                = 240 0.0 240.0
192
193 # Vertical line sampler in YZ-plane (along Z-axis, through full rotor diameter)     at 2D downstream
194 sampling.vert-line-yz2.type               = LineSampler
195 sampling.vert-line-yz2.num_points         = 29
196 sampling.vert-line-yz2.start              = 480 0.0 -240.0
197 sampling.vert-line-yz2.end                = 480 0.0 240.0
198
199 ...
200
201 # Vertical line sampler in YZ-plane (along Z-axis, through full rotor diameter)     at 11D downstream
202 sampling.vert-line-yz11.type              = LineSampler
203 sampling.vert-line-yz11.num_points        = 29
204 sampling.vert-line-yz11.start             = 2640 0.0 -240.0
205 sampling.vert-line-yz11.end               = 2640 0.0 240.0
206
207
208 #== END AMR-WIND INPUT ==
```

Neutral ABL

```
1  #....................................#
2  #           SIMULATION STOP          #
3  #....................................#
4  time.stop_time                   =   46000.0     # Max (simulated) time to evolve, 30 hours
5  #time.max_step                   =   10          # Max number of time steps
6  incflo.verbose                   =   0         # incflo_level
7
8  #....................................#
9  #         TIME STEP COMPUTATION      #
10 #....................................#
11 time.fixed_dt                =   0.02       # Use this constant dt if > 0
12 #time.cfl                    =   0.95         # CFL factor
13
14 #....................................#
15 #           INPUT AND OUTPUT         #
16 #....................................#
17 time.plot_time_interval      = 800 # in seconds
18 time.checkpoint_delay      = 20000 # at 400 seconds
19 time.checkpoint_interval                = 10000  # every 200 seconds
20
21
22 #....................................#
23 #              PHYSICS               #
24 #....................................#
25 incflo.gravity               =   0.  0. -9.81  # Gravitational force (3D)
26 incflo.density                 = 1.225          # Reference density
27 io.restart_file                          = ../abl_spinup_nuovo/chk120000
28
29 ## Solver options
30 incflo.use_godunov       = 1
31 incflo.godunov_type        = weno_z
32 incflo.diffusion_type        = 1
```

```
turbulence.model       = AMD


## Physical parameters
transport.viscosity        = 0.0  # In AMR-Wind, they always set to zero
transport.laminar_prandtl      = 0.7
transport.turbulent_prandtl      = 0.3333

diffusion.max_order        = 1

mac_proj.mg_verbose        = 1
nodal_proj.mg_verbose        = 1

diffusion.mg_rtol        = 1.0e-5
diffusion.mg_atol        = 1.0e-10

mac_proj.mg_rtol       = 1.0e-5
mac_proj.mg_atol       = 1.0e-10

nodal_proj.mg_rtol       = 1.0e-5
nodal_proj.mg_atol       = 1.0e-10


#.....................................#
#              GEOMETRY               #
#.....................................#

geometry.prob_lo             =   0.     0.     0.  # Lo corner coordinates
geometry.prob_hi             =   4080  2560.   960.  # Hi corner coordinates
geometry.is_periodic         =   0   0   0   # Periodicity x y z

amr.n_cell                   = 204 128 48 # Grid cells at coarsest AMRlevel
amr.max_level                = 3           # Max AMR level in hierarchy
amr.blocking_factor      = 2


# Boundary conditions

xlo.type                                = mass_inflow
xhi.type                                = pressure_outflow
xlo.density                             = 1.225
xlo.temperature                         = 290.0


ylo.type                                = slip_wall
yhi.type                                = slip_wall

zlo.type         = wall_model
zhi.type         = slip_wall
zhi.temperature_type        = fixed_gradient
zhi.temperature        = 0.003 # tracer is used to specify potential temperature gradient

#.....................................#
#            MESH REFINEMENT          #
#.....................................#

tagging.labels                          = newrefinement0 newrefinement1 newrefinement2

#1st refinement
tagging.newrefinement0.type             = GeometryRefinement
tagging.newrefinement0.shapes           = Level0
tagging.newrefinement0.level            = 0
tagging.newrefinement0.Level0.type      = box
tagging.newrefinement0.Level0.origin    = 0.0 500.0 0.0
tagging.newrefinement0.Level0.xaxis     = 4080.0 0.0 0.0
tagging.newrefinement0.Level0.yaxis     = 0.0 1560.0 0.0
tagging.newrefinement0.Level0.zaxis     = 0.0 0.0 960.0

tagging.newrefinement1.type             = GeometryRefinement
tagging.newrefinement1.shapes           = Level1
tagging.newrefinement1.level            = 1
tagging.newrefinement1.Level1.type      = box
tagging.newrefinement1.Level1.origin    = 400 1040.0 0.0
tagging.newrefinement1.Level1.xaxis     = 3640.0 0.0 0.0
tagging.newrefinement1.Level1.yaxis     = 0.0 480.0 0.0
tagging.newrefinement1.Level1.zaxis     = 0.0 0.0 400.0

tagging.newrefinement2.type             = GeometryRefinement
tagging.newrefinement2.shapes           = Level2
tagging.newrefinement2.level            = 2
tagging.newrefinement2.Level2.type      = box
tagging.newrefinement2.Level2.origin    = 480 1100 10.0
tagging.newrefinement2.Level2.xaxis     = 3520.0 0.0 0.0
tagging.newrefinement2.Level2.yaxis     = 0.0 350.0 0.0
tagging.newrefinement2.Level2.zaxis     = 0.0 0.0 340.0


```

```
#....................................#
#                ABL                 #
#....................................#


incflo.physics         = ABL Actuator
ICNS.source_terms        = BoussinesqBuoyancy BodyForce ABLMeanBoussinesq ActuatorForcing

##--------- Additions by calc_inflow_stats.py ---------#

ABL.wall_shear_stress_type     = "local"
ABL.inflow_outflow_mode      = true
ABL.wf_velocity        = 6.672666009608711 0.026233193028503826
ABL.wf_vmag          = 6.69105208840121
ABL.wf_theta         = 290.03617199583533

BodyForce.uniform_timetable_file   = "../abl_precursor_nuovo/abl_forces.txt"

BoussinesqBuoyancy.reference_temperature = 290


## Initial conditions
incflo.velocity                          = 10.59 0.0 0.0
ABL.bndry_file                           = ../abl_precursor_nuovo/bndry_file
ABLForcing.abl_forcing_height            = 150.0
ABLForcing.forcing_timetable_output_file = abl_forces.txt
ABL.tendency_forcing                     = false

ABL.bndry_io_mode                        = 1        # 0 = write, 1 = read
ABL.bndry_planes                         = xlo ylo
ABL.bndry_output_start_time              = 45000.0
ABL.bndry_var_names                      = velocity temperature

ABL.kappa                                = 0.41
ABL.surface_roughness_z0                 = 0.012
ABL.reference_temperature                = 290.0
ABL.surface_temp_rate                    = 0.0
ABL.log_law_height                       = 5.0

ABL.perturb_temperature      = true
ABL.cutoff_height            = 50
ABL.perturb_velocity         = true
ABL.perturb_ref_height       = 50
ABL.Uperiods                             = 4.0
ABL.Vperiods                             = 4.0
ABL.deltaU                               = 1.0
ABL.deltaV                               = 1.0
ABL.init_tke_beare_profile     = true
ABL.temperature_heights        = 0.0 750 850. 1040.0
ABL.temperature_values         = 290 290 295 297

ABLMeanBoussinesq.read_temperature_profile = true
ABLMeanBoussinesq.temperature_profile_filename = ../abl_precursor_nuovo/avg_theta.dat



#....................................#
#               TURBINES             #
#....................................#

Actuator.type                            = TurbineFastLine
Actuator.TurbineFastLine.epsilon         = 2.5 2.5 2.5         # based on delta_x. Currently eps = delta_x * 1
Actuator.TurbineFastLine.fllc            = true
Actuator.TurbineFastLine.fllc_nonuniform = 1
Actuator.TurbineFastLine.fllc_type    = variable_chord
Actuator.TurbineFastLine.fllc_eps_dr_ratio = 3
Actuator.TurbineFastLine.fllc_start_time = 5
Actuator.TurbineFastLine.density         = 1.225

Actuator.labels                          = T0 T1


Actuator.T0.type                         = TurbineFastLine
Actuator.T0.openfast_input_file          = T1_IEA-15-240-RWT-UMaineSemi/IEA-15-240-RWT-UMaineSemi.fst
Actuator.T0.base_position                = 1200.0 1280.0 0.0
Actuator.T0.rotor_diameter               = 240.0
Actuator.T0.hub_height                   = 150.0
Actuator.T0.num_points_blade             = 300
Actuator.T0.num_points_tower             = 0
Actuator.T0.fllc                         = true
Actuator.T0.epsilon              = 2.5 2.5 2.5
Actuator.T0.epsilon_min          = 2.5 2.5 2.5
Actuator.T0.epsilon_chord        = 0.25 0.25 0.25
Actuator.T0.openfast_start_time          = 0.0
Actuator.T0.openfast_stop_time           = 1000.0
Actuator.T0.nacelle_drag_coeff           = 0.0
Actuator.T0.nacelle_area                 = 0.0
```

```
Actuator.T0.yaw                          = 0
Actuator.T0.output_frequency             = 10
Actuator.T0.num_blades                   = 3
Actuator.T0.use_tip_correction           = true
Actuator.T0.use_root_correction          = true


Actuator.T1.type                         = TurbineFastLine
Actuator.T1.openfast_input_file          = T2_IEA-15-240-RWT-UMaineSemi/IEA-15-240-RWT-UMaineSemi.fst
Actuator.T1.base_position                = 2400.0 1280.0 0.0  # 5D
Actuator.T1.rotor_diameter               = 240.0
Actuator.T1.hub_height                   = 150.0
Actuator.T1.num_points_blade             = 300
Actuator.T1.num_points_tower             = 0
Actuator.T1.fllc                         = true
Actuator.T1.epsilon              = 2.5 2.5 2.5
Actuator.T1.epsilon_min          = 2.5 2.5 2.5
Actuator.T1.epsilon_chord        = 0.25 0.25 0.25
Actuator.T1.openfast_start_time          = 0.0
Actuator.T1.openfast_stop_time           = 1000.0
Actuator.T1.nacelle_drag_coeff           = 0.0
Actuator.T1.nacelle_area                 = 0.0
Actuator.T1.yaw                          = 0
Actuator.T1.output_frequency             = 10
Actuator.T1.num_blades                   = 3
Actuator.T1.use_tip_correction           = true
Actuator.T1.use_root_correction          = true


#...................................#
#              SAMPLING             #
#...................................#


incflo.post_processing                   = sampling
sampling.type                            = Sampling
sampling.output_frequency                = 100      #frequency*dt -- every 2 sec
sampling.fields                          = velocity p


sampling.labels                          = xy-domain xz-domain vert-line-yz0 vert-line-yz1 vert-line-yz2  vert-line-yz3 vert
     -line-yz4 vert-line-yz5 vert-line-yz6 vert-line-yz7 vert-line-yz8 vert-line-yz9 vert-line-yz10 vert-line-yz11 horiz-
     line-yz0 horiz-line-yz1 horiz-line-yz2 horiz-line-yz3 horiz-line-yz4 horiz-line-yz5 horiz-line-yz6 horiz-line-yz7 horiz
     -line-yz8 horiz-line-yz9 horiz-line-yz10 horiz-line-yz11

sampling.xy-domain.type                  = PlaneSampler
sampling.xy-domain.num_points            = 1153 193     # every 2.5m
sampling.xy-domain.origin                = 720.0 1040 150
sampling.xy-domain.axis1                 = 3359.0 0.0 0.0
sampling.xy-domain.axis2                 = 0.0 480.0 0.0

sampling.xz-domain.type                  = PlaneSampler
sampling.xz-domain.num_points            = 1153 193
sampling.xz-domain.origin                = 720.0 1280.0 0.0
sampling.xz-domain.axis1                 = 3359.0 0.0 0.0
sampling.xz-domain.axis2                 = 0.0 0.0 480.0


#Line Sampling


# Vertical line sampler in YZ-plane (along Z-axis, through full rotor diameter)     at 0D downstream
sampling.vert-line-yz0.type               = LineSampler
sampling.vert-line-yz0.num_points         = 29
sampling.vert-line-yz0.start              = 1200.0 1280.0 1
sampling.vert-line-yz0.end                = 1200.0 1280.0 481

# Vertical line sampler in YZ-plane (along Z-axis, through full rotor diameter)     at 1D downstream
sampling.vert-line-yz1.type               = LineSampler
sampling.vert-line-yz1.num_points         = 29
sampling.vert-line-yz1.start              = 1440 1280.0 1
sampling.vert-line-yz1.end                = 1440 1280.0 481




# Vertical line sampler in YZ-plane (along Z-axis, through full rotor diameter)     at 11D downstream
sampling.vert-line-yz11.type              = LineSampler
sampling.vert-line-yz11.num_points        = 29
sampling.vert-line-yz11.start             = 3840.0 1280.0 1.0
sampling.vert-line-yz11.end               = 3840.0 1280.0 481.0

...

# Horizontal line sampler in YZ-plane (along Z-axis, through full rotor diameter)     at 0D downstream
sampling.horiz-line-yz0.type              = LineSampler
sampling.horiz-line-yz0.num_points        = 15
sampling.horiz-line-yz0.start             = 1200.0 1040.0 150
```

```
sampling.horiz-line-yz0.end                = 1200.0 1520.0 150

# Horizontal line sampler in YZ-plane (along Z-axis, through full rotor diameter)     at 1D downstream
sampling.horiz-line-yz1.type               = LineSampler
sampling.horiz-line-yz1.num_points         = 15
sampling.horiz-line-yz1.start              = 1440.0 1040.0 150
sampling.horiz-line-yz1.end                = 1440.0 1520.0 150

...

# Horizontal line sampler in YZ-plane (along Y-axis, through full rotor diameter)     at 11D downstream
sampling.horiz-line-yz11.type               = LineSampler
sampling.horiz-line-yz11.num_points         = 15
sampling.horiz-line-yz11.start              = 3840.0 1040.0 150.0
sampling.horiz-line-yz11.end                = 3840.0 1520.0 150.0
```


DTU


TU Delft

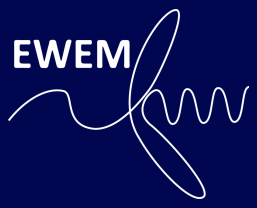
EWEM